



**EFFECT OF EQUIVALENCE RATIO AND G-LOADING ON IN-
SITU MEASUREMENTS OF CHEMILUMINESCENCE IN AN
ULTRA COMPACT COMBUSTOR**

THESIS

Jason M. Armstrong, Captain, USAF

AFIT/GAE/ENY/04-M01

**DEPARTMENT OF THE AIR FORCE
AIR UNIVERSITY**

AIR FORCE INSTITUTE OF TECHNOLOGY

Wright-Patterson Air Force Base, Ohio

APPROVED FOR PUBLIC RELEASE; DISTRIBUTION UNLIMITED

The views expressed in this thesis are those of the author and do not reflect the official policy or position of the United States Air Force, Department of Defense, or the United States Government.

AFIT/GAE/ENY/04-M01

EFFECT OF EQUIVALENCE RATIO AND G-LOADING ON IN-SITU
MEASUREMENTS OF CHEMILUMINESCENCE IN AN ULTRA COMPACT
COMBUSTOR

THESIS

Presented to the Faculty

Department of Aeronautics and Astronautics

Graduate School of Engineering and Management

Air Force Institute of Technology

Air University

Air Education and Training Command

In Partial Fulfillment of the Requirements for the
Degree of Master of Science in Aeronautical Engineering

Jason M. Armstrong, BS

Captain, USAF

March 2004

APPROVED FOR PUBLIC RELEASE; DISTRIBUTION UNLIMITED.

EFFECT OF EQUIVALENCE RATIO AND G-LOADING ON IN-SITU
MEASUREMENTS OF CHEMILUMINESCENCE IN AN ULTRA COMPACT
COMBUSTOR

Jason M. Armstrong, BS
Captain, USAF

Approved:

Ralph A. Anthenien (Chairman)

date

Richard J. McMullan (Member)

date

Mark F. Reeder (Member)

date

Abstract

Using a spectrometer and high temperature fiber optics the relative intensities of the near-infrared, visible and ultraviolet radiation emitted from the C_2^* , CH^* , and OH^* radicals were measured at eight discrete locations within the Ultra Compact Combustor test rig. Blackbody radiation in the near infrared was also observed. The tests were conducted at various g -loadings and overall equivalence ratios and with various air hole configurations. These measurements were compared to determine the effect of these changes on the radiation emitted. Local C_2^* intensities were used to estimate the flame location within the combustor and the local CH^*/OH^* ratio was used as a gauge of the local equivalence ratio within the cavity. Results indicate the highest ratios of CH^*/OH^* occur in the outer radius of the cavity where the high g -loads transport the colder unreacted fuel and air. The highest C_2^* ratios also occur in the outer radius. A correlation between cavity equivalence ratio and C_2^*/OH^* was determined for these experiments as well. Fuel droplet size characterization was also conducted using a laser diffraction particle size analyzer. The same pressure atomizer used in the Ultra Compact Combustor test rig was used. Fuel flow conditions simulated the same fuel flow conditions as the test rig. Experiments indicated poor atomization at the lower overall fuel to air ratio test conditions since the fuel flow pressure is relatively low at these test conditions. Combustion efficiencies were also some of the lowest efficiencies measured for these test conditions, which is indicative of poor fuel atomization. All experiments were completed in the Air Force Research Laboratory's Atmospheric Combustion Research Facility at Wright-Patterson AFB. This research supports compact common

core initiatives of the Versatile, Affordable, Advanced Turbine Engine (VAATE) program.

Acknowledgements

I would like to thank my advisor Captain, now Dr. Ralph A. Anthenien who provided guidance and assistance during experimental design, setup and writing process. I'd like to thank my thesis committee readers, Maj. Richard J. McMullan and Dr. Mark F. Reeder for providing assistance during the writing process.

I'd especially like to thank Dr. Julian Tishkoff, AFOSR, for providing funds to make this research possible and to Dr. Joe Zelina, AFRL/PRTS, and Dr. Michael Brown, ISSI, for assistance in defining the experiments of interest, the experimental setup and testing.

I'd also like to thank Glen Boggs and Dwight Fox of ISSI for their assistance in design and fabrication of the fiber optic probe components and interfaces as well as the operation of the Ultra Compact Combustor during testing.

Table of Contents

	Page
Abstract	iv
Acknowledgements	vi
List of Figures	ix
List of Tables	xiii
List of Symbols	xiv
List of Physical Constants.....	xvii
 I Introduction and Overview	 1
I.1 Aircraft Propulsion History	1
I.2 Motivation.....	2
I.3 Method	4
I.4 Thesis Content	4
 II Background and Theory	 5
II.1 Quantum Chemistry	5
II.2 Chemiluminescence.....	6
II.3 Fuel Spray Characteristics.....	8
II.4 Laser Diffraction Techniques	10
II.5 Laser Diffraction Error Effects.....	11
II.5 General Combustor Principles	12
II.5.1 Pressure Loss Parameters	12
 III Experimental Configuration.....	 14
III.1 Experimental Setup	14
III.2 Ultra Compact Combustor Test Rig	14
III.2.1 Ultra Compact Combustor Experimental Configuration.....	17
III.2.2 Fiber Optic Probe Construction	22
III.2.3 Test Rig Instrumentation and Data Acquisition Software	25
III.2.4 Spectrometer Instrumentation and Spectral Analysis Software.....	25
III.2.5 Calibration Lamp	26
III.3 Chemiluminescence Experimental Setup	26
III.3.1 Chemiluminescence Experimental Procedure	29
III.4 Fuel Spray Characterization Experimental Configuration.....	31
III.4.1 Laser Diffraction Particle Size Analyzer	31
III.4.2 Laser Test-bed Setup	31

III.5 Particle Size Experimental Setup	33
III.5.1 Particle Size Experimental Procedure.....	35
IV Results and Discussion	38
IV.1 Chemiluminescence Data Reduction.....	38
IV.2 CH*/OH* Chemiluminescence Results.....	49
IV.3 C ₂ */OH* Chemiluminescence Results	55
IV.4 C ₂ * Chemiluminescence Results	60
IV.5 Chemiluminescence Sensing Measurement Errors	66
IV.6 Fuel Droplet Size Analysis Results	68
V Conclusion.....	76
V.1 Chemiluminescence Conclusions	76
V.2 Fuel Atomization Conclusions	78
V.3 Recommendations	79
Appendix A.....	81
Bibliography.....	96
Vita.....	98

List of Figures

	Page
Figure 1: View of the Ultra Compact Combustor without Rear Flange.....	15
Figure 2: Cavity Side View.....	16
Figure 3: View of the UCC showing the cavity.....	17
Figure 4: Rear View of the Front Flange View Port Locations.....	18
Figure 5: Section A-A and B-B Superimposed on Each Other.....	19
Figure 6: Before and After Photograph of the Quartz Window with a Fitting for Size Comparison.....	21
Figure 7: View of the UCC Cavity showing the Soot Covered Quartz View Ports and the Soot Patterns after Combustor Operations.....	21
Figure 8: View of the Fiber Optic Probe connector.....	22
Figure 9: Fiber Optic Probe.....	23
Figure 10: Fiber Optic Setup.....	24
Figure 11: Air Hole Patterns for UCC configurations.....	27
Figure 12: Top View of Malvern Setup.....	32
Figure 13: Malvern 2600 Laser Test bed Setup.....	33
Figure 14: Side View of Malvern Setup.....	36
Figure 15: Typical Spectral Output from the UCC.....	38
Figure 16: Observed Spectral Output from the Calibration Lamp.....	39
Figure 17: True Lamp Intensities with Polynomial Curve Fits.....	40
Figure 18: Scaled Ratio of True Intensity to Measured Intensity for a Given Wavelength.....	41
Figure 19: Typical Calibrated Spectral Output from the UCC.....	42

Figure 20: Close Up Cut Away View of the UCC Showing Probe Displacement Distance.....	43
Figure 21: Variation in Spectra Signal Intensity with Axial Displacement.....	45
Figure 22: Comparison of Intensities from an Inner Radius and an Outer Radius Hole.....	46
Figure 23: Close Up of Radical Emissions Spectral Bands.....	47
Figure 24: Calculation of the Area of the OH* Spectral Feature.....	48
Figure 25: Histogram of CH*/OH* Ratio.....	50
Figure 26: Rear view of the UCC showing the fuel injector cone angle.....	51
Figure 27: Superposition of View Ports on to One Fuel Injector Cone Angle.....	53
Figure 28: Average CH*/OH* Versus Cavity Equivalence Ratio for Both Experimental Configurations.....	54
Figure 29: Histogram of C ₂ */OH* Ratio.....	56
Figure 30: Average C ₂ */OH* Versus Cavity Equivalence Ratio for Both Experimental Configurations.....	57
Figure 31: Average C ₂ */OH* Versus Cavity Equivalence Ratio for Both Experimental Configurations and Morrell's n-Heptane Data.....	58
Figure 32: Roby's CH*/OH* data for a premixed methane/air flame.....	60
Figure 33: Histogram of C ₂ *.....	62
Figure 34: C ₂ * Intensity versus Radial Position for the Inner Radius, 2% Pressure Loss, Configuration 1.....	63
Figure 35: C ₂ * Intensity versus Radial Position for the Outer Radius, 2% Pressure Loss, Configuration 1.....	63
Figure 36: C ₂ * Intensity versus Cavity Equivalence Ratio.....	65
Figure 37: C ₂ * Intensity versus G-Load for Constant Φ and $\Phi > 1$	66
Figure 38: Comparison of a Used and a New Graphite Ferrule.....	68
Figure 39: Fuel Droplet Size Distribution for Test Number 2.....	71

Figure 40: Histogram of Combustion Efficiency Grouped by Particle Size Test Number.....	73
Figure 41: Combustion Efficiency versus Fuel Pressure.....	73
Figure 42: Carbon Monoxide Emission Index for Each Test Condition.....	75
Figure 43: Unburned Hydrocarbons Emission Index for Each Test Condition.....	75
Figure 44: C_2^* Intensity versus Radial Position for the Inner Radius, 3% Pressure Loss, Configuration 1.....	81
Figure 45: C_2^* Intensity versus Radial Position for the Inner Radius, 5% Pressure Loss, Configuration 1.....	81
Figure 46: C_2^* Intensity versus Radial Position for the Outer Radius, 3% Pressure Loss, Configuration 1.....	82
Figure 47: C_2^* Intensity versus Radial Position for the Inner Radius, 5% Pressure Loss, Configuration 1.....	82
Figure 48: C_2^* Intensity versus Radial Position for the Inner Radius, 2% Pressure Loss, Configuration 2.....	83
Figure 49: C_2^* Intensity versus Radial Position for the Inner Radius, 3% Pressure Loss, Configuration 2.....	83
Figure 50: C_2^* Intensity versus Radial Position for the Inner Radius, 5% Pressure Loss, Configuration 2.....	84
Figure 51: C_2^* Intensity versus Radial Position for the Outer Radius, 2% Pressure Loss, Configuration 2.....	84
Figure 52: C_2^* Intensity versus Radial Position for the Outer Radius, 3% Pressure Loss, Configuration 2.....	85
Figure 53: C_2^* Intensity versus Radial Position for the Outer Radius, 5% Pressure Loss, Configuration 2.....	85
Figure 54: View Port A. CH^*/OH^* Versus Cavity Equivalence Ratio for Both Experimental Configurations.....	86
Figure 55: View Port B. CH^*/OH^* Versus Cavity Equivalence Ratio for Both Experimental Configurations.....	86

Figure 56: View Port C. CH*/OH* Versus Cavity Equivalence Ratio for Both Experimental Configurations.....	87
Figure 57: View Port D. CH*/OH* Versus Cavity Equivalence Ratio for Both Experimental Configurations.....	87
Figure 58: View Port E. CH*/OH* Versus Cavity Equivalence Ratio for Both Experimental Configurations.....	88
Figure 59: View Port F. CH*/OH* Versus Cavity Equivalence Ratio for Both Experimental Configurations.....	88
Figure 60: View Port G. CH*/OH* Versus Cavity Equivalence Ratio for Both Experimental Configurations.....	89
Figure 61: View Port H. CH*/OH* Versus Cavity Equivalence Ratio for Both Experimental Configurations.....	89
Figure 62: View Port A. C ₂ */OH* Versus Cavity Equivalence Ratio for Both Experimental Configurations.....	90
Figure 63: View Port B. C ₂ */OH* Versus Cavity Equivalence Ratio for Both Experimental Configurations.....	90
Figure 64: View Port C. C ₂ */OH* Versus Cavity Equivalence Ratio for Both Experimental Configurations.....	91
Figure 65: View Port D. C ₂ */OH* Versus Cavity Equivalence Ratio for Both Experimental Configurations.....	91
Figure 66: View Port E. C ₂ */OH* Versus Cavity Equivalence Ratio for Both Experimental Configurations.....	92
Figure 67: View Port F. C ₂ */OH* Versus Cavity Equivalence Ratio for Both Experimental Configurations.....	92
Figure 68: View Port G. C ₂ */OH* Versus Cavity Equivalence Ratio for Both Experimental Configurations.....	93
Figure 69: View Port H. C ₂ */OH* Versus Cavity Equivalence Ratio for Both Experimental Configurations.....	93
Figure 70: UCC in Operation at a Lean Cavity Equivalence Ratio.....	94
Figure 71. UCC in Operation with a Rich Cavity Equivalence Ratio.....	95

List of Tables

	Page
Table 1: View Port Location with the UCC cavity.....	20
Table 2: Chemiluminescence Test Matrix.....	28
Table 3: Fuel Flow Rates for Particle Size Experiments.....	34
Table 4: Particle Size Experiment Identification.....	35
Table 5: Axial Displacement of the Fiber Optic Probe.....	44
Table 6: Wavelength Range for Area Calculations.....	49
Table 7: CH*/OH* Ratio.....	49
Table 8: View Port Location with respect to the Fuel Injector.....	52
Table 9: Coefficients and Centering & Scaling Parameters for CH*/OH*	55
Table 10: C ₂ */OH* Ratio.....	55
Table 11: Coefficients and Centering & Scaling Parameters for C ₂ */OH*.....	57
Table 12: C ₂ * Intensity.....	61
Table 13: Results of the Repeatability Test.....	67
Table 14: Particle Sauter Mean Diameter.....	70
Table 15: Fuel Pressure and Combustion Efficiency.....	72

List of Symbols

Nomenclature

A/D = Analog to Digital

AFRL = Air Force Research Laboratory

CFD = Computational Fluid Dynamics

CP = Calibration Parameter

d = Fuel Orifice Diameter or Initial Jet Diameter

D = Diameter

EI = Emissions Index

FN = Flow Number

g = acceleration due to gravity

G = G-Loading

I = Intensity

I.D. = Inner Diameter

ITB = Inter Turbine Burner

\dot{m} = Mass Flow Rate

MTBM = Mean Time Between Maintenance

O.D. = Outer Diameter

OFAR = Overall Fuel to Air Ratio

P = Power

r = radius

R = total energy radiated per unit area per unit time from a blackbody

Re = Reynolds number

SMD = Sauter Mean Diameter

ST = Specific Thrust

T = Temperature

TSFC = Thrust Specific Fuel Consumption

T/W = Thrust to Weight ratios

U = Velocity

V = Velocity

UCC = Ultra Compact Combustor

WE = Weber number

Symbols

ε = Emissivity

Φ = Equivalence Ratio

η = Wave Number

λ = Wavelength

ν = Velocity

ρ = Density

σ = Surface Tension

μ_1 = the mean(x)

μ_2 = the std(x).

Subscripts

3 = Combustor Inlet

3-4 = Across the Combustor

4 = Combustor Outlet

CN = Calibrated and Normalized

f = fuel

a = air

ac = cavity air

am = main air

max = maximum

0 = initial

R= air relative to fuel or reference

Ref = reference

Tan = tangential

Units

m = meter

K = Kelvin

psi = Pounds per Square Inch

W = watt

Prefixes

m = milli

μ = micro

n = nano

List of Physical Constants

$$c = \text{Speed of Light} = 2.997925 \times 10^8 \text{ m} \cdot \text{s}^{-1}$$

$$h = \text{Planck's Constant} = 6.62618 \times 10^{-34} \text{ J} \cdot \text{s}$$

$$k = \text{Boltzmann's Constant} = 1.38066 \times 10^{-23} \text{ J} \cdot \text{K}^{-1}$$

$$\sigma = \text{Stefan-Boltzmann Constant} = 5.67032 \times 10^{-8} \text{ J} \cdot \text{m}^{-2} \cdot \text{K}^{-4} \cdot \text{s}^{-1}$$

EFFECT OF EQUIVALENCE RATIO AND G-LOADING ON IN-SITU MEASUREMENTS OF CHEMILUMINESCENCE IN AN ULTRA COMPACT COMBUSTOR

I Introduction and Overview

I.1 Aircraft Propulsion History

In the early days of aviation the goal of aircraft was to go faster and higher. To set these milestones the powerplants propelling these aircraft needed to improve and evolve. Early aircraft used piston engines for propulsion, but piston engine/propeller combinations are most efficient from 0.4-0.7 Mach number. Higher speeds require a different propulsion system. In the 1930's Frank Whittle and Hans Von Ohain separately developed the turbojet engine. These powerplants were first used to power military aircraft such as the Gloster Meteor and the Messerschmidt Me-262 during the final months of World War II. Rockets were also used as the propulsion source of some aircraft such as the Bell X-1 and North American X-15 experimental aircraft to help push the speed envelope beyond the speed of sound and into the hypersonic realm. Rockets, though useful for experimental aircraft and missiles, were not well suited for production aircraft since they provide thrust for such short periods of time and are required to carry their oxidizer internally thus adding considerably to the weight of the aircraft. In the late 1960's and 1970's the economics of air travel became the driving force behind engine design. Turbojets gave way to turbofans since they have a lower Thrust Specific Fuel Consumption (TSFC), which improves the fuel economy, hence reducing the costs of

operating an aircraft. Today this still remains the main driving force behind engine design. Environmental concerns are also a major factor in current engine design. Pollutants such as NO_x , SO_x and CO have an effect on the environment and plant and animal life. NO oxidizes with ozone, O_3 , to form NO_2 and O_2 , thus effecting the ozone layer. SO_x is a cause of acid rain and sulfur compounds lead to particulate formation that can divert solar radiation from the Earth (Levebvre, 1983:463) Using fuels with low sulfur content can minimize SO_x emissions.

In recent years research has delved into innovative combustor designs to improve upon Thrust to Weight ratios (T/W) while maintaining high efficiencies and minimizing emissions. Research into the design of an Ultra Compact Combustor (UCC) is one such effort.

I.2 Motivation

Research into an UCC design has been an ongoing effort at the Air Force Research Laboratory (AFRL) Propulsion Directorate, Turbine Engine Division, Combustion Science Branch (PRTS). The premise of the UCC is to shorten the combustor chamber by using centrifugal acceleration effects to produce shorter flame lengths that run radially as opposed to axial flames in the combustor of a conventional gas turbine engine. Shorter flames lengths are caused when the time to complete combustion is shorter. In order to shorten combustion time the flame propagation rate through the combustible mixture must be increased. Research into propane-air mixtures completed by Lewis showed that flame propagation rate increased proportional to the square root of the acceleration when the centrifugal acceleration was greater than 200 g's. (Lewis, 1972) Thus centrifugal acceleration is the key to increasing flame propagation

rate and shortening the flame length. Having shorter flame lengths means the combustor can be made shorter and still contain the flame. For a given combustor efficiency and mass flow rate (\dot{m}) having a shorter combustor reduces the weight and size of the engine thus increasing the T/W.

With the shorter flame lengths and lower weight combustors the concept of an Inter Turbine Burner (ITB) can be realized. An ITB burns fuel in the stator passages between the turbine rotors. It has been shown that specific thrust (ST) can be increased by over 50% using a single stage ITB within a conventional gas turbine engine without a dramatic increase in TSFC which is the case in a gas turbine using an afterburner (Sirignano and Liu, 1999). Since the UCC concept relies on the swirl effect of the incoming air to create high “g” loads further weight savings can be realized by the removal of the stators prior to the combustor (Quaale, 2003).

The benefits of an engine using an UCC or ITB are numerous. Smaller engines could be produced with the same thrust as a conventional gas turbine, but with lower TSFC. Engines with the same weight as a conventional gas turbine could be produced that have higher thrust or produce the same thrust with a lower turbine inlet temperature, thus increasing the life of turbine blades and reducing the Mean Time Between Maintenance (MTBM) (Quaale, 2003:2). An UCC with the same weight as a conventional gas turbine combustor could also be produced that has the same thrust, but the additional energy can be used to power an ultra high bypass ratio fan or drive a generator to provide electricity for high-powered devices such as lasers or sensor suites for unmanned aerial vehicles (Zelina, 2002). Thus the UCC should be of great importance to the commercial and military aviation sectors.

I.3 Method

Data from recent experiments at AFRL/PRTS using chemiluminescence and data from other sources will be utilized. Spatial differences of combustion within the test rig will be investigated. The CH^*/OH^* ratio and C_2^*/CH^* ratio will be evaluated and their relation to cavity equivalence ratio as well as their physical significance within various locations of the cavity will be determined. C_2^* intensities as a function of position and their physical significance on flame location will be determined.

I.4 Thesis Content

This work covers the experimental work completed on the UCC and the laser diffraction equipment. A comparison is done between the data collected in these experiments and other published works using chemiluminescence of liquid fuels or methane. Finally, conclusions about the data collected are developed to address trends that lead to hypotheses.

II Background and Theory

II.1 Quantum Chemistry

Some background in quantum chemistry is necessary before discussing chemiluminescence. When atoms are subjected to very high temperatures they radiate at specific wavelengths as the electrons transition from one state to another (Gaydon, 1957:3). These spectra are known as line spectra. When a molecule is subjected to high temperature it radiates with bands of wavelengths that are known as band spectra. These band spectral features are of importance to these chemiluminescence experiments since the spectra of several molecules will be analyzed.

Two effects that change the shape of the bands are known as Doppler broadening and collision broadening. Because the molecules of an emitting gas are not stationary an effect known as Doppler broadening occurs. If a molecule is emitting at a wave number (reciprocal of the wavelength), η_{ij} and is also moving at a velocity, v , toward an observer the observed wave number, η is increased (Siegel and Howell, 1992: 545).

$$\eta = \eta_{ij} \left(1 + \frac{v}{c} \right) \quad (1)$$

where c is the *speed of light*

Conversely if the molecule is moving away from the observer the wave number observed will be less. Since molecular motion is a function of thermal energy, Doppler broadening is important at high temperatures.

As the pressure of the gas is increased the collision rate of the molecules is increased. Collisions disturb the energy states of the molecules resulting in collision broadening (Siegel and Howell, 1992: 546). Collision broadening or Lorentz broadening

as it is also known as becomes important at high pressures and either low temperatures or high densities.

Another spectral feature of importance is that of blackbody radiation. A blackbody is any object that completely absorbs all incident radiation of all wavelengths from all directions (Siegel and Howell, 1992: 1053). Blackbody radiation is a continuous spectral feature because it absorbs at all wavelengths. Continuous spectra are usually the result of solid particles such as soot, the combustor walls or liquid droplets (Gaydon, 1957:4). The spectra of the blackbody can be related to the temperature of the blackbody through Wien's displacement law. If λ_{max} is the wavelength at which energy density per wavelength, $\rho'(\lambda, T)$, is a maximum, then (McQuarrie, 1983:10)

$$\lambda_{max}T = 2897 \mu\text{m-K} \quad (2)$$

where T is the *temperature*.

Additionally the Stefan-Boltzmann law gives the total energy radiated per unit area per unit time from a blackbody.

$$R = \epsilon \sigma T^4 \quad (3)$$

where ϵ is the *emissivity* and σ is the *Stefan-Boltzmann Constant*. (McQuarrie, 1983:11).

II.2 Chemiluminescence

In order to identify local changes in equivalence ratio it is necessary to determine the relative intensities of chemical constituents present at or very near to the flame. Chemiluminescence sensing is one technique to accomplish this.

Chemiluminescence is the light released by excited molecules when they return to their equilibrium ground state (Roby and others ,1998). The light released at specific wavelengths is dependent upon the species that emits it. The wavelengths studied for these experiments were selected so as to include those emitted by the species OH*, CH* and C₂*. These radicals are used since the transition from the ground state to the lowest excited state requires relatively little energy and can be excited strongly by the temperatures found in flames (Gaydon, 1957:4). OH* radicals emit in the ultraviolet at 306.4 nm, The main CH* emission is at 431.5 nm and a weaker emission occurs at 388.9 nm. The main C₂* emission is at 516.5 nm. Though the intensity of a radical emission can be determined it is difficult to relate this intensity to concentration as some of the radical could be absorbed (Gaydon:1957:9).

Various research efforts have determined strong correlations between OH*/CH* and equivalence ratio. Ikeda and others found this relationship to be nearly linear for premixed laminar methane/air flames when the equivalence ratio was less than 1.4 (Ikeda and others, 2002). Roby and others found linear relationships between OH*/CH* and equivalence ratio in lean premixed laminar methane/air flames and in lean premixed turbulent methane/air flames (Roby and others ,1998). Roby puts forth the theory that OH* production is tied to the concentration of the oxidizer and CH* production is tied to the concentration of fuel (Roby and others ,1998). An increase in equivalence ratio means more fuel is present and the OH*/CH* ratio should decrease. Ikeda's results lend credence to this argument (Ikeda and others, 2002).

Research efforts also suggest that in addition to an equivalence ratio dependence, the OH*/CH* ratio is also dependent upon fuel type(Roby and others ,1998). Since

Roby's and Ikeda's research focused on methane/air (CH_4) flames with a C/H ratio of 4 the linear correlations empirically determined in the studies would not be of any direct use in the UCC except for trending purposes.

Morrell and others used chemiluminescence sensing in a non-premixed, liquid fueled combustor using n-heptane (C_7H_{16}) as the fuel. Like Ikeda's and Roby's research Morrell and others found a decrease in OH^*/CH^* with increasing equivalence ratio (Morrell and others, 2001). Morrell also noted that C_2^*/OH was very sensitive to changes in equivalence ratio, but not to the extent that it was in a premixed methane/air flame. Morrell concluded this is probably due to the limited chemical pathways for production of C_2^* since methane has no Carbon-Carbon bonds especially for lean mixtures (Morrell and others, 2001). In the combustion of liquid hydrocarbons there are more pathways that lead to C_2^* in both lean and rich mixtures a thus a smaller dependence on equivalence ratio (Morrell and others, 2001).

II.3 Fuel Spray Characteristics

There are several characteristics of fuel sprays important to the combustion process, fuel drop size and distribution being two of them (Lefebvre, 1983:375). Fuel drop size is dependent on the amount of atomization caused by the fuel injector. Atomization is the process of converting a volume of liquid into many smaller drops. Fuel atomization is an important part of the combustion process. Smaller fuel droplets mean more surface area and faster evaporation rates. Not all droplets will be the same size so a way to characterize the level of atomization using a mean diameter is necessary. Since fuel evaporation rate is important and is the result of the surface area size, the

Sauter Mean Diameter (SMD or D_{32}) is one of the most widely used to measure mean diameter. The SMD replaces the actual fuel droplet size distribution with one droplet size that is representative of the fuel spray. The SMD is the diameter of a fuel droplet of the same volume to surface ratio as the entire fuel spray (Lefebvre, 1983:375).

$$SMD = \frac{\sum D^3}{\sum D^2} \quad (4)$$

where D is the *diameter of each fuel droplet*. Once the fuel spray leaves the injector nozzle atomization continues until a critical fuel drop size is reached.

The critical fuel drop size is dependent upon the fuel jets velocity relative to surrounding air. In the UCC the cavity air holes and the fuel injectors have the same angle from the radial direction, however the circumferential distance between the air holes and fuel injectors cause these features to be angled relative to one another. If the fuel and air flow were in the same direction penetration of the fuel spray would be increased, atomization effects would be retarded and the mean drop diameter would increase (Lefebvre, 1983:389). A parameter that helps define the fuel drop size when a liquid jet breaks up into smaller drops due to the influence of surrounding air and is governed by the ratio of disruptive aerodynamic forces to the surface tension forces is a dimensionless parameter known as the Weber number.

$$We = \frac{\rho_A U_R^2 d_0}{\sigma} \quad (5)$$

where ρ_A is the *air density*, U_R is the *velocity of the air relative to the fuel*, d_0 is the *fuel orifice diameter* or *initial jet diameter*, and σ is the *surface tension* (Lefebvre, 1983: 373). As the Weber number increases finer atomization occurs (Lefebvre, 1983: 397).

Fuel drop size distribution is an important part of fuel spray characterization as well. A large quantity of smaller drop sizes is necessary for ease of combustor ignition while having a large quantity of larger drop sizes could impact emissions since these drops will be too large to evaporate and contribute to combustion (Lefebvre, 1983:389).

Fuel particles are typically modeled using a Rosin-Rammler distribution which was first used for materials that are fractured into smaller parts such as in coal crushing (Verheijen, 2001). Spray atomization can be thought of as cylinder or cone of fuel breaking up into smaller drops so this distribution type is appropriate. Mathematically the Rosin-Rammler distribution is the integral of the Weibull distribution.

II.4 Laser Diffraction Techniques

Laser diffraction uses the scattering of a laser beam by a particle to measure the size of the particle. This is accomplished by measuring the scatter angle. Large particles scatter at low angles while small particles scatter at high angles. The laser diffraction techniques applied to measuring the fuel droplet sizes require a basic understanding of a few key principles with Mie Theory of scattering being one of them. It is used when the diameter of the particle being measured is as large as or larger than the wavelength of the electromagnetic radiation scattered by the particle, or put simply, when the diameter to wavelength ratio is on the order of unity or greater. The Malvern 2600 Particle Sizer used in these experiments adheres to this theory since the fuel droplet sizes being measured are on the order of micrometers while the laser beam that is scattered by these fuel drops is on the order of nanometers. Laser diffraction techniques using the Malvern 2600 Particle Sizer fall into the category of non-imaging optical systems since an image of the particle is not needed in order to determine its size. The laser light is refracted

forward to the detector elements which are arranged radially to measure the scatter angle and calculate the size based on this information. Laser light that passes directly through the particles without being refracted is also measured in order to determine obscuration of the laser beam. Effects of obscuration will be discussed later.

II.5 Laser Diffraction Error Effects

There are several effects that can occur in laser diffraction that can contribute to the error in estimation of particle size. Two of the most significant are obscuration and vignetting.

Obscuration causes errors due to the density of spray whereby photons are scattered off more than one particle. This causes the indicated distribution to be broader in distribution and smaller in average size than the actual distribution since the photons are scattered off more than one particle thereby increasing the angle of scatter (Dodge, 1984b). The magnitude of the error depends on spray size with a stronger effect for smaller drops. When transmission of unscattered light is less than 50% some correction factor should be used. If transmission is less than 4% then data cannot be corrected. (Dodge, 1984b).

$$\text{Obscuration} = \frac{P_{D_{\text{Lost}}}}{P_{D_{\text{Nondiffracted}}}} \quad (6)$$

Where $P_{D_{\text{Lost}}}$ is the *power lost to diffraction* and $P_{D_{\text{Nondiffracted}}}$ is the *total power of a non-diffracted beam*.

Vignetting occurs when the particles being measured are so far away from the collection lens that the maximum scattering angle can not be collected by the lens.

Vignetting causes the calculated size distribution to be skewed toward the larger particle sizes because the larger scatter angles of the smaller particles are not collected by the lens (Dodge, 1984a). Vignetting occurs in the outer detector rings causing a decrease in the intensity on these rings. Vignetting effects increase as the sample gets further away from the lens. If the sample is within a certain cut-off distance from the lens no vignetting effects occur.

II.5 General Combustor Principles

While there are many different principles that are of interest in combustor design and performance only a few that are relevant to this research are detailed in this section.

II.5.1 Pressure Loss Parameters

Two parameters of importance in combustor design are the overall pressure loss and the pressure loss factor.

Overall pressure loss, $\frac{\Delta P_{3-4}}{P_3}$, is usually reported as a percentage (Lefebvre, 1983:108)

ΔP_{3-4} represents the pressure drop across the combustor while P_3 represents the combustor inlet pressure.

Pressure Loss Factor $\frac{\Delta P_{3-4}}{q_{ref}}$, is similar to a drag coefficient and is a fixed property of the combustor chamber. (Lefebvre, 1983:108)

$q_{ref} = \frac{\rho_3 U_{ref}^2}{2}$ and is also referred to a dynamic pressure.

II.5.2 Flow Number

Flow number, FN describes the effective flow area of a fuel injector. $FN = \frac{\dot{m}_f}{\Delta P^{0.5}}$

where \dot{m}_f is in lb/hr and ΔP is in psi. (Lefebvre, 1983:388)

II.5.3 Equivalence Ratio.

Equivalence ratio, Φ , is the fuel to air ratio of a given combustible mixture divided by the stoichiometric fuel to air ratio of a given combustible mixture. From an energy perspective gas turbine engines are most efficient at a $\Phi=1$ since temperature is at a maximum at this value.

III Experimental Configuration

III.1 Experimental Setup

The experimental setup consists of two parts, the UCC test rig setup and the fuel droplet analysis setup. The UCC test rig setup includes the test rig and the associated data acquisition system along with the fiber optic probe and its associated data acquisition system. The fuel droplet analysis setup includes the laser diffraction analyzer and its associated data acquisition system. All of these parts are described in detail below

III.2 Ultra Compact Combustor Test Rig

The Ultra Compact Combustor test rig is located in the Atmospheric Combustion Research Laboratory at Wright Patterson AFB. The combustor consists of a front and a rear flange bolted together around a pressure ring and a liner ring. A center body with six vanes passes through the middle of this flange-ring combination. Figure1 is a photo of the combustor.

Unlike combustors for turbofan engines used in both military and commercial aviation, the UCC test rig operates at atmospheric pressure. This allows the UCC test rig to be operated without the need for powerful pumps to compress the incoming air and simplifies the overall operation of the test rig. The UCC's cavity is approximately 18.1 in³ in volume.

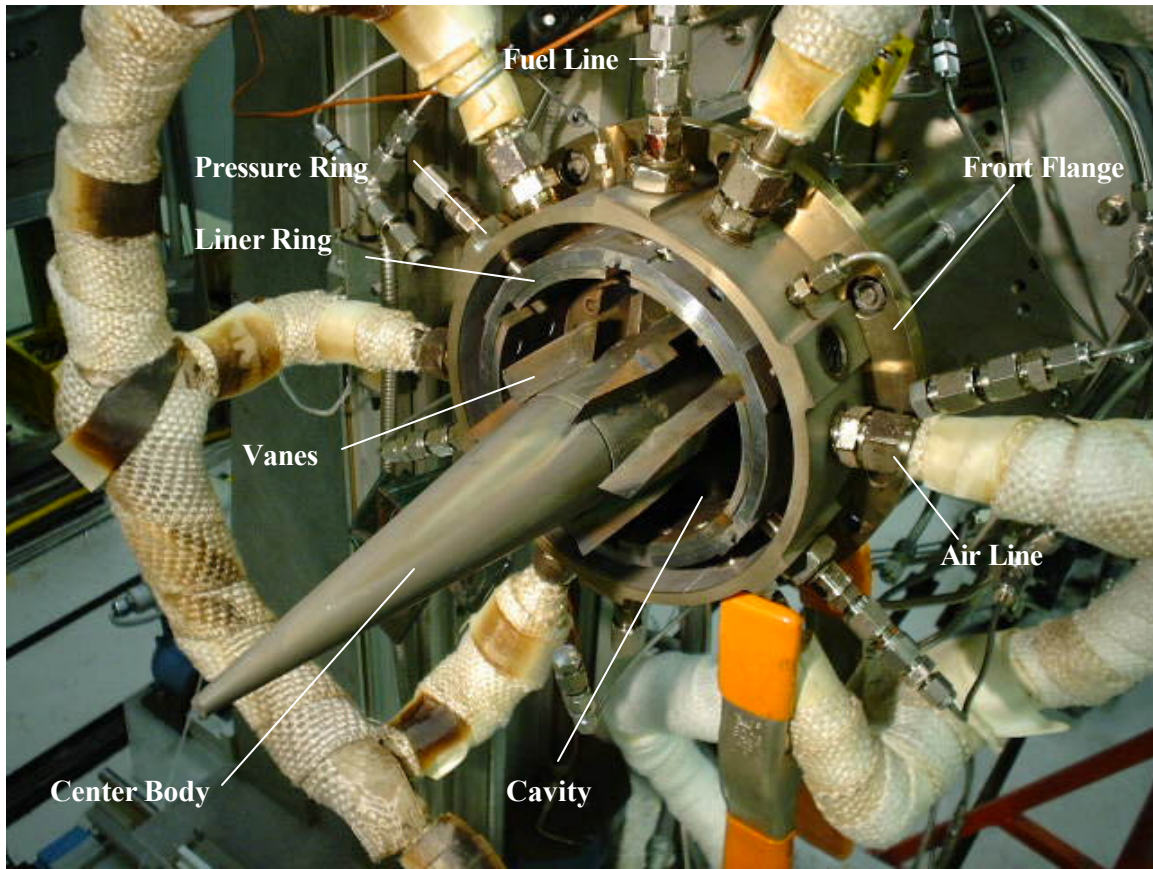


Figure 1: View of the Ultra Compact Combustor without Rear Flange

During operation airflow to the combustor is preheated to 500 °F. Air flows into the combustor from two sources, main airflow and cavity airflow. Main air flows through a heater then through a plenum and into the combustor via an inlet in an axial direction. Cavity airflow enters the combustor perpendicular to the axial flow and at approximately a 37° angle to the radial direction through air ports which cause a circumferential swirl effect within the cavity. The two sources of airflow combine in the combustor near the vanes and exit in an axial manner along the tail of the center body. Figure 2 is a schematic of the side view of the cavity showing this air flow.

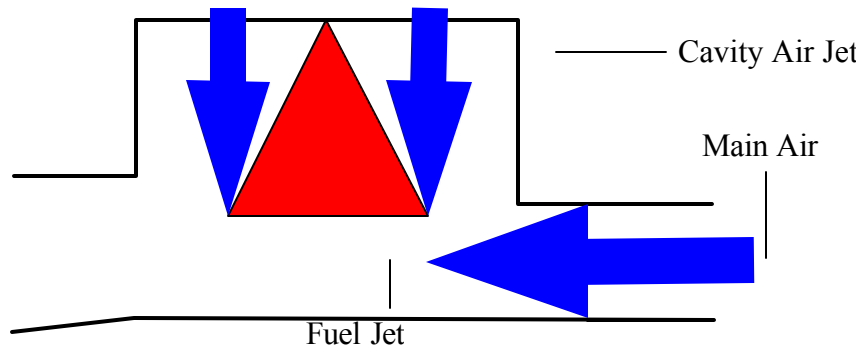


Figure 2: Cavity Side View

JP-8 +100 fuel is injected into the cavity via six fuel injectors located at 60° intervals for a total of six injectors. The fuel injectors are angled 37° like the cavity air holes. This minimizes the interference between the fuel spray fan pattern and the circumferential cavity airflow. Parker-Hannifin model# 67700-1 fuel injectors were used during the experiments. They have a flow number of $0.5 \text{ lb}_m/\text{hr}/\text{psi}^{0.5}$ and a cone angle of 45° . Fuel ignition occurs via two spark plugs that ignite an ethylene/air mixture. This mixture travels a short distance through two small tubes into the cavity igniting the evaporated JP-8 +100 fuel/air mixture. Figure 3 provides another view of the UCC interior.

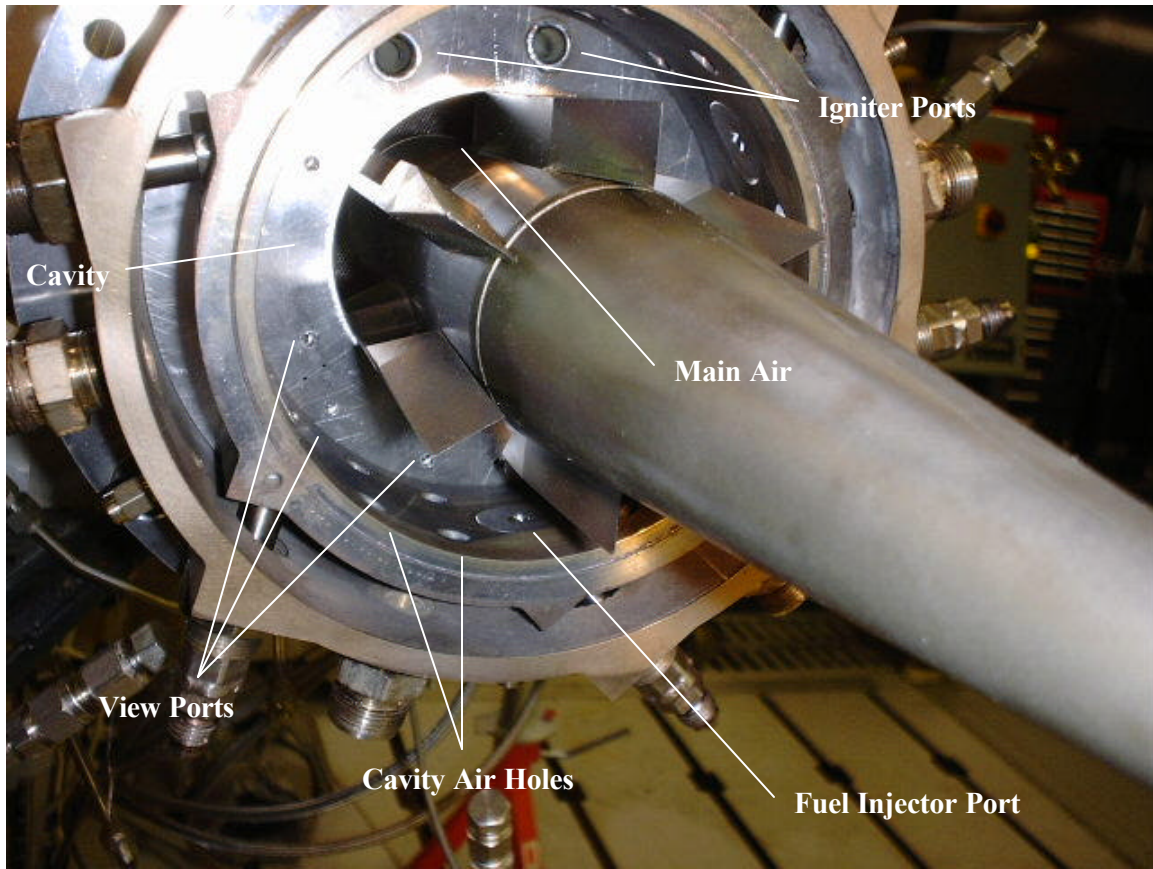


Figure 3: View of the UCC showing the cavity

III.2.1 Ultra Compact Combustor Experimental Configuration

Since the current configuration of the UCC does not allow direct viewing of the combustor cavity, view ports were added to the front (upstream) flange. Figure 4 shows the location of the view ports on the front flange with the main body rings superimposed on the flange to show the location of the air holes, fuel injector ports and the cavity. The letters represent the identifying marks that relate each hole to its location within the cavity. This is explained in detail in Table 1.

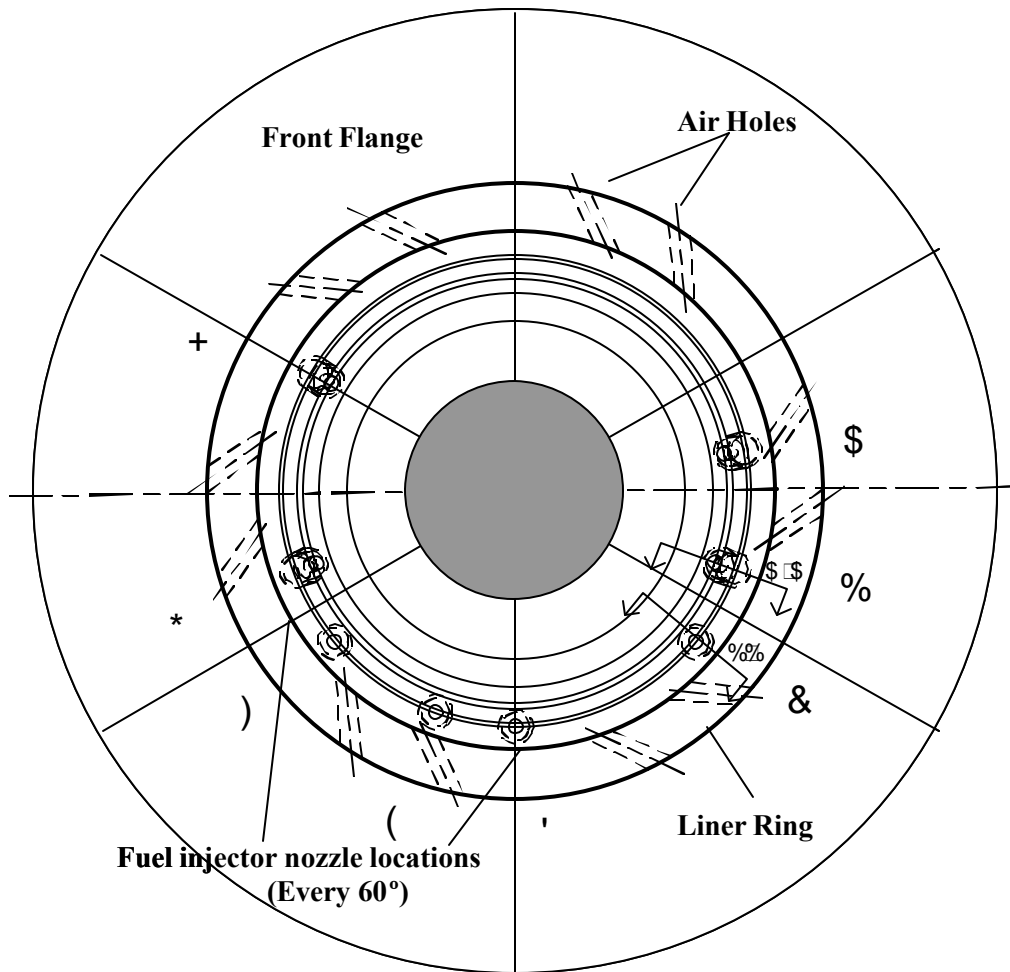


Figure 4: Rear View of the Front Flange View Port Locations

The view ports are located such that two different radii within the cavity may be observed; one that has a field of view of the outer radius of the cavity and one that has a field of view of the inner radius of the cavity. Due to the location of the incoming air inlet, viewing the inner radius of the cavity was not feasible unless the view ports were angled. Figure 5 represents cross sections A-A and B-B seen in figure 4 and shows how these view ports are angled and the sections of the cavity that can be viewed through the ports. Error bounds have been placed on the viewing area due to the tolerances placed on the manufacture of the fiber optics.

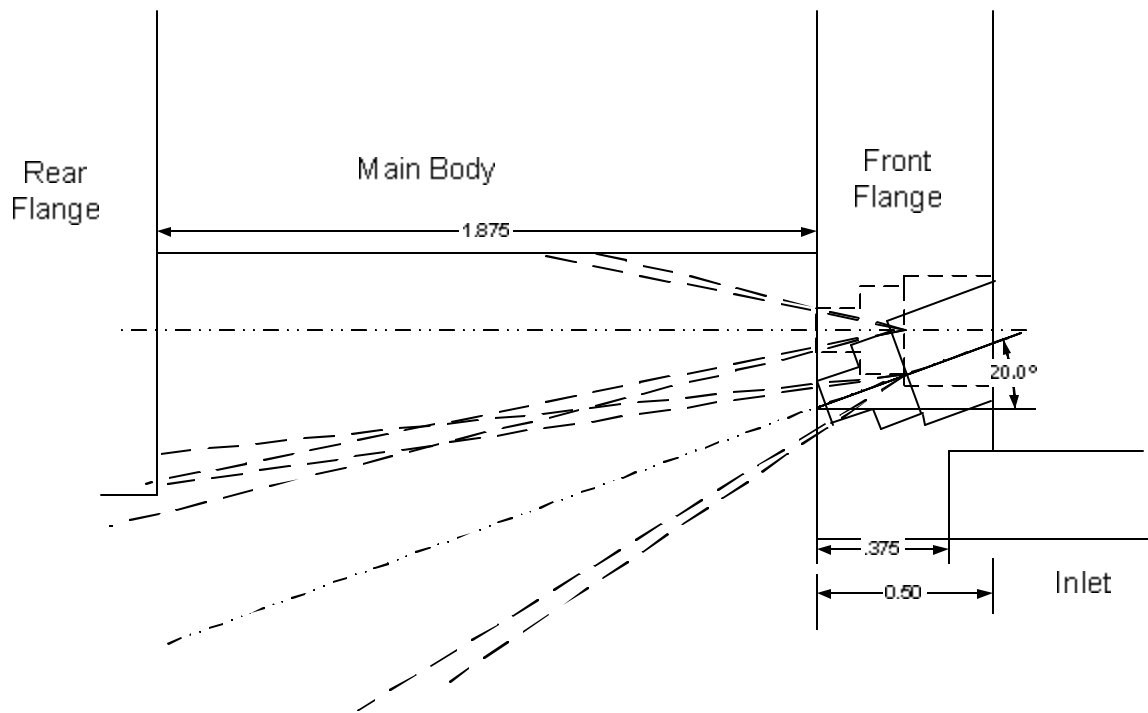


Table 1: View Port Location with the UCC cavity

View Port ID	View Port Location
A	Inner Radius, In-line with Air Hole
B	Inner Radius, 10° Upstream of Fuel Injector
C	Outer Radius, 10° Downstream of Fuel Injector
D	Outer Radius, In-line with Fuel Injector
E	Outer Radius, In-line with Air Hole
F	Outer Radius, 10° Upstream of Fuel Injector
G	Inner Radius, 10° Downstream of Fuel Injector
H	Inner Radius, In-line with Fuel Injector

In order to automate many of the calculations used in the results section the view port identification may also be listed with a numerical identification. Initially each of the ports was to have a quartz window in order to shield the fiber optic probe from the direct heat of the cavity, but after performing a test with the quartz windows placed in the ports it was observed that the windows would quickly cake over with soot almost as soon as light-off was complete. Thus the fiber optic probe's ability to gather radiation from the combustor would be compromised. Figure 6 shows the condition of the quartz window before and after operation. Notice the amount of soot after operation



Figure 6: Before and After Photograph of the Quartz Window with a Fitting for Size Comparison

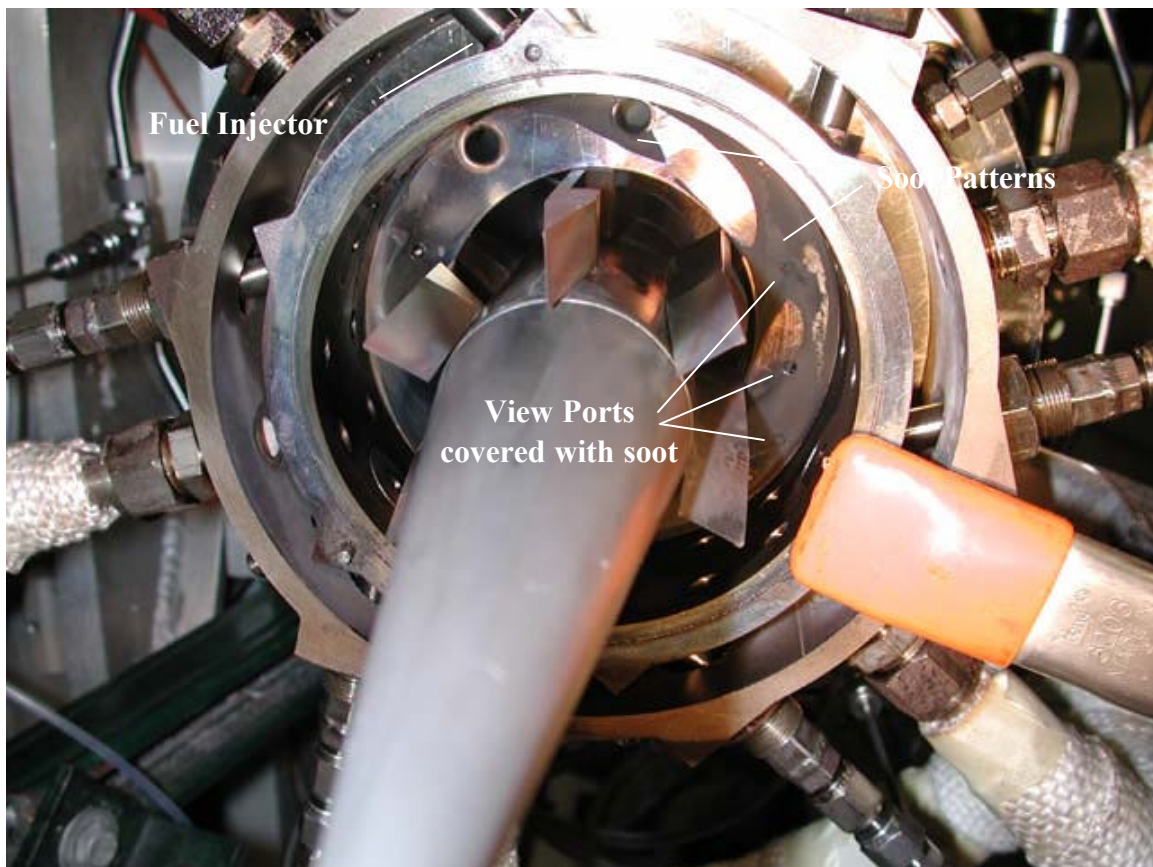


Figure 7: View of the UCC Cavity showing the Soot Covered Quartz View Ports and the Soot Patterns after Combustor Operations

Figure 7 shows the soot patterns on the inner wall of the rear flange within the cavity. Notice the pattern where the soot was removed due to the heat of the flame. It

was decided that the tests would have to be conducted without the quartz windows in place. With the fiber optic probe recessed within the view port the chances of damage due to heat could be avoided. The fiber optic probe was attached to the view port via a coupling welded to a threaded bolt with an 1/8" I.D. hole drilled in it. Figure 8 shows the view port connector.

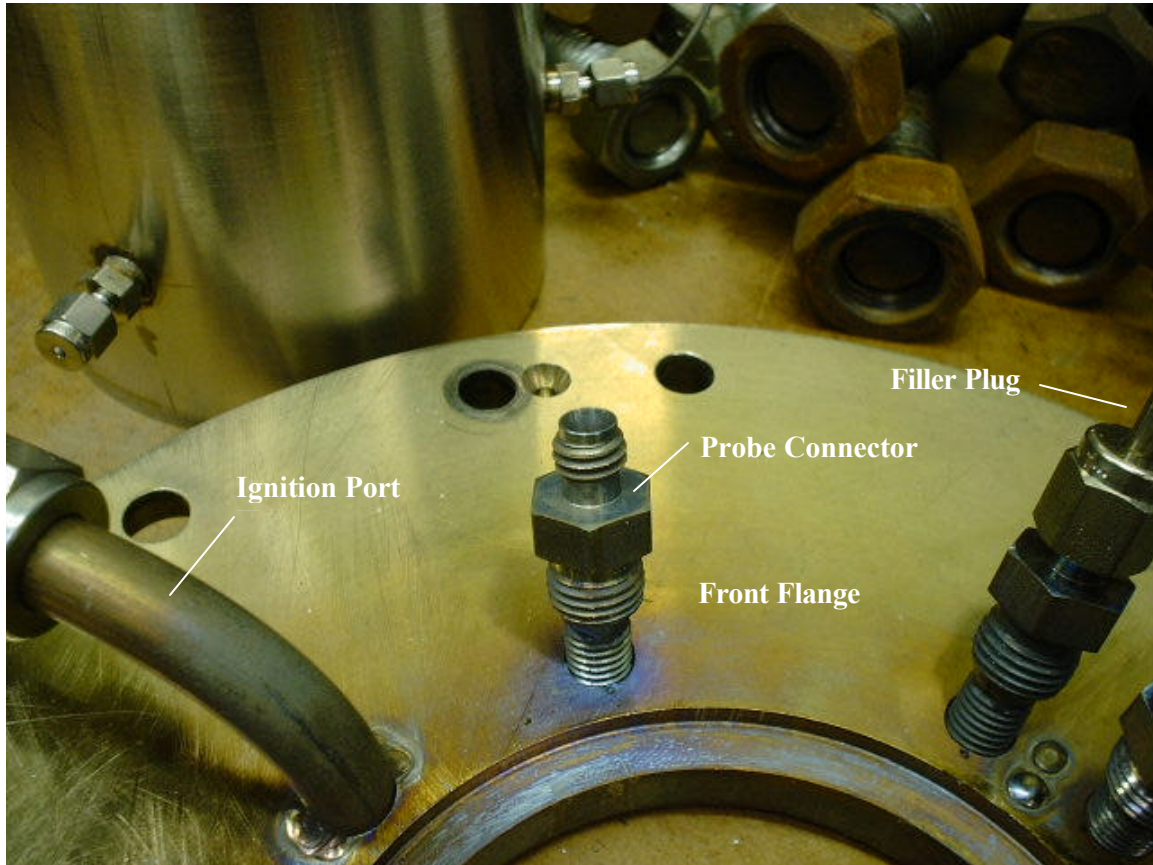


Figure 8: View of the Fiber Optic Probe connector

III.2.2 Fiber Optic Probe Construction

The fiber optic probe consists of a bundle of five Thorlabs™ product# FG-200-UCR silica/silica multi-mode fiber optic cables. The cable consists of a silica core with a diameter of $200 \pm 8 \mu\text{m}$ surrounded by a silica cladding with a diameter of $240 \pm 5 \mu\text{m}$. The core and cladding are encased in a buffer coating with a diameter of $400 \pm 30 \mu\text{m}$.

The core and cladding are capable of withstanding temperatures up to 1140 °C. The fiber has a transmission of 97% per meter or better from 300 nm to 900 nm. Five cables were selected to provide redundancy for the optic signal incase one or more cables lost the ability to transmit light. Each fiber optic cable has a half cone angle field of view of 11.5° - 13.9°.

The bundle was sheathed in a 1/8" O.D. ceramic tube in order to provide some temperature protection and rigidity for the probe. A graphite ferrule was fitted around the ceramic tube and was used in conjunction with a Swagelok™ fitting to lock the probe in place during testing. Figure 9 shows this probe configuration.

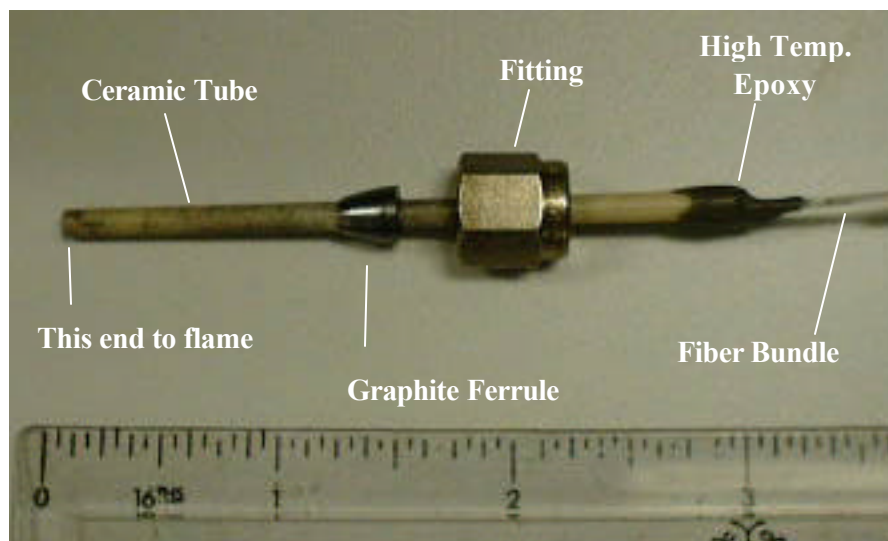


Figure 9: Fiber Optic Probe

The length of the fiber optic cable bundle used in the experiments was approximately 72 inches. This provided flexibility to reposition the probe within the UCC test rig while allowing the data acquisition equipment some stand-off from the hot test section. The end of the fiber optic bundle opposite the probe was also sheathed in a ceramic tube. This ceramic tube provided rigidity for the fibers to be clamped to optical mounting equipment and aimed at a collection lens. The collection lens and mounting

equipment were fastened to a breadboard with 0.25 inch holes and a one inch hole pattern. By varying the position of the table the fiber optic bundle could be positioned so that the lens could gather the greatest amount of light as possible. The collection lens gathered the light signal from the fiber optic probe bundle and transmitted it to the spectrometer via a sheathed fiber optic cable. Figure 10 is a photograph of the fiber optic bundle, collection lens and sheathed fiber optic cable.

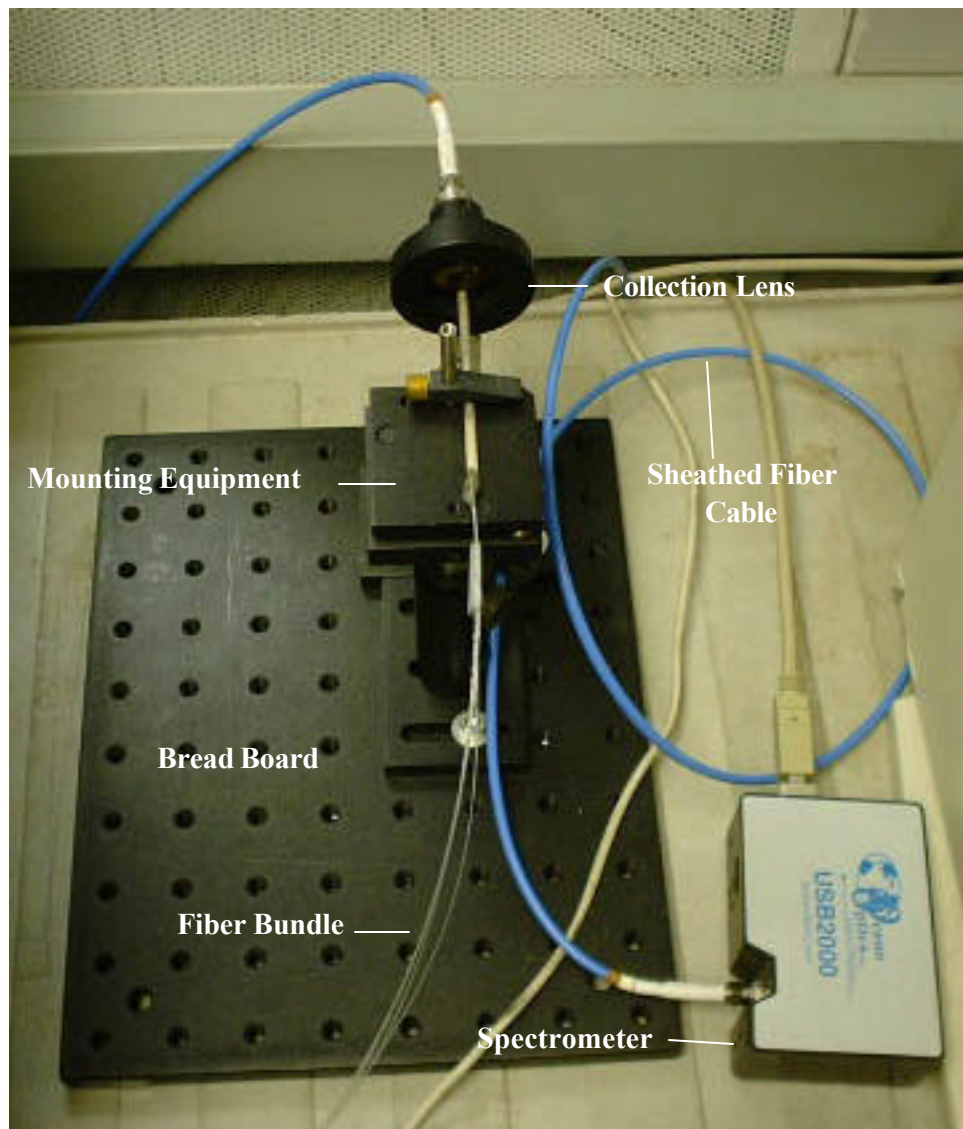


Figure 10: Fiber Optic Setup

III.2.3 Test Rig Instrumentation and Data Acquisition Software

Several types of instruments are used on the test rig. These include emissions sensors for detecting CO, CO₂, NO_x, O₂ as well as total unburned hydrocarbons, thermocouples for recording temperature at various locations, pressure transducers for recording pressures at various locations, and flow meters for recording air and fuel mass flow rates. Data from all these instruments is fed to a data acquisition system, is processed and displayed on the computer screen. Additional information on the test rig instrumentation and data acquisition system can be found on pages 36-38 of Quaaale, 2003.

III.2.4 Spectrometer Instrumentation and Spectral Analysis Software

The spectrometer used to gather light intensity data was an Ocean Optics™ Spectrometer USB2000, serial number: USB2E7356. The spectrometer has a 2048-element linear silicon CCD-array detector with a 12 bit analog to digital (A/D) converter. The spectrometer accepts light energy transmitted through single-strand optical fiber and disperses it via a fixed grating across the linear CCD array detector, which is responsive from 200-1100 nm. A #2 grating was used for this serial number which has 600 lines per mm. This grating provides efficiencies greater than 30% in the 250 to 800 nm range. Efficiencies for Ocean Optics Inc. gratings are defined as the wavelength range that the grating optimizes the first order spectra. The spectrometer has a resolution of 0.3 nm and capable of integration times from 3 milliseconds to 65 seconds. The software used to capture the data was Ocean Optics Inc. OOIbasic32, program version 2.0.1.2.

III.2.5 Calibration Lamp

A calibration lamp was used to account for the intensity signal roll-off at high and low wavelengths. An Ocean Optics Inc. DH-2000 Micropac light calibration instrument was used for this purpose. It consists of two lamps, a deuterium lamp that is used for an ultraviolet light source, 210-400 nm, and a tungsten halogen lamp that is used for a visible and near infrared light source, 360-1700 nm.

III.3 Chemiluminescence Experimental Setup

Initially the experiments were to investigate the variation in chemiluminescence observed within the cavity with changing fuel spray patterns, fuel injector angles and vane geometries. These configuration changes would be held constant while overall fuel/air ratio (OFAR) and overall pressure loss ($\%dP/P$) were varied independently. The scale of these experiments was considered too grand to accomplish in the limited time frame and was reduced to only include two configurations. Additionally to accommodate the needs of AFRL/PRTS, instead of varying fuel injectors and vane geometry, the air hole configuration was varied.

The two configurations consisted of a four air hole pattern in the cavity and a five air hole pattern. This pattern repeats itself every 60° along the circumference of the liner ring. Figure 11 is a representation of these two configurations. In both configurations the air holes are 0.213 inches in diameter. The air holes and fuel injectors are all 20° apart on the inner circumference of the liner ring. The air hole centers are offset from the fuel injector center by 0.469 inches. In Configuration 2 the middle air hole is centered

between the other four air holes and inline with the fuel injector. Configuration 2 provides 25% more air to the cavity than configuration 1.

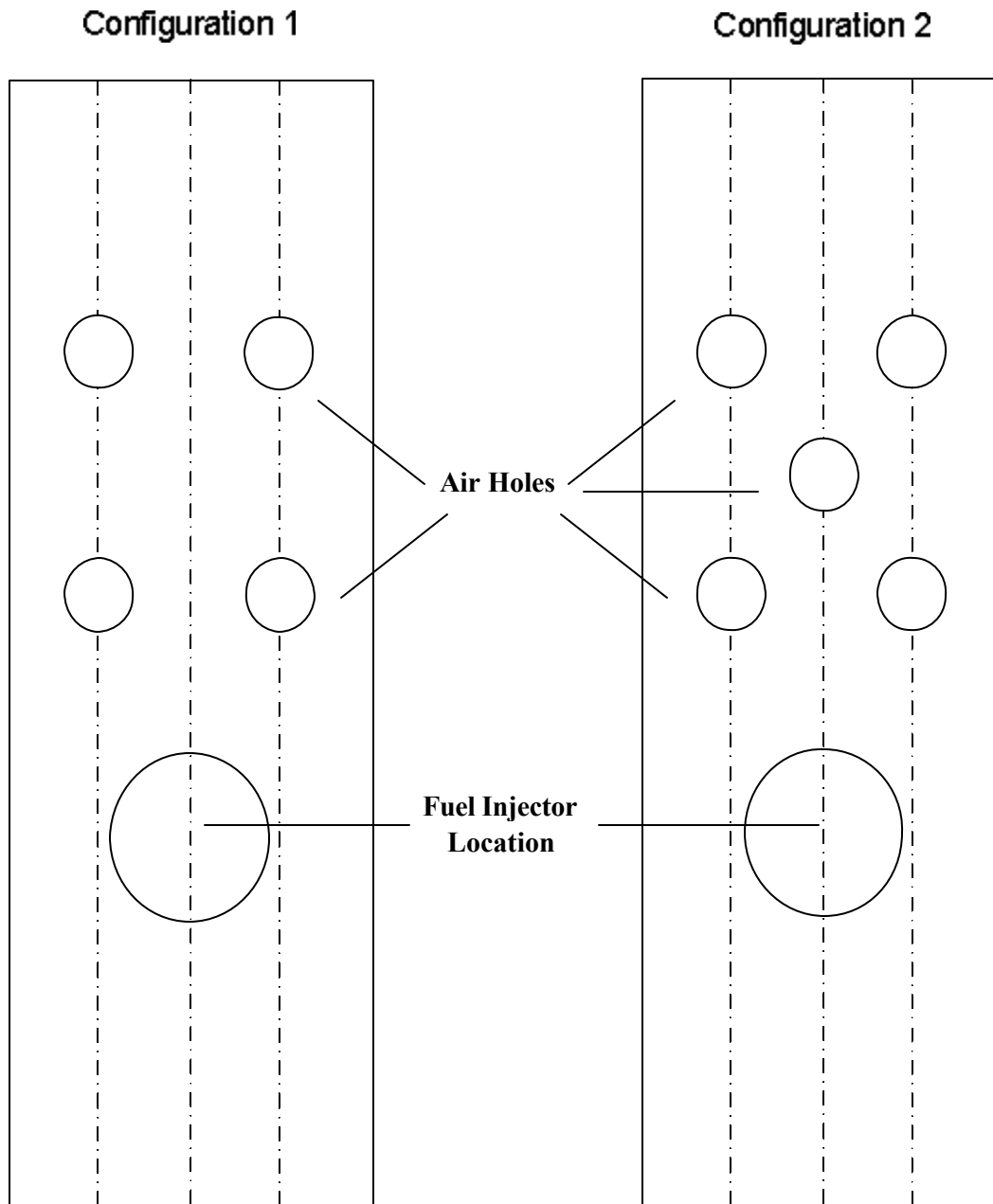


Figure 11: Air Hole Patterns for UCC configurations

The test matrix consisted of two parameters, OFAR and %dP/P. OFAR was varied from 0.0125 to 0.0250 and %dP/P was varied from 2% to 5%. Table 2 shows the

complete test matrix for chemiluminescence experiments. Eighteen different experiments were run, nine for each configuration.

Table 2: Chemiluminescence Test Matrix

Experiment ID	Configuration	%dP/P	OFAR	Φ_{CAV}
A	1	2	0.0125	0.91
B	1	2	0.0200	1.47
C	1	2	0.0250	1.82
D	1	3	0.0125	0.91
E	1	3	0.0200	1.47
F	1	3	0.0250	1.82
G	1	5	0.0150	1.09
H	1	5	0.0200	1.47
I	1	5	0.0250	1.82
J	2	2	0.0150	0.83
K	2	2	0.0200	1.09
L	2	2	0.0250	1.37
M	2	3	0.0150	0.83
N	2	3	0.0200	1.09
O	2	3	0.0250	1.37
P	2	5	0.0175	0.97
Q	2	5	0.0200	1.09
R	2	5	0.0250	1.37

The OFAR's selected for the experiments were 0.0125, 0.02 and 0.025 corresponding to a cavity equivalence ratio from 0.83 to 1.83 depending upon which configuration was used. Overall the equivalence ratio is very lean for all three OFAR's ranging from 0.184 to 0.367. At higher %dP/P the combustor could not be stabilized for these conditions due to the lean blowout limit which is related to the cavity equivalence ratio so the cavity equivalence ratios were increased via OFAR increases. The OFAR was increased since to 0.015 and in one case the lowest OFAR that could be sustained rounded to the nearest 0.0025 was 0.0175. The %dP/P selected for the experiments were 2%, 3% and 5% which are similar to overall pressure losses within the combustors of conventional turbofan engines (Lefebvre, 1983:110).

As stated earlier, eight different locations within the cavity were selected for gathering chemiluminescence data. This data was gathered for each experimental condition for a total of 144 points of data.

III.3.1 Chemiluminescence Experimental Procedure

This procedure focuses on the procedure used for gathering chemiluminescence data and only briefly describes the normal combustor operating procedure when applicable to the chemiluminescence data collection.

Prior to engine startup the computer equipment used for gathering chemiluminescence data was started up. The spectrometer was powered up for approximately 30 minutes prior to use for all experimental conditions. This allows the background voltage of the spectrometer to settle down to an equilibrium value (Brown, 2003). After 30 minutes elapsed the fiber optic probe was positioned in front of a tungsten halogen light source in order to check the alignment of the fiber optic cable ends with the collection lens. The intensity of the signal was viewed in real time using the OOIbasic32 software and alignment adjustments were made to the table to ensure the maximum signal was being gathered. This procedure was performed prior to every startup incase the table was accidentally bumped from the time when the previous experiments were performed. Once it was determined the alignment was correct the combustor was started up.

The combustor was always started without the probe positioned in one of the view ports. From previous work using this fiber optic technique it was learned that the probe could be damaged or caked over with soot during light off. Instead filler plugs were

positioned in each of the view ports at light off. Once ignition was complete the fuel mass flow rate (\dot{m}_f), the cavity air flow rate (\dot{m}_{ac}) and main air flow rate (\dot{m}_{am}) were adjusted to provide the appropriate OFAR and %dP/P.

The OFAR and %dP/P were allowed to stabilize then data such as temperature, pressure, mass flow rates, emissions concentration, etc. were collected by the acquisition software and saved to file. A filler plug was removed from one of the view ports, the port was checked for blockage and then the fiber optic probe was inserted into the port to a predetermined depth. The intensity of the spectrum was then viewed via the software and the integration time was then altered so that the peak intensity output was as close to the maximum intensity possible without truncating the signal. This maximum intensity was 4096 binary counts since the spectrometer is a 12 bit device. Relating this intensity to a physical quantity could not be accomplished since a calibration source that measures the absolute intensity was not used.

This signal was then saved to file and this process was repeated for the remaining seven view ports. This process took approximately 20 to 30 minutes to complete. Once all spectrum data was saved the temperature, pressure, etc data was saved to file to account for any drift in the OFAR, %dP/P parameters while the spectrum data was being gathered. Occasionally if the fiber optic probe measurements were taking longer than 30 minutes to gather a third set of temperature, pressure, etc data was taken.

After all the data was taken for a given number of OFAR, %dP/P combinations the combustor was shut down and the spectral data collection process was repeated in order to gather the background spectra for each hole. All equipment such as heaters, fans

and lights that were on during the tests were left running so as not to alter the background signal. The entire process was repeated until all eighteen test conditions were completed.

III.4 Fuel Spray Characterization Experimental Configuration

In addition to the chemiluminescence experiments conducted using the UCC test rig, experiments to characterize the fuel spray were also performed. These tests were conducted using a Malvern Instruments Ltd. Malvern 2600 particle size analyzer.

III.4.1 Laser Diffraction Particle Size Analyzer

The Malvern 2600 particle size analyzer uses laser diffraction to determine particle size. The Malvern 2600 is a helium-neon laser that operates at 633 nm with a maximum power output of 5 mW. The system consists of a transmitter, a receiver, and data analysis computer and software. The system comes with several lenses of varying focal lengths. The size range of the particles to be measured determines the focal length to use. For these experiments the 100 mm lens was selected since it provides for size characterization of particles from 1.9 to 188 μm which is the expected size range of fuel particles in the combustor. The 100 mm lens has a cut-off distance of 133 mm to eliminate the vignetting effect previously discussed.

III.4.2 Laser Test-bed Setup

The laser transmitter and receiver were mounted on a uni-strut frame to provide a rigid alignment. This frame was mounted to a cart to provide vertical offset capability with the sample container. This capability allows the laser to be repositioned so that

droplet sizes can be measured at various standoff distances from the tip. The three distances chosen were 0.5, 1.0 and 1.5 inches since these would correspond well with the distances within the cavity of the UCC test rig.

The sample container was a glass box constructed to keep the spray contained and to keep it from striking the receiving lens. The same type of fuel injector used in the chemiluminescence experiments was mounted to the top of the glass box. Beneath the glass box a hole was cut in the cart and a bucket was placed underneath to collect the JP-8 +100 fuel. A ventilation system was also incorporated into the setup to vent any fumes from the fuel out of the laboratory. Figure 12 is a schematic of the setup, while Figure 13 is a photograph of the setup.

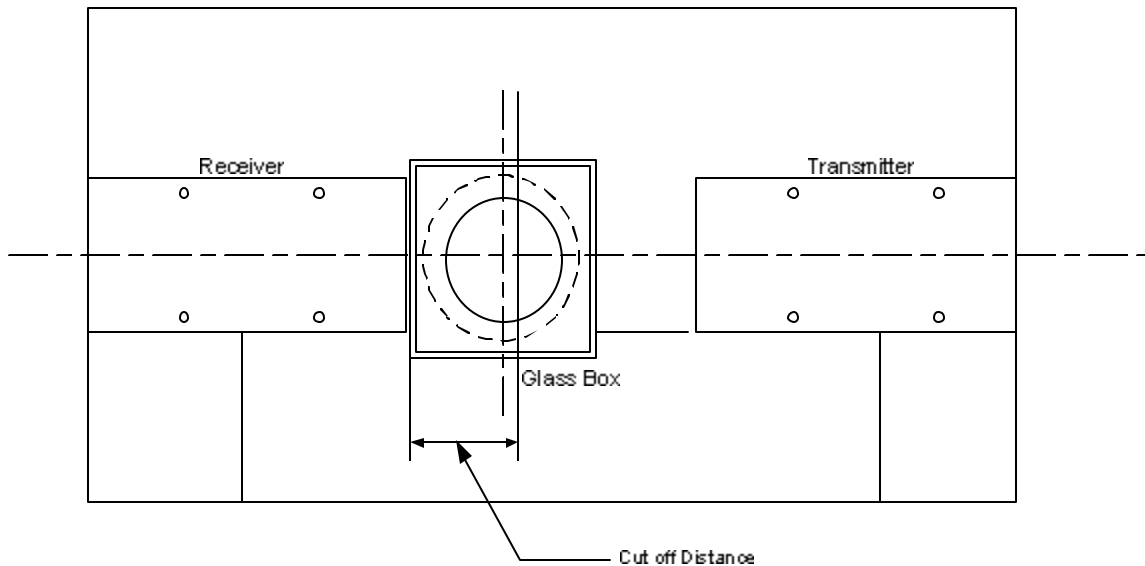


Figure 12: Top View of Malvern Setup

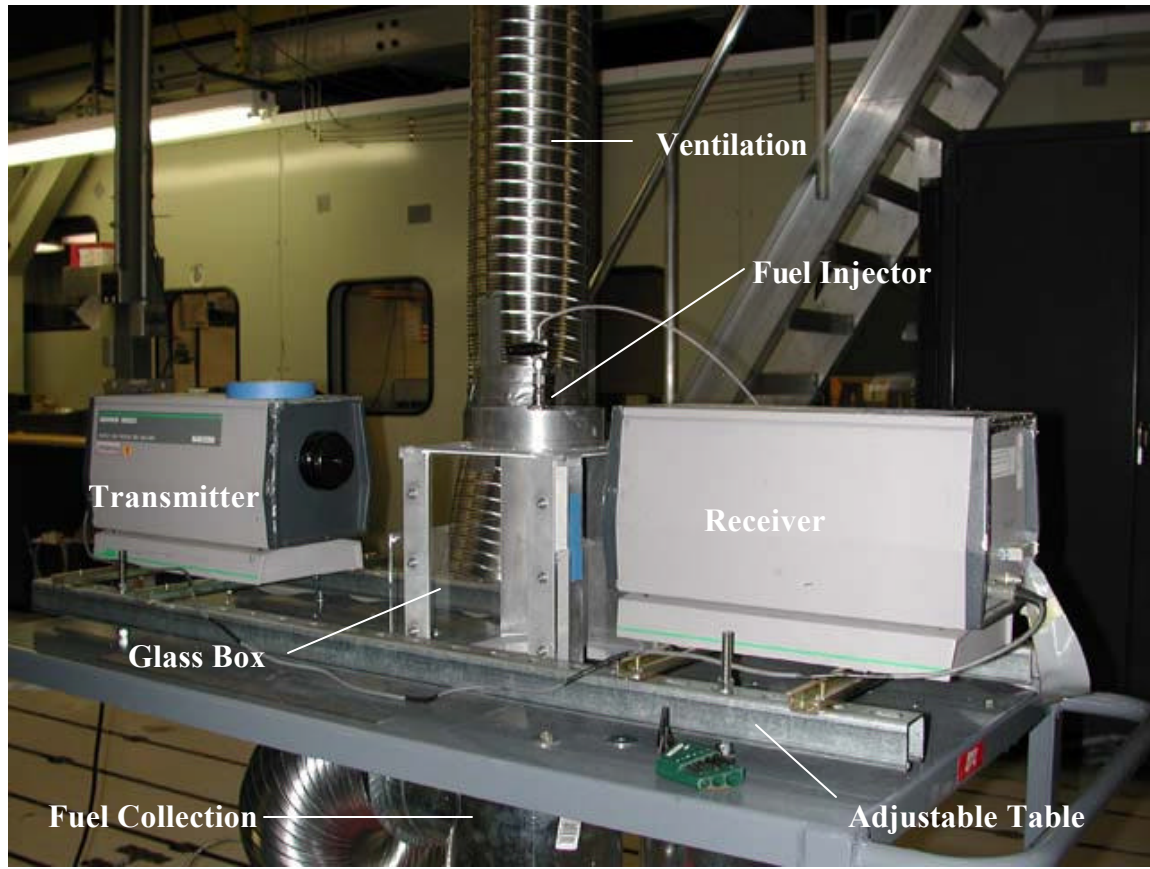


Figure 13: Malvern 2600 Laser Test bed Setup

III.5 Particle Size Experimental Setup

In order to duplicate the spray conditions within the UCC the same \dot{m}_f per nozzle that was used for each UCC test condition was used for the particle size analysis. Table 3 shows the mass flow per fuel injector used in the UCC and the pressure drop across the fuel injector calculated from the mass flow and flow number, (FN). These calculated pressure drops are similar to the pressure drops measured during the UCC experiments.

Table 3: Fuel Flow Rates for Particle Size Experiments

Flow Number = $0.5 \text{ lb}_m/\text{hr}/\text{psi}^{0.5}$		
Experiment ID	Mass Flow (lbm/min)	? P
A	0.022	6.97
B	0.031	13.84
C	0.038	20.79
D	0.027	10.50
E	0.040	23.04
F	0.047	31.81
G	0.042	25.40
H	0.053	40.45
I	0.064	58.98
J	0.026	9.73
K	0.032	14.75
L	0.037	19.71
M	0.032	14.75
N	0.040	23.04
O	0.048	33.18
P	0.048	33.18
Q	0.053	40.45
R	0.064	58.98

Since many of these flow rates are similar several were grouped together to reduce the number of experiments conducted. See Table 4 to see how the experiments were grouped.

Table 4: Particle Size Experiment Identification

Particle Test ID	Exp. ID	Mass Flow (lbm/min)
1	E	0.040
	N	0.040
	G	0.042
2	F	0.047
	O	0.048
	P	0.048
3	H	0.053
	Q	0.053
4	I	0.064
	R	0.064
5	A	0.022
6	J	0.026
	D	0.027
7	B	0.031
	K	0.032
	M	0.032
8	L	0.037
	C	0.038

The experiment requires that each of the eight groups be tested three times at each of the three fuel injector standoff distances for a total of 72 tests.

III.5.1 Particle Size Experimental Procedure

The experiments were to start at the furthest stand off distance and the higher mass flow rates since the fuel spray should be better formed further from the nozzle and at higher pressures, associated with the higher mass flows. The Malvern test bed was adjusted for the 1.5 inch stand off distance and then the x and y axis of the laser beam receiver was aligned so that the beam intensity was centered on the detector array. Once the laser is aligned a background measurement is taken in order to determine the background light scattering the laser receiver is measuring. The Malvern software

corrects for this error when calculating particle size. Since the laser beams path travels through two glass plates before reaching the receiver, by viewing a plot of the intensity scatter pattern displayed on the computer screen, it was revealed that the background scattering intensity levels were too high. It was determined that the background light refraction and reflection along with the laser beam refraction through the plate was too great to be used in this configuration. This required a change to the test bed configuration. The glass plates were shifted to remove them from the laser path and a black cloth tarp was placed over the test bed during measurements. Figure 14 shows the new configuration. A plot of the intensity scatter pattern displayed on the computer screen revealed that the new configuration was acceptable for use as a background measurement.

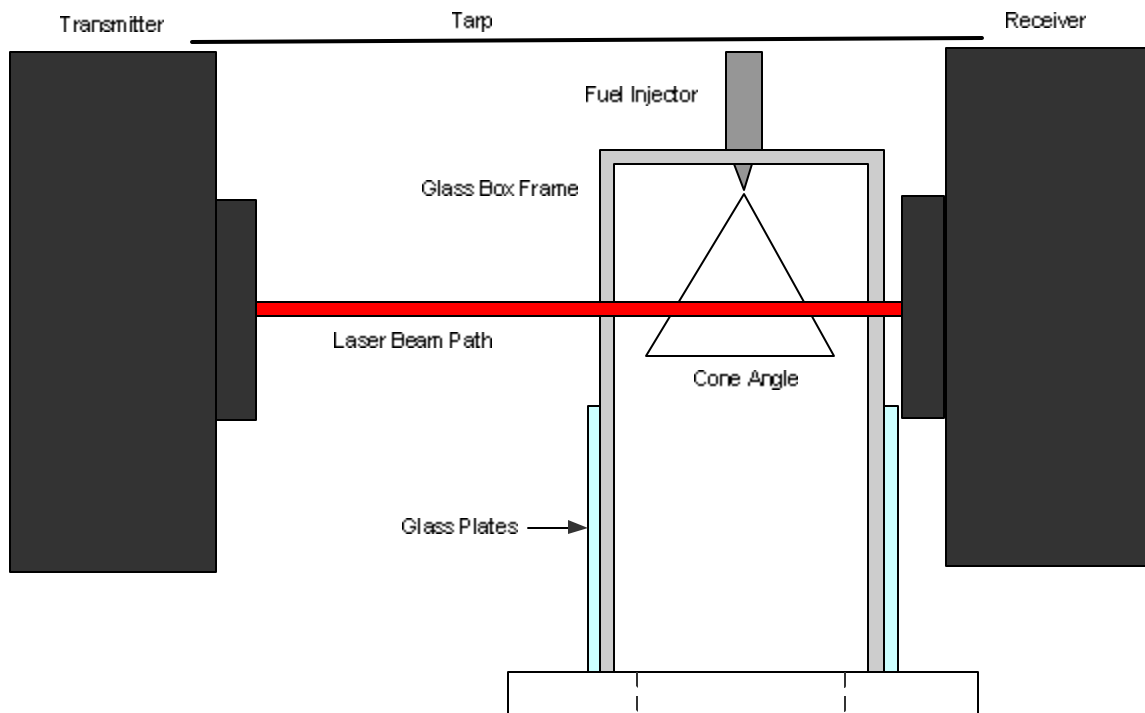


Figure 14: Side View of Malvern Setup

Once the background data was collected the fuel flow was turned on and the fuel flow rate was matched with the flow rate needed for the particular experiment. The

concentration was measured using the software to ensure the sample concentration was not so high as to cause obscuration of the laser beam. The sample was measured using the Malvern 2600 particle size analysis software and the results were output to the monitor in tabular and graphical form. Since the Malvern 2600 is an older model the software could not be configured to print to a laser jet printer and since the data files did not provide useful output a photograph of the screen output was taken to record the results of each experiment. Notes about the visual examination of the fuel spray were also taken for each experiment. This procedure was repeated until all the experiments were completed.

IV Results and Discussion

IV.1 Chemiluminescence Data Reduction

Chemiluminescence experiments were completed on four separate days of testing. Test Conditions D-F were completed first on 12 November 2003, followed by G-I and A-C on 20 November 2003. Upon completion of the configuration change, test conditions J-O were completed on 3 December 2003 followed by test conditions P-R on 4 December 2003.

Figure 15 is a plot of the spectral output of the fiber optic measurements.

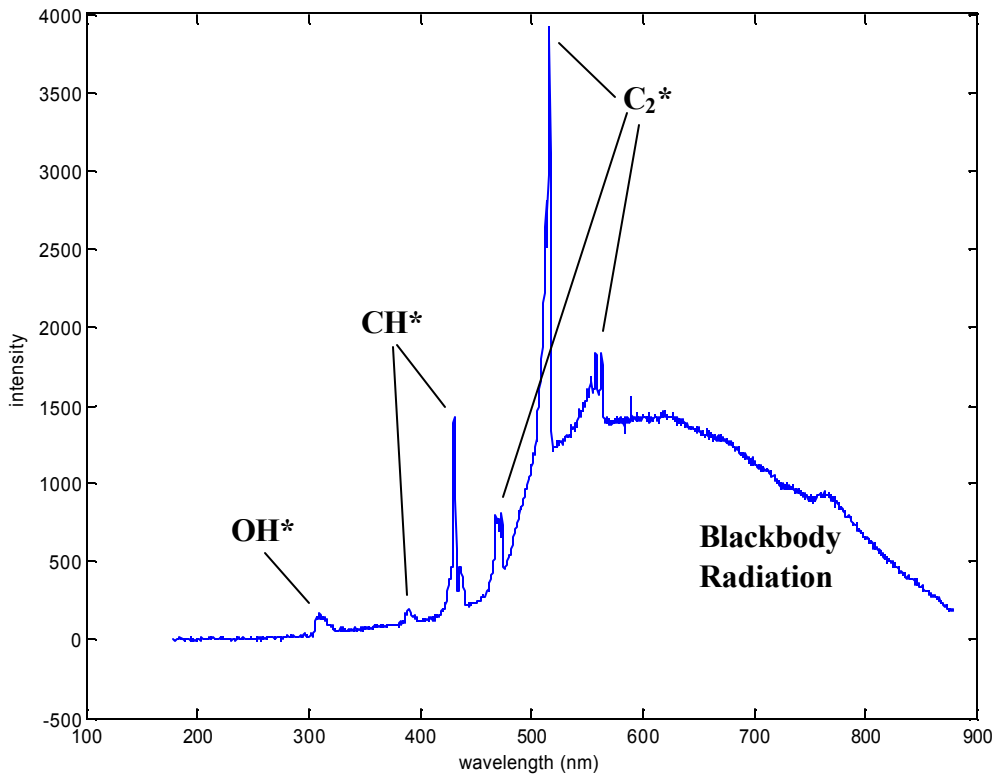


Figure 15: Typical Spectral Output from the UCC

This figure has the background spectral signal for this particular view port subtracted from the signal measured while combustion was occurring in the UCC. This signal

intensity is typical of all the view ports and all the test conditions with some minor variation in the spectral feature sizes.

In order to account for the signal degradation of the spectrometer and from the fiber optic probe a calibration measurement was taken after the completion of all the tests. The fiber optic probe head was inserted into each of the DH-2000 Micropac light calibration instrument view ports and the spectral signal was taken. A background signal was also taken and subtracted from this signal. Figure 16 is a plot for this data.

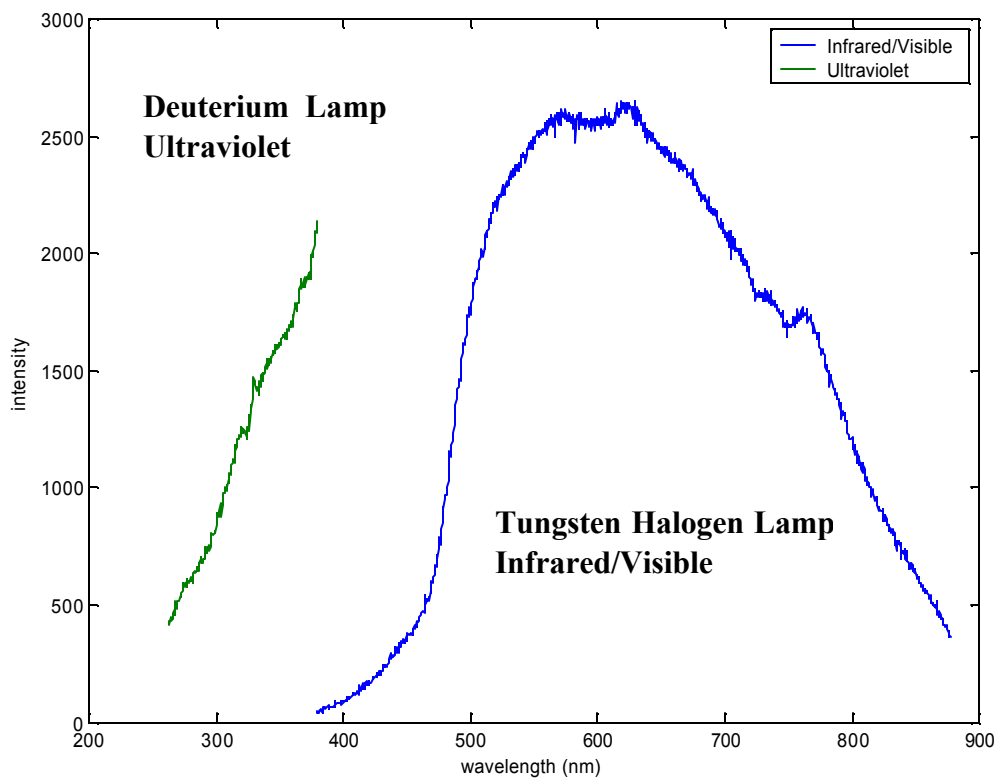


Figure 16: Observed Spectral Output from the Calibration Lamp

The true lamp intensities for the Calibration instrument are known and are provided with the lamp. Figure 17 is a plot of this data.

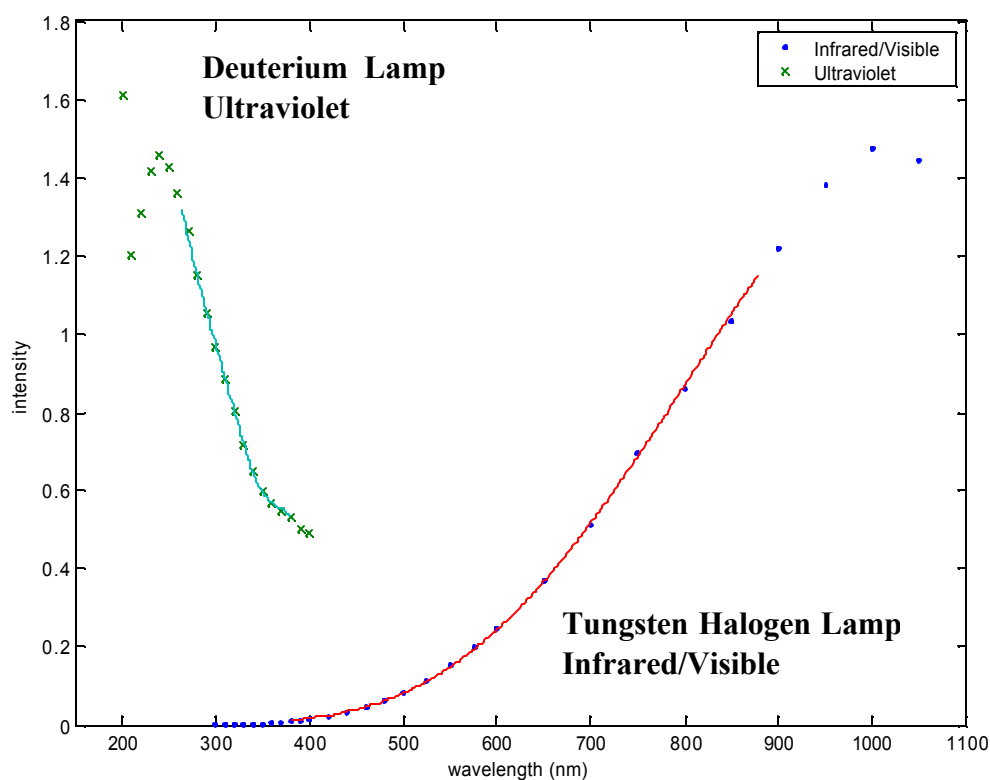


Figure 17: True Lamp Intensities with Polynomial Curve Fits

Polynomial curve fits to the data were added using the `polyfit` and `polyval` commands in Matlab®. These curve were fitted to all points within each data set, but were only plotted from 265-380 nm for the ultraviolet data points and 380-877 nm for the visible and infrared data points. The high range was selected because the spectrometer only takes data up to 877 nm. The low range was as a matter of convenience for plotting the calibration factor.

In order to calibrate the observed spectra with the known or true spectra, a calibration parameter was defined as

$$CP = \frac{I_{true}}{I_{measured}} * 1200 \quad (7)$$

where I_{true} is the *true intensity of the lamp* and $I_{measured}$ is the *measured intensity of the lamp*. This ratio is plotted in Figure 18. The number 1200 is an arbitrary scaling factor that adjusts the ratio so that the average value for the spectral range from 265-877 nm is approximately one.

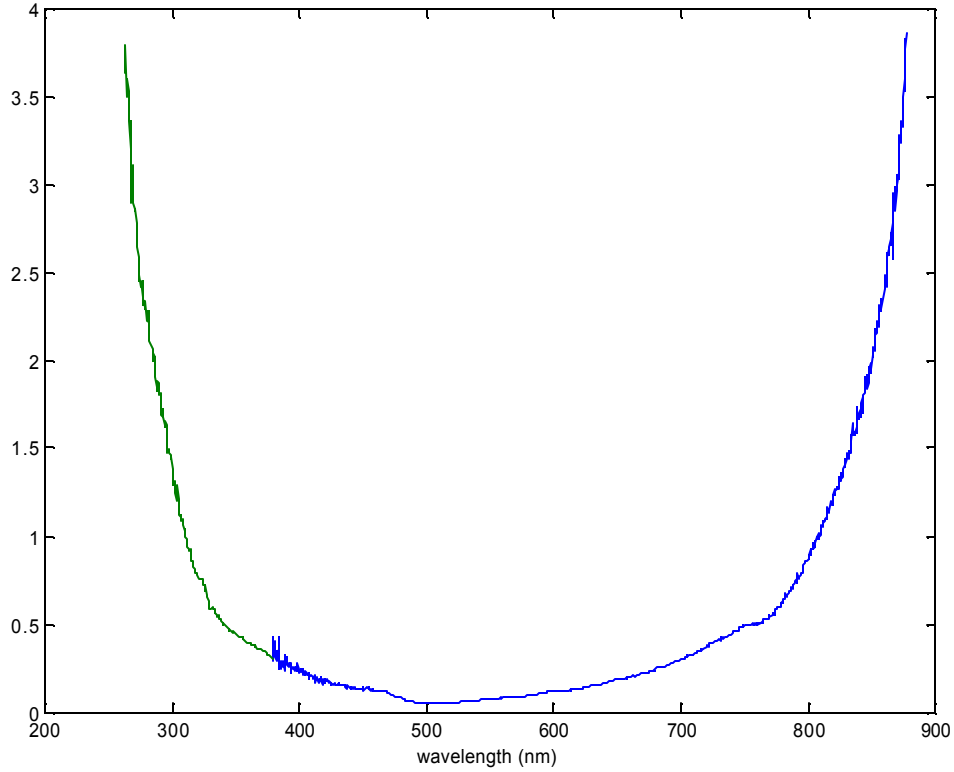


Figure 18: Scaled Ratio of True Intensity to Measured Intensity for a Given Wavelength

By multiplying the measured intensity of each spectra, taken from the experimental data, by the calibration parameter the true intensity of each spectra can be

determined. The same uncalibrated spectral output plotted in figure 15 has been plotted in figure 19 after the calibration parameter has been applied

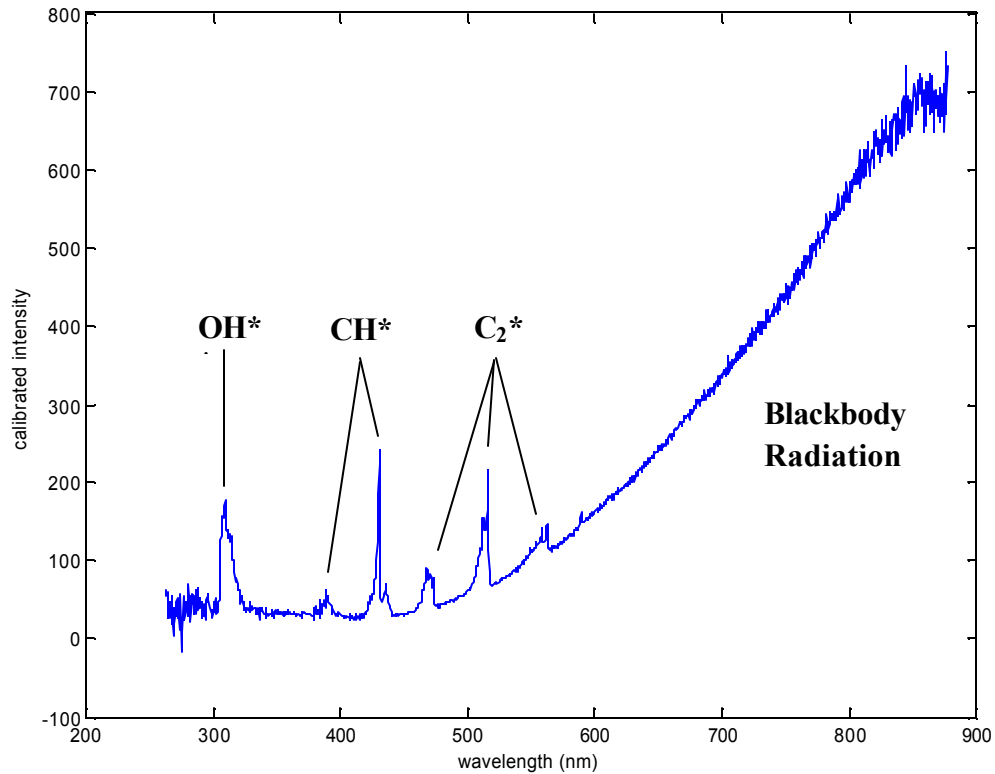


Figure 19: Typical Calibrated Spectral Output from the UCC

Note: Calibrated intensity is in terms of counts from 0 to 4096

One of the noticeable differences between the uncalibrated and calibrated spectra is the increase in size of the blackbody radiation intensity and the OH* spectral band. This is due to the large difference between the true intensity and the measured intensity at the short and long wavelengths as seen in figure 18. The larger value of the calibration parameters at these wavelengths also increases the signal noise that can be seen in figure 19 as well.

To compare variations in hole-to-hole intensities the variation in integration times needs to be accounted for. The intensity of the signal is linear in integration time. This

assumes constant number density of the species observed. Since the time scales used for gathering the intensity were from 1.5 to 10 seconds this assumption is valid (Brown, 2003). Additionally there were no changes in the combustor operating conditions during the time scales measured. All intensity data was normalized by dividing the intensity by the integration time thus changing the intensity scale (y-axis) on figure 19.

Another adjustment to the data must be made prior to use and that is an adjustment based on the axial displacement of the fiber optic probe head to the inside face of the front flange. This is shown in figure 20.

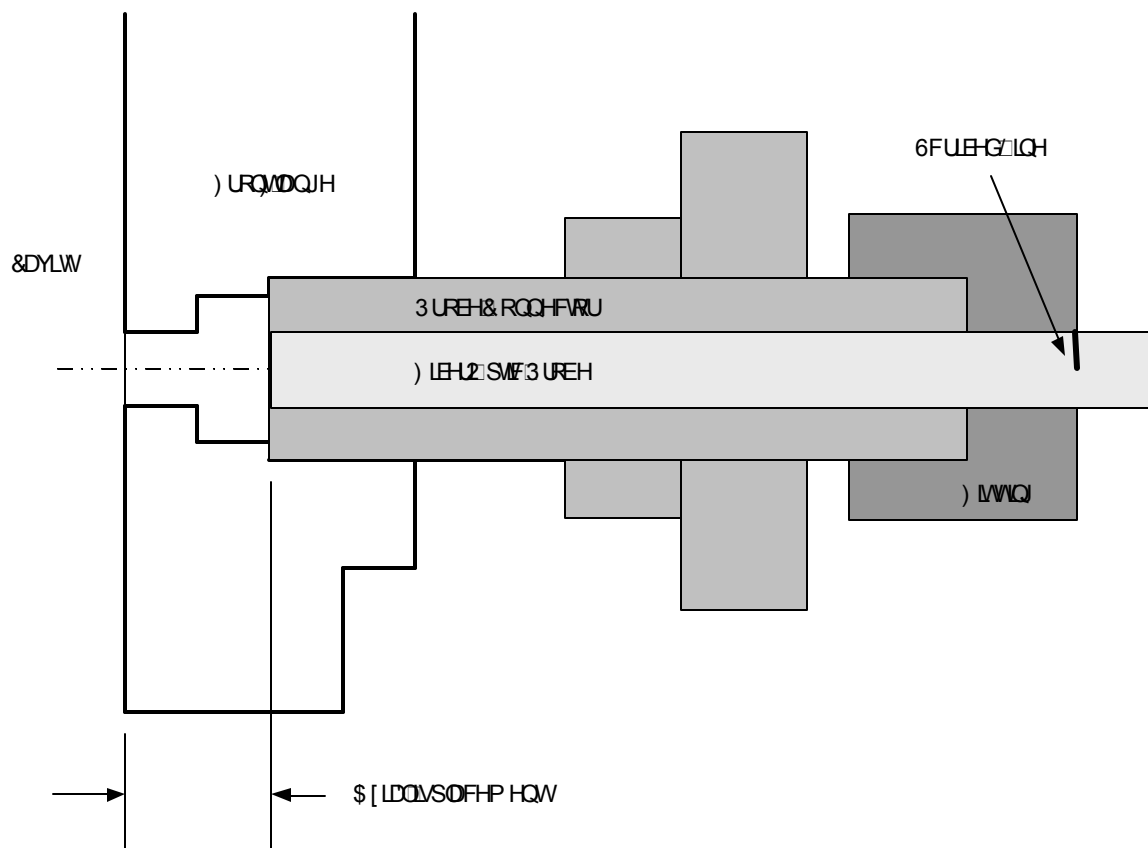


Figure 20: Close Up Cut Away View of the UCC Showing Probe Displacement Distance

The original view port design had the same axial displacement for every hole, but when the quartz window was removed the datum surface with which to butt the fiber probe against was lost. Instead a line was scribed onto the ceramic tube and the ceramic

tube was aligned so that the line was just visible when the fitting was tightened to hold the probe in place. Because the probe connectors were not uniform in length actual axial displacements were measured once the test rig was dismantled at the completion of the experiments. The axial displacements are listed in table 5.

Table 5: Axial Displacement of the Fiber Optic Probe

View Port ID	Axial Displacement (in)
A	0.215
B	0.203
C	0.161
D	0.196
E	0.164
F	0.250
G	0.223
H	0.195

As you move closer to the flame (ie: less axial displacement) the signal intensity increases. This is manifested in the shorter integration times consistently observed for the C, D and E holes when compared to the F and G holes. In order to account for this intensity variation with axial displacement the intensities for two different holes, an inner radius looking hole and an outer radius looking hole, were measured at three different displacements. These axial displacements were 0.142, 0.212 and 0.250 inches. Each signal intensity spectra was measured three times at each axial displacement. The three measurements at each axial displacement were then averaged. Figure 21 is a plot of these signal intensities versus wavelength versus axial displacement.

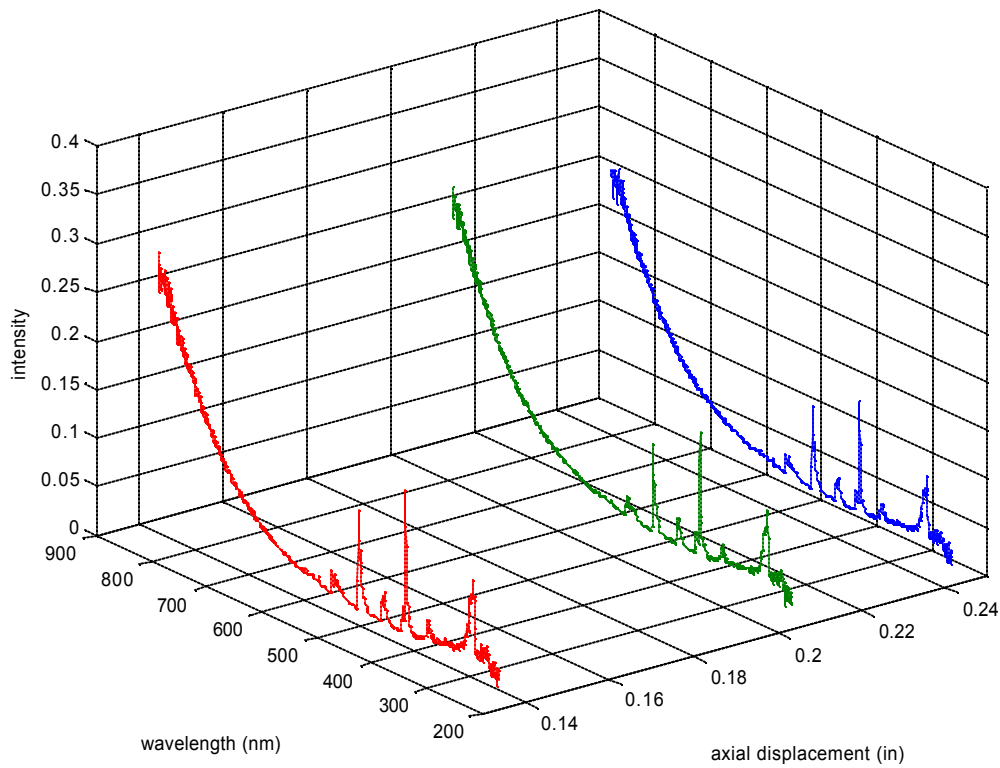


Figure 21: Variation in Spectra Signal Intensity with Axial Displacement

The intensity signal in figure 21 has been calibrated and normalized with integration time. The intensity will vary with the square of the projected radius of view. Since the intensity variation is so small over a short displacement range and since all the intensity data taken is within this displacement range a linear fit to this data was used instead of a second order polynomial fit. The slope is negative since the intensity decreases with increasing axial displacement. The slope of the intensity versus axial position line was calculated for each wavelength, then multiplied by the distance from a

reference datum to each holes' axial displacement, and added to each holes' signal intensity. The reference datum used was an axial displacement of 0.200 inches.

$$I_R = I_{C,N} + M \times (0.200 - L_{AD}) \quad (8)$$

Where I_R is the *reference intensity*, $I_{C,N}$ is the *calibrated, normalized intensity*, M is the *slope* and L_{AD} is the *axial displacement length*. This standardization allows the spectra of one hole to be superimposed onto the spectra of another hole for comparison purposes. This also allows the intensity ratios such as CH^*/OH^* and C_2^*/OH^* and the relative intensities of individual species such as C_2^* to be compared from hole to hole. A typical comparison of spectral features is plotted in figure 22.

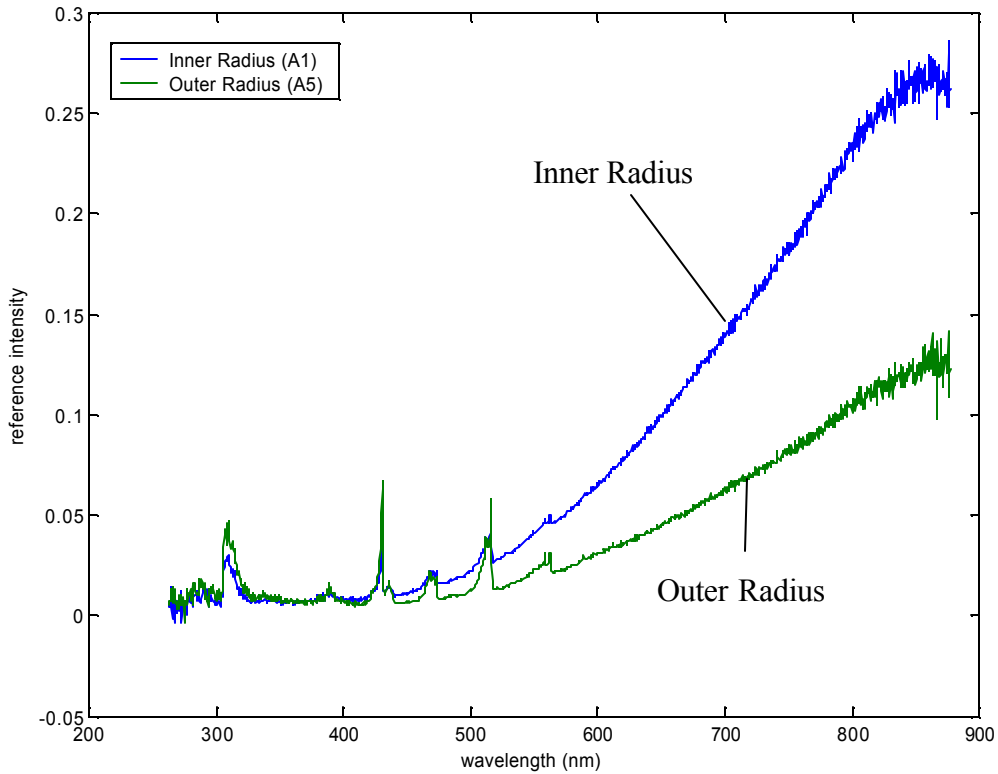


Figure 22: Comparison of Intensities from an Inner Radius and an Outer Radius Hole
Note: reference intensity is in terms of counts /ms

Figure 23 shows a close up of the radical emissions.

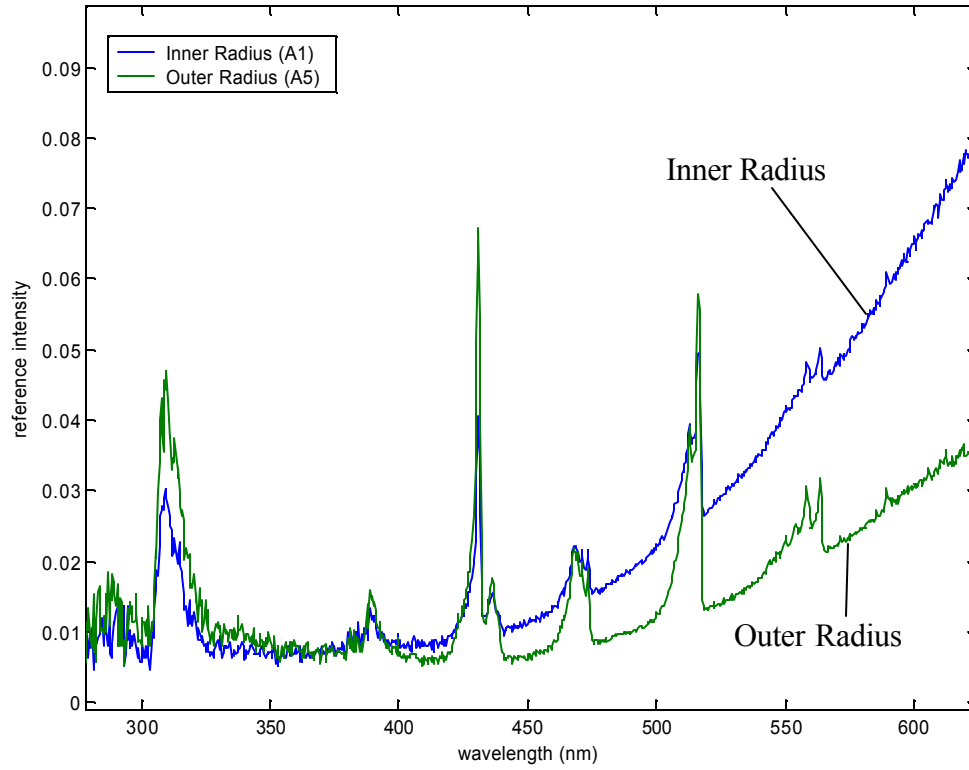


Figure 23: Close Up of Radical Emissions Spectral Bands

For these particular plots the UCC conditions were $OFAR = 0.0125$ and $dP/P = 2\%$. The locations where these signal intensity spectra were taken from were A1 = Inner Radius, 10° downstream of the fuel injector centerline and A5 = Outer Radius, 16° downstream of fuel injector centerline. See table 8.

Now that the data for each hole and each test condition has been converted to a reference signal intensity spectra, CH^*/OH^* and C_2^*/OH^* ratios can be determined. In order to reduce the effects of signal noise on these calculations, area ratios were used instead of peak intensity ratios. The area under each spectral feature was numerically integrated over a specified wavelength to come up with the total area. CH^* and C_2^* are strong emitters, but their signals can be obscured in some flames due to broadband CO_2^*

and soot blackbody radiation. OH* is in the ultraviolet wavelengths where reduced blackbody radiation exists thus increasing its observability (Morrell and others, 2001).

Because of this background radiation the area between the specified wavelengths below the spectral feature is subtracted from the total area. This new area is what is used in the ratio calculations. This method is presented graphically in Figure 24 for the OH* spectral feature.

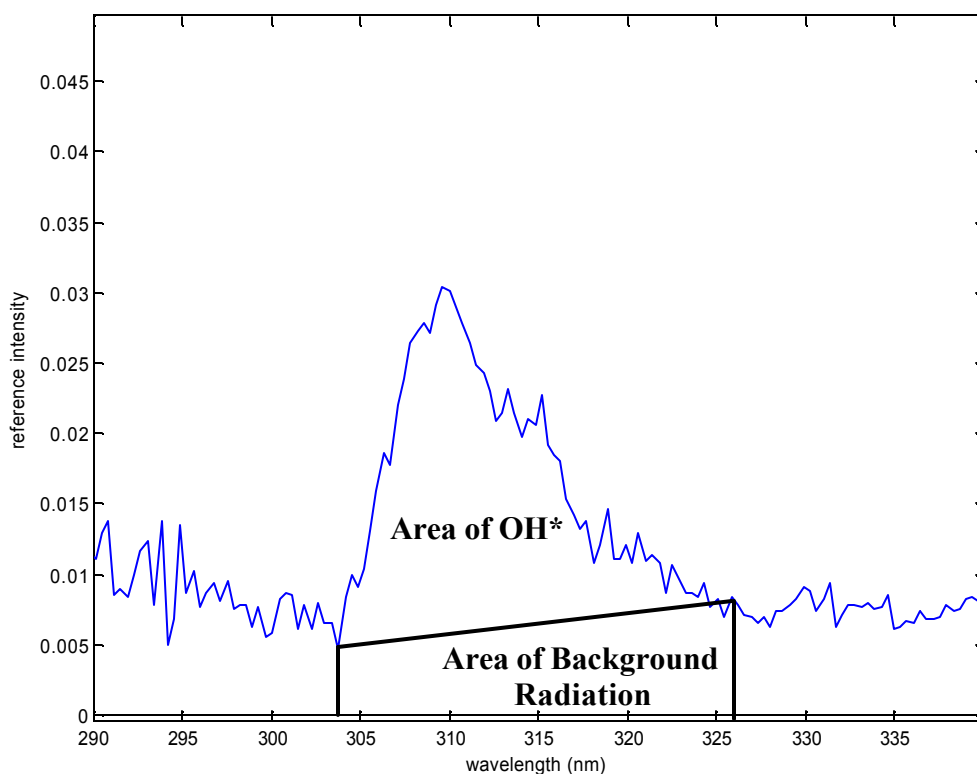


Figure 24: Calculation of the Area of the OH* Spectral Feature

Only the CH* spectral band at 431 nm and the C2* spectral band at 516 nm are used to calculate the CH* and C2* areas respectively. The wavelength ranges used in the area calculation are listed in table 6.

Table 6: Wavelength Range for Area Calculations

Spectral Feature	Wavelength Range (nm)
OH* (308 nm)	304 - 326
CH* (431 nm)	420 - 440
C ₂ * (516 nm)	500 - 519

These ratio calculations for CH*/OH* and C₂*/OH* were automated using Matlab®.

IV.2 CH*/OH* Chemiluminescence Results

CH*/OH* ratios are listed in Table 7.

Table 7: CH*/OH* Ratio

Test ID	View Port Location							
	A	B	C	D	E	F	G	H
A	0.7111	0.6410	0.6602	0.7281	0.6902	0.6955	0.6732	0.6021
B	0.8164	0.7271	1.0927	0.6467	0.9360	0.7249	0.8153	0.7116
C	0.8244	0.8583	0.7429	0.8880	0.8961	0.8123	0.8216	0.6561
D	0.5787	0.3248	0.5751	0.7404	0.6214	0.5277	1.0171	0.3459
E	0.7458	0.5338	0.8776	0.6913	0.8985	0.6649	0.8169	0.5262
F	0.8279	0.7019	1.3447	0.7352	0.9526	0.6658	0.7499	0.6881
G	0.6143	0.5695	0.7267	0.8489	0.7394	0.7422	0.7469	0.6384
H	0.7333	0.8028	0.7712	0.7618	0.8316	0.7817	0.8921	0.7815
I	0.8087	0.8716	0.9049	0.8288	0.8387	0.7755	0.7776	0.7603
J	0.6307	0.5803	0.7504	0.7540	0.8001	0.7330	0.6680	0.6303
K	0.6423	0.7534	1.0273	1.0827	1.2978	0.7806	0.8633	0.6252
L	0.6377	0.9570	1.0705	0.8218	1.0896	0.7691	1.1419	0.9045
M	0.5367	0.6027	0.7864	0.7664	0.9012	0.7544	0.6070	0.5941
N	0.6666	0.7793	0.9216	0.8602	1.0901	0.8438	0.7651	0.6473
O	0.6661	0.8598	0.9082	0.8549	0.8659	0.8279	0.9103	0.7297
P	0.5781	0.5965	0.6572	0.7022	0.7278	0.8404	0.6275	0.5825
Q	0.5492	0.6128	0.7210	0.8032	0.7290	0.8132	0.5739	0.5726
R	0.5967	0.6927	0.7952	0.8182	0.9018	0.7927	0.7215	0.6276

The CH*/OH* ratio shaded in dark gray is the maximum CH*/OH* ratio for a given experimental test condition. The CH*/OH* ratio shaded in light gray is the minimum CH*/OH* ratio for a given experimental test condition. As seen in figures 4 and 5, view

port location's C-F view the outer radius of the cavity and some of the inner radius at the rear of the cavity while view port location's A-B and G-H view the inner radius of the cavity and portions of the main section of the combustor. This table shows that the majority of the highest CH^*/OH^* ratios are located in the outer radius of the cavity. This trend becomes readily noticeable in figure 25 which is a histogram of this data.

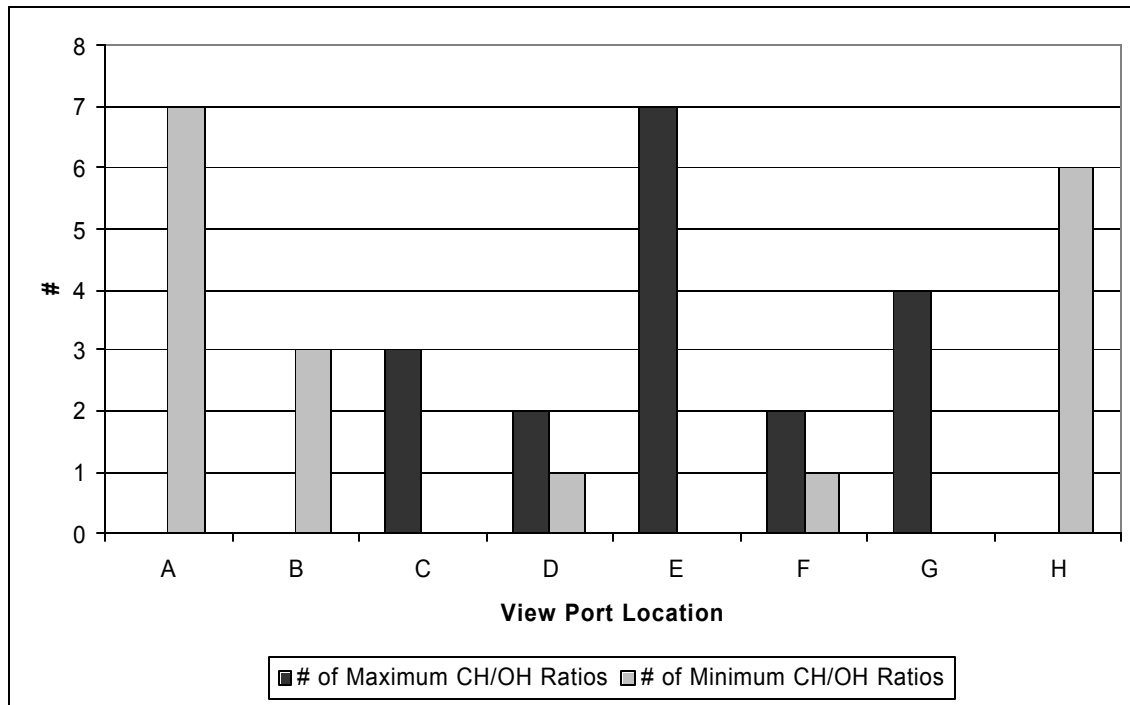


Figure 25: Histogram of CH^*/OH^* Ratio

In order to help visualize the cavity and the fuel spray cone angle within the cavity, another schematic of the cavity was drawn which includes the vanes. Figure 26 shows the rear of the UCC with the rear flange removed so as to view the cavity. Main air flow is coming out of the page while cavity air flow is clockwise within the cavity.

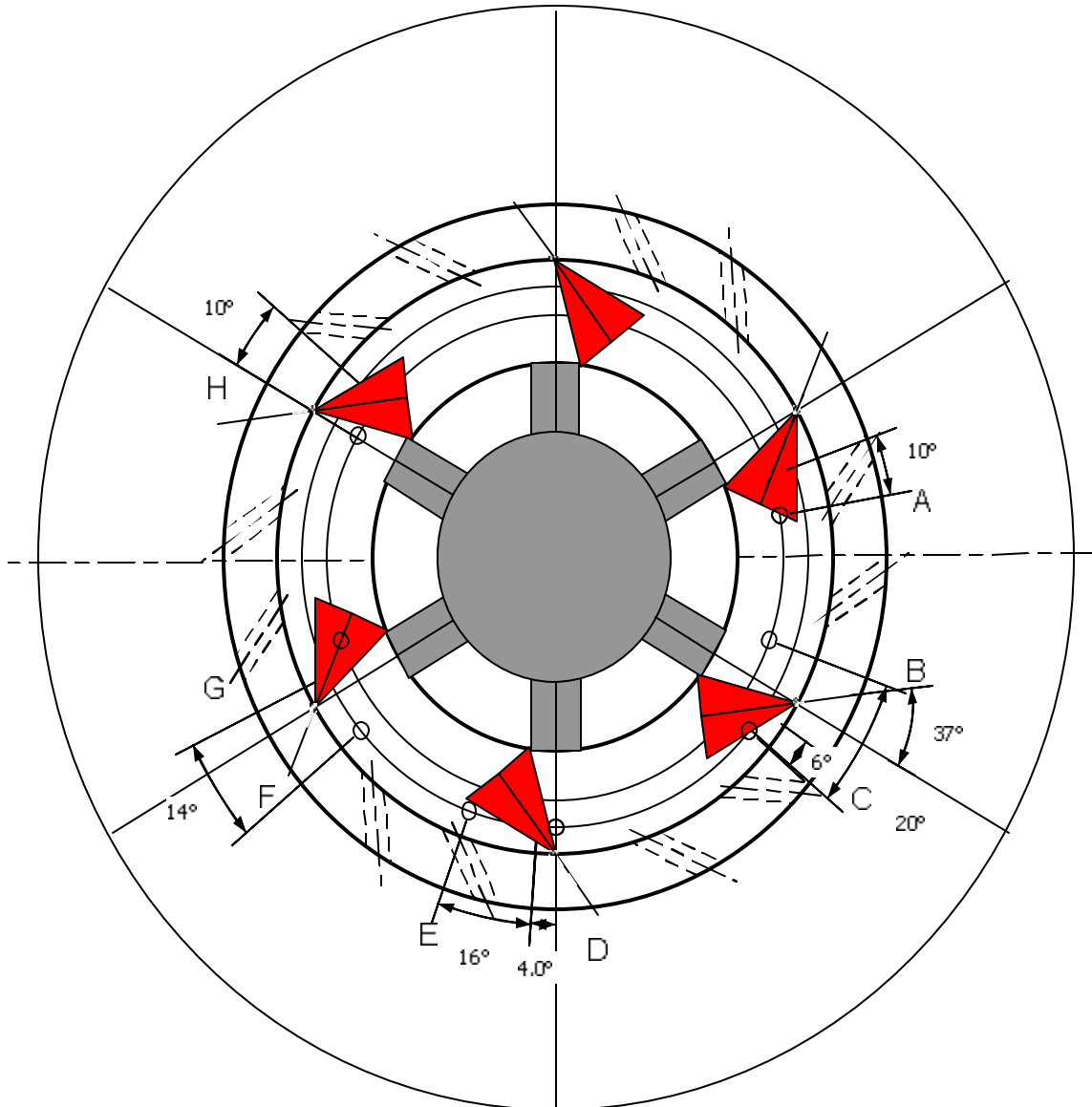


Figure 26: Rear view of the UCC showing the fuel injector cone angle

Because the fuel injectors are angled 37° from the radial the original description of the locations of the view ports (see table 1) is not really a good indication of where they lie in relation to the fuel injector. A new description was used to describe these view port locations in terms of the angle along the radial between where the view port center is located on a circumferential diameter and where the projected fuel injector centerline crosses this circumferential diameter. Angles downstream of the fuel injector are taken to

be positive and angles upstream of the fuel injector are taken to be negative. These angles are plotted on figure 26 without the sign convention. Table 8 lists this information as well.

Table 8: View Port Location with respect to the Fuel Injector

View Port ID	View Port Location
A	Inner Radius, 10° Downstream of FI centerline
B	Inner Radius, 20° Upstream of FI centerline
C	Outer Radius, 6° Downstream of FI centerline
D	Outer Radius, 4° Upstream of FI centerline
E	Outer Radius, 16° Downstream of FI centerline
F	Outer Radius, 14° Upstream of FI centerline
G	Inner Radius, Inline with the FI Centerline
H	Inner Radius, 10° Upstream of FI centerline

Since all the view ports are at various radial locations a drawing that superimposes these locations onto one fuel injector cone angle projection was created to help visualize the chemiluminescence changes with respect to view port location. Since the cavity configuration repeats itself every 60° it's reasonable to assume the conditions within the cavity repeat every 60° so superimposing the view ports onto one fuel injector cone angle projection is a reasonable assumption to make to compare chemiluminescence changes. This assumption is the same one used in the past to create the CFD model for the UCC (Quaale, 2003:4). Figure 27 shows these view ports superimposed onto one fuel injector.

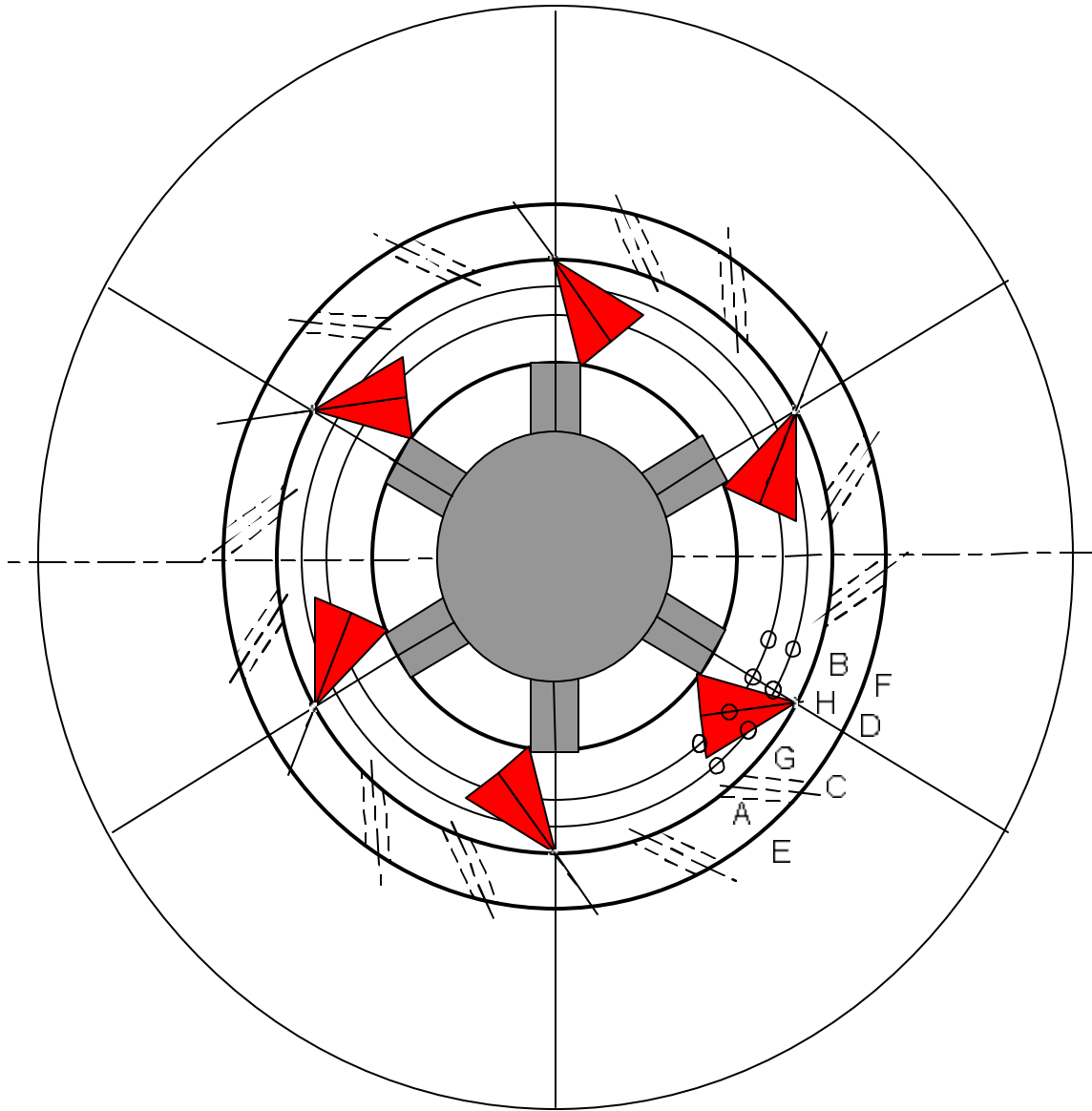


Figure 27: Superposition of View Ports on to One Fuel Injector Cone Angle

As discussed earlier chemiluminescence experiments performed by various researchers show an increase in the CH^*/OH^* ratio with increasing equivalence ratio. The average CH^*/OH^* ratio was plotted versus cavity equivalence ratio and this same trend can be seen in figure 28 for the results for configuration 1. This is not the case for Configuration 2. The average CH^*/OH^* ratios for configuration 2 are scattered again suggesting that relative to Configuration 1, reduced mixing is occurring in the cavity.

The scattering of intensities for individual view ports is presented in figures 54-61 in the Appendix. Again configuration 2 shows more scatter in the intensities versus cavity equivalence ratio per view port than in configuration 1.

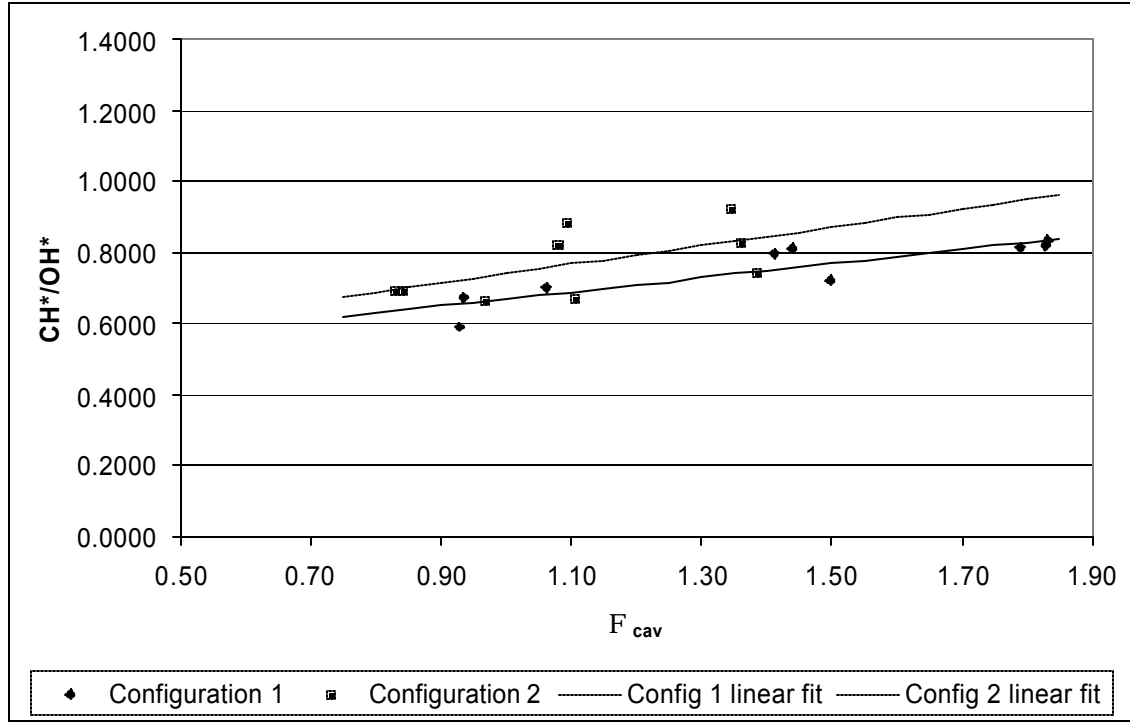


Figure 28: Average CH*/OH* Versus Cavity Equivalence Ratio for Both Experimental Configurations

The linear curve fits shown were calculated using the formula

$$y = p_1 \hat{x} + p_2 \quad (9)$$

$$\hat{x} = \frac{(x - \mu_1)}{\mu_2} \quad (10)$$

where μ_1 is the $mean(x)$ and μ_2 is $std(x)$. These values were calculated using Matlab® and are listed in table 9 along with the coefficients.

Table 9: Coefficients and Centering & Scaling Parameters for CH*/OH*

Configuration 1		Configuration 2	
P ₁	0.073	P ₁	0.056
P ₂	0.751	P ₂	0.769
μ ₁	1.413	μ ₁	1.113
μ ₂	0.369	μ ₂	0.215

IV.3 C₂*/OH* Chemiluminescence Results

The C₂*/OH* ratios are listed in Table 10.

Table 10: C₂*/OH* Ratio

Test ID	View Port Location							
	A	B	C	D	E	F	G	H
A	0.7498	0.6931	0.5785	0.6474	0.6935	0.6654	0.6788	0.7262
B	0.9734	0.7605	1.0679	0.6777	0.9135	0.7567	0.8073	0.7590
C	0.8715	0.8977	0.7995	0.9278	0.9530	0.8282	0.8242	0.6680
D	0.7171	0.4114	0.4859	0.6347	0.5721	0.5007	1.0002	0.4733
E	0.8202	0.6501	0.9304	0.7189	0.9742	0.6627	0.8817	0.5995
F	0.9447	0.7620	0.9629	0.7836	1.0795	1.0097	0.8291	0.7996
G	0.7651	0.6782	0.8095	0.9080	0.7881	0.7641	0.8654	0.7391
H	0.9113	0.9046	0.7942	0.7818	0.8564	0.7858	0.9961	0.8585
I	0.8957	0.9045	0.9568	0.8614	0.9613	0.8009	0.8636	0.8357
J	0.6261	0.5339	0.6034	0.6608	0.7305	0.6909	0.6455	0.6435
K	0.6090	0.7569	0.9931	1.0759	1.2339	0.7831	0.8822	0.6068
L	0.6321	1.0274	1.0839	0.8320	1.1483	0.7936	1.1954	0.9539
M	0.5053	0.5665	0.6136	0.7145	0.8166	0.7152	0.6194	0.6205
N	0.6376	0.7821	0.8719	0.8582	1.0683	0.8332	0.7932	0.6620
O	0.6630	0.9443	0.9417	0.9118	1.0637	0.8392	1.0019	0.7459
P	0.4911	0.5613	0.5151	0.6295	0.6319	0.7756	0.5694	0.5581
Q	0.4803	0.5743	0.5972	0.7297	0.6564	0.7678	0.5524	0.5547
R	0.5225	0.6806	0.7245	0.7580	0.8671	0.8016	0.7275	0.6619

The C₂*/OH* ratio shaded in dark gray is the maximum C₂*/OH* ratio for a given experimental test condition. The C₂*/OH* ratio shaded in light gray is the minimum C₂*/OH* ratio for a given experimental test condition. This table shows that the majority of the highest C₂*/OH* ratios are located in the outer radius of the cavity; a trend similar to the CH*/OH* ratios and is seen in figure 29.

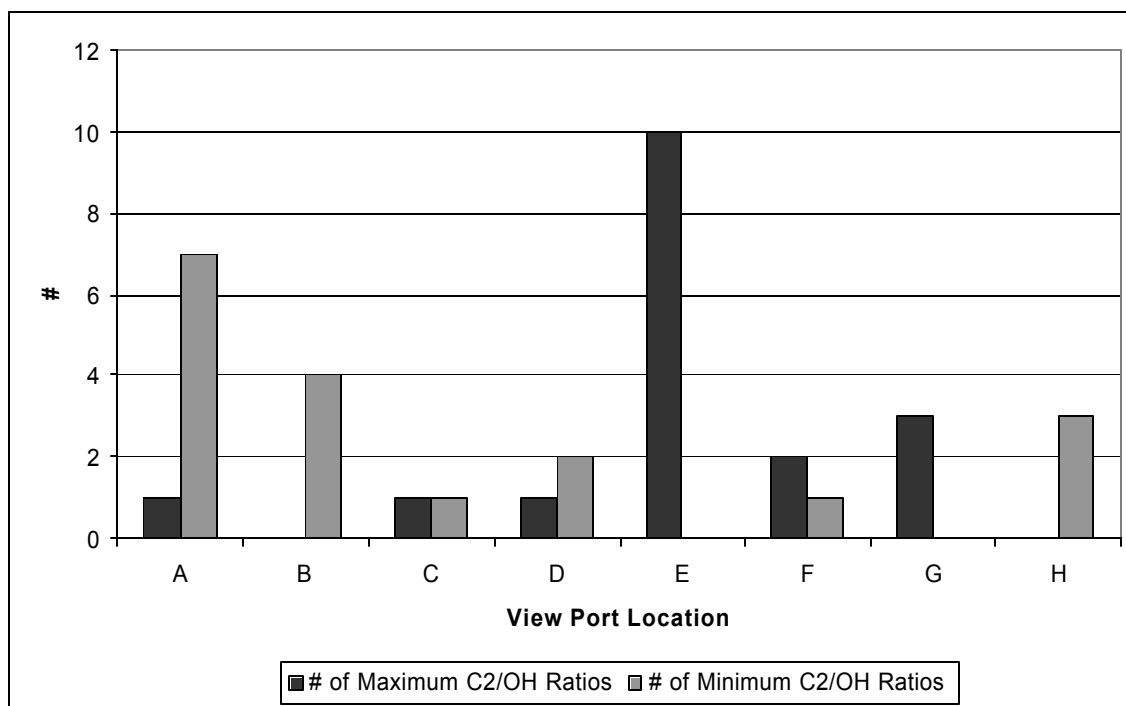


Figure 29: Histogram of C_2^*/OH^* Ratio

It was noted by Morrell that C_2^*/OH^* ratio was more sensitive to changes in equivalence ratio. Again this trend can be seen in figure 30 when C_2^*/OH^* is plotted versus cavity equivalence ratio for configuration 1 and compared with the plot of CH^*/OH^* versus cavity equivalence ratio, figure 28. Additionally configuration 2 shows similar scattering as the CH^*/OH^* data. Morrell's C_2^*/OH^* spectrometer data, with the background subtracted, for n-heptane is reproduced and plotted along with this data in figure 31 (Morrell and others, 2001).

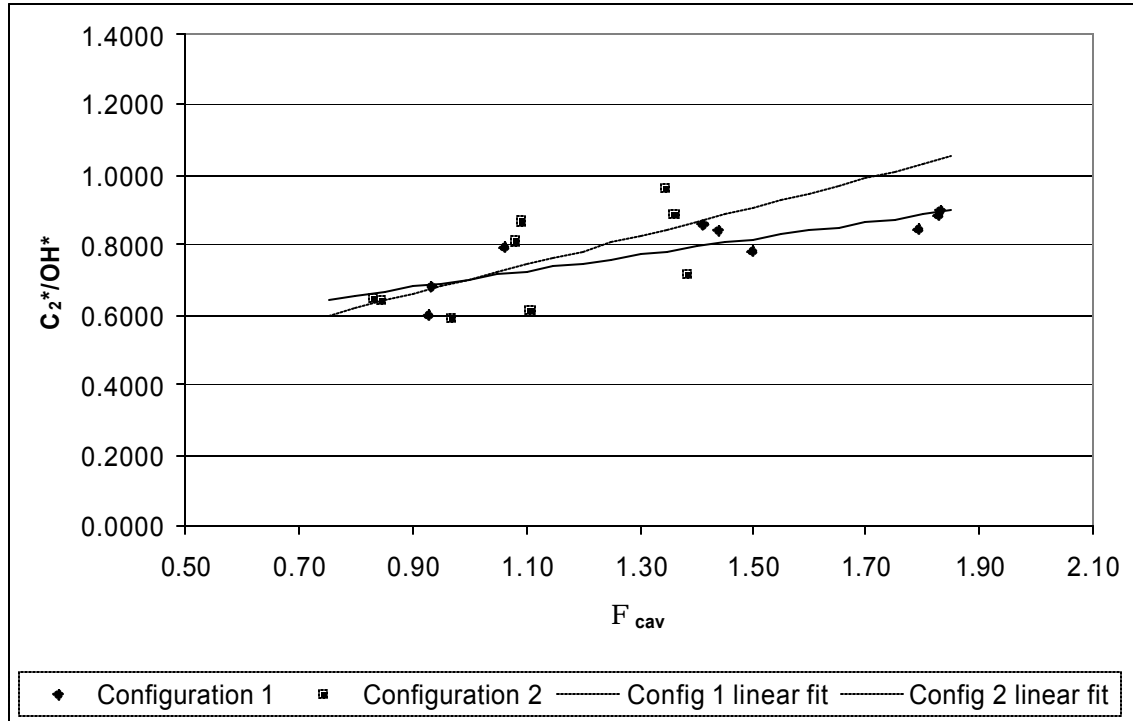


Figure 30: Average C_2^*/OH^* Versus Cavity Equivalence Ratio for Both Experimental Configurations

Again the curve fits shown for C_2^*/OH^* versus cavity equivalence ratio were calculated in the same manner as those for CH^*/OH^* . Table 11 lists the curve fit data.

Table 11: Coefficients and Centering & Scaling Parameters for C_2^*/OH^*

Configuration 1		Configuration 2	
P_1	0.085	P_1	0.088
P_2	0.797	P_2	0.749
μ_1	1.413	μ_1	1.113
μ_2	0.369	μ_2	0.215

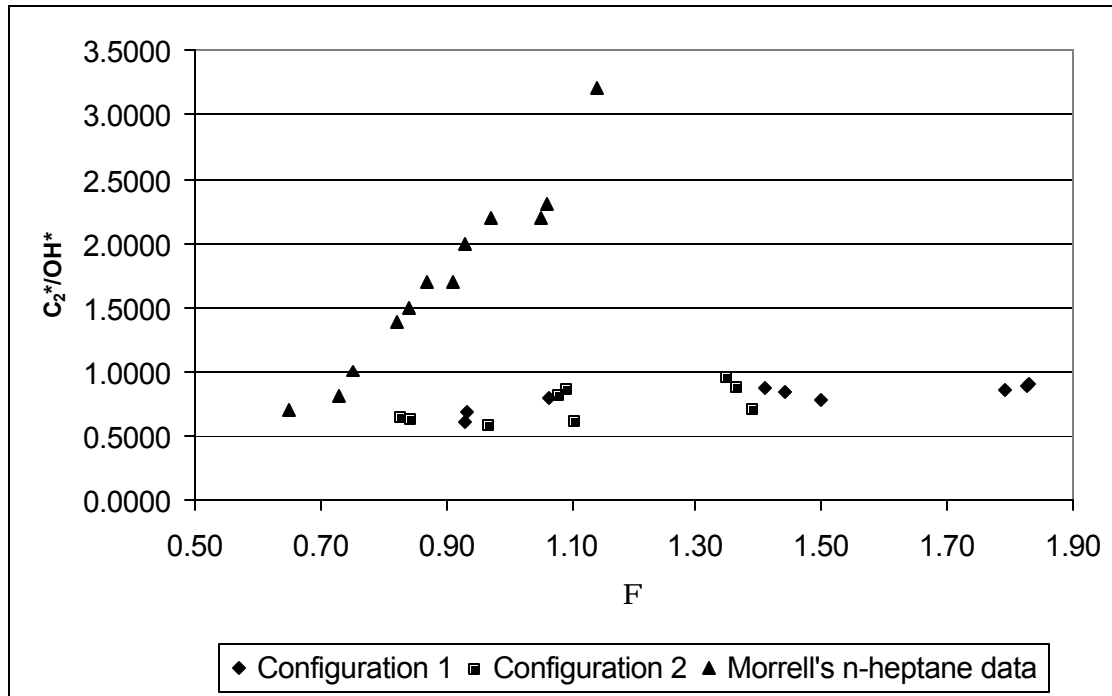


Figure 31: Average C_2^*/OH^* Versus Cavity Equivalence Ratio for Both Experimental Configurations and Morrell's n-Heptane Data

The most noticeable difference between the two sets of data and Morrell's data is the sensitivity of C_2^*/OH^* with changes in equivalence ratio. Morrell's data reveals that C_2^*/OH^* is much more sensitive to changes in equivalence ratio than the C_2^*/OH^* for the data collected from the UCC. Comparison of this data could suggest that the UCC is more turbulent than the combustor used for Morrell's experimental set-up. The basis for this conclusion is a comparison of intensities for a laminar premixed methane/air flame and turbulent premixed methane/air flames from Roby's research

This author concludes that comparison of Roby's OH^*/CH^* data for a laminar flame and a turbulent flame with a Reynolds number (Re) of 3000 to 7000 using his peak height ratio data sets indicates that the OH^*/CH^* ratio is more sensitive to changes in equivalence ratio for the laminar data than the turbulent data. Roby concludes that the low turbulence associated with these Reynolds numbers has little effect on the

equivalence ratio correlation, but goes on to say these conclusions do not indicate that turbulence has no effect on chemiluminescence levels (Roby and others, 1998). Ikeda also draws these conclusions for premixed methane/air flames with a Reynolds number of 8100 (Ikeda and others, 2002). Because levels of turbulence in conventional gas turbine combustors are much higher than the turbulence levels of Roby's or Ikeda's experiments their conclusions might not be valid for higher Reynolds numbers. Additionally Roby's and Ikeda's experiments focused on premixed flames compared with liquid hydrocarbon fuels used in this experiment and Morrell's Experiment. Only additional experiments at higher turbulence can determine this effect.

Morrell's C_2^*/OH^* measurements were taken from an experimental set-up meant to simulate a conventional gas turbine engine fueled by a liquid hydrocarbon. This data is a good benchmark for comparison to the UCC since the n-heptane used in Morrell's experiments has a hydrogen to carbon ratio (H/C) of 2.29 that is a closer approximation to the JP-8+100 used in the UCC than the H/C ratio of 4 for methane. Morrell does not provide turbulence intensity data for his results, but turbulence intensity data for a UCC configuration very similar to the UCC configurations tested in these experiments are presented by Quaale. This data shows the UCC has a turbulence intensity of 20%-60% in the circumferential direction and 40%-180% in the radial direction (Quaale, 2003:80-83). For comparison purposes the cavity mass flow varies from 0.014 to 0.026 kg/s for configuration 1 and from 0.019 to 0.033 kg/s for configuration 2.

Because Morrell's data and Roby's data both show an increase in CH^*/OH^* and C_2^*/OH^* as equivalence ratio is increased the assumption is made that like the CH^*/OH^*

ratio the sensitivity of the C_2^*/OH^* ratio should decrease in sensitivity as turbulence is increased.

Roby's peak height ratio data has been reproduced in figure 32, but with the CH^*/OH^* ratio plotted instead of the OH^*/CH^* ratio (Roby and others, 1998).

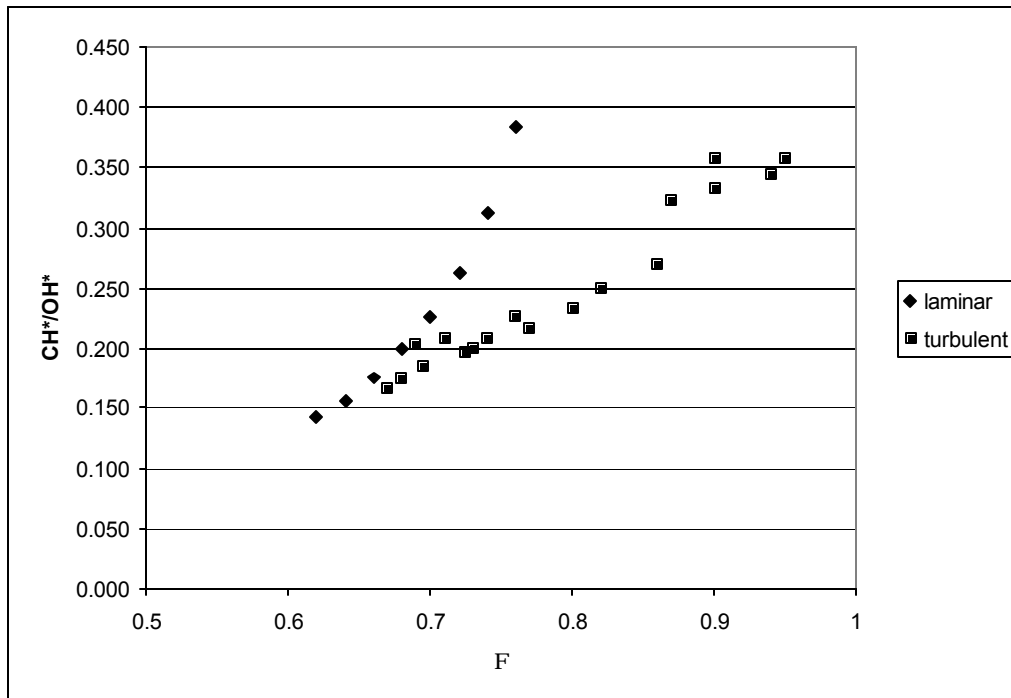


Figure 32: Roby's CH^*/OH^* data for a premixed methane/air flame

IV.4 C_2^* Chemiluminescence Results

In order to determine the approximate location of the flame, C_2^* intensities were used since the C_2^* intensity profile versus displacement from the flame is more narrow than the OH^* or CH^* intensity profiles (Smith and Others, 2002). Table 12 lists the C_2^* intensities for all the view ports at all the test conditions. The maximum C_2^* intensity per test condition are shaded in dark gray while the minimum C_2^* are shaded in light gray. The radial position with respect to the fuel injector centerline in radians is also listed.

Table 12: C₂* Intensity

Test ID	View Port Location							
	A	B	C	D	E	F	G	H
A	0.0497	0.0239	0.0438	0.0340	0.0579	0.0536	0.0393	0.0359
B	0.0774	0.0492	0.1027	0.0777	0.0958	0.0819	0.0712	0.0721
C	0.0948	0.0979	0.0938	0.0857	0.0885	0.0936	0.0772	0.1037
D	0.0190	0.0096	0.0160	0.0144	0.0168	0.0291	0.0203	0.0112
E	0.0229	0.0145	0.0277	0.0268	0.0280	0.0324	0.0247	0.0237
F	0.0325	0.0251	0.0394	0.0281	0.0457	0.0473	0.0432	0.0395
G	0.0348	0.0291	0.0561	0.0400	0.0470	0.0624	0.0344	0.0366
H	0.0413	0.0467	0.0695	0.0564	0.0532	0.0637	0.0441	0.0329
I	0.0636	0.0518	0.0779	0.0704	0.0646	0.0790	0.0748	0.0900
J	0.0192	0.0134	0.0352	0.0328	0.0616	0.0569	0.0236	0.0228
K	0.0257	0.0339	0.0908	0.0568	0.0970	0.0955	0.0594	0.0700
L	0.0488	0.0561	0.1220	0.0803	0.1139	0.1062	0.0769	0.0973
M	0.0089	0.0182	0.0438	0.0409	0.0701	0.0635	0.0262	0.0283
N	0.0280	0.0393	0.0959	0.0537	0.1001	0.0893	0.0422	0.0537
O	0.0476	0.0521	0.1252	0.0924	0.1126	0.0874	0.0609	0.0788
P	0.0236	0.0239	0.0443	0.0442	0.0621	0.0738	0.0645	0.0343
Q	0.0258	0.0353	0.0490	0.0555	0.0879	0.0947	0.0410	0.0353
R	0.0440	0.0483	0.0814	0.0761	0.1179	0.0988	0.0532	0.0529
Position from FI (rad)	0.175	-0.349	0.105	-0.070	0.279	-0.244	0.000	-0.175

A histogram of this information is presented in figure 33. This table shows that the majority of the highest C₂* intensities are from the view ports aimed at the upper half of the cavity. 67% of the maximum C₂* intensities are from view port locations downstream of the fuel injection centerline. Almost all the minimum intensities are from view port locations A and B, which view the inner radius of the cavity and the main flow. These results could indicate that the flames are not being blown out into the main flow and remain within the field of view of the outer radius view ports. See figure 5.

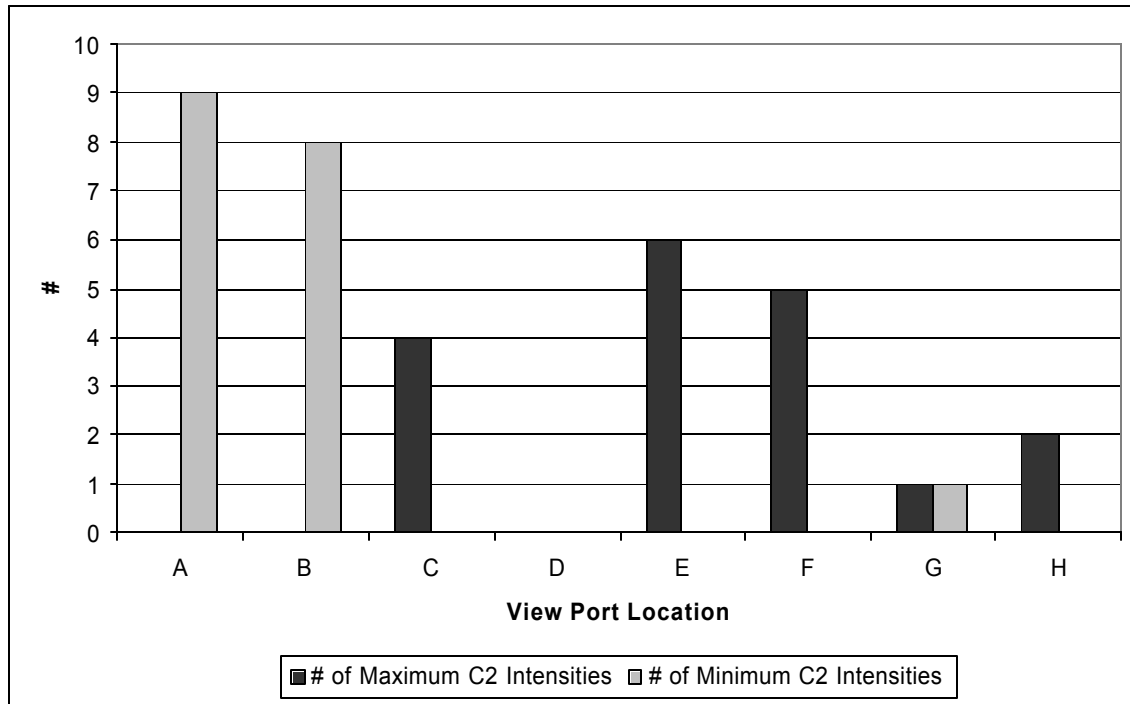


Figure 33: Histogram of C_2^*

Plotting the C_2^* intensities as a function of radial position relative to the fuel injector centerline for configuration 1 for both the inner and outer radius view ports reveals a trend of slightly increasing C_2^* intensity for the inner radius and little variation in C_2^* intensity for the outer radius as you move from upstream to down stream of the fuel injector centerline. Since the signals were gathered from 1.5 to 10 seconds this would suggest the fuel and air are well mixed throughout the cavity with the flame anchored to the fuel injector. Overall the C_2^* intensity data for configuration 1 would suggest the flame is more uniform in the outer radius while less uniform and concentrated more downstream of the fuel injector in the inner radius. The trend of the C_2^* intensity increasing with increasing cavity equivalence ratio per pressure loss is seen in figures 34-35 as well which is to be expected since there is more carbon available. Figures for 3% and 5% pressure losses can be found in the Appendix.

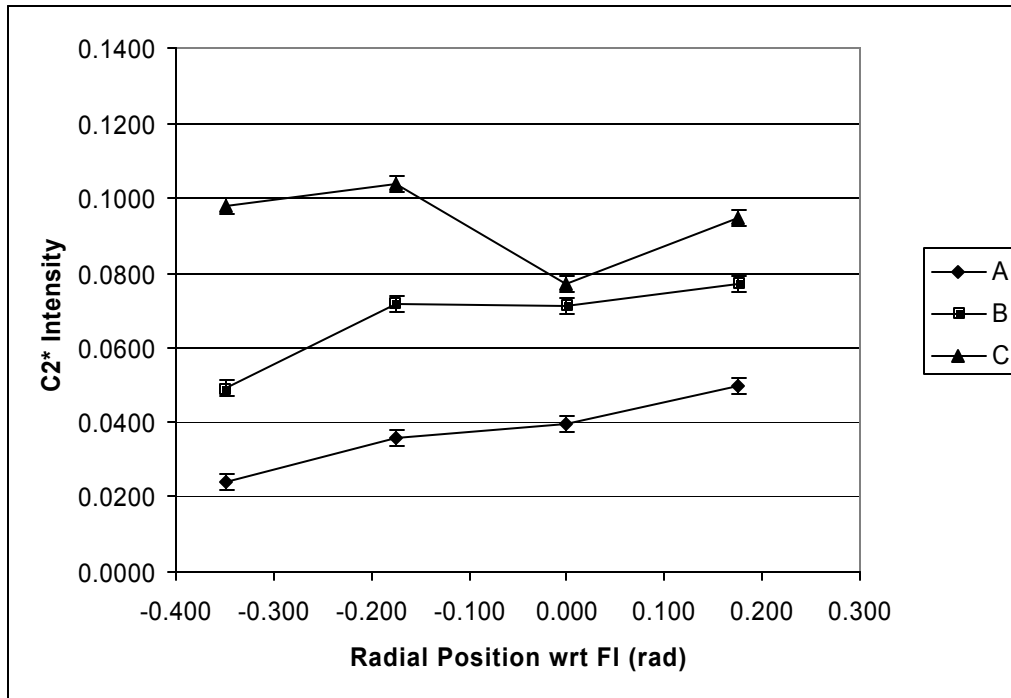


Figure 34: C_2^* Intensity versus Radial Position for the Inner Radius, 2% Pressure Loss, Configuration 1

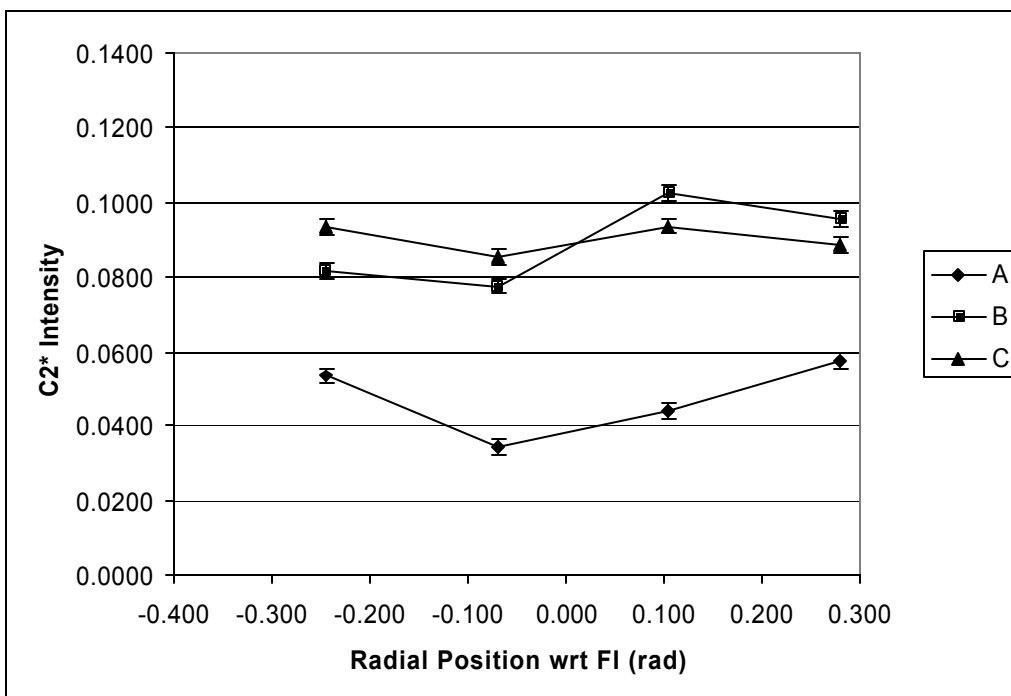


Figure 35: C_2^* Intensity versus Radial Position for the Outer Radius, 2% Pressure Loss, Configuration 1

These same plots for configuration 2 reveal different trends. See figures 44-53 in the Appendix. For the inner radius the C_2^* intensity appears to shift from upstream to downstream of the fuel injector centerline which could indicate the higher g loads associated with the higher pressure drops are forcing the flame further downstream from the fuel injector. For the outer radius the C_2^* intensity appears to be more uniform, but also shows the trend of shifting C_2^* intensity from upstream to downstream as the g-load is increased. The variations in C_2^* intensity suggest the fuel and air relative to configuration 1 are not as well mixed. This could be due to the centerline air jet blowing the flame off the fuel injector therefore causing it to vary. The trend of the C_2^* intensity increasing with increasing cavity equivalence ratio for a specific pressure loss is also seen in these figures. Overall the C_2^* intensity data for configuration 2 would suggest the flame is less uniform in both the inner and outer radius than configuration 1 and shifts downstream of the fuel injector as the g-load is increased.

Figure 36 show the variation of the C_2^* intensity with increasing cavity equivalence ratio. As expected the C_2^* intensity increases since there is more carbon available to form C_2^* .

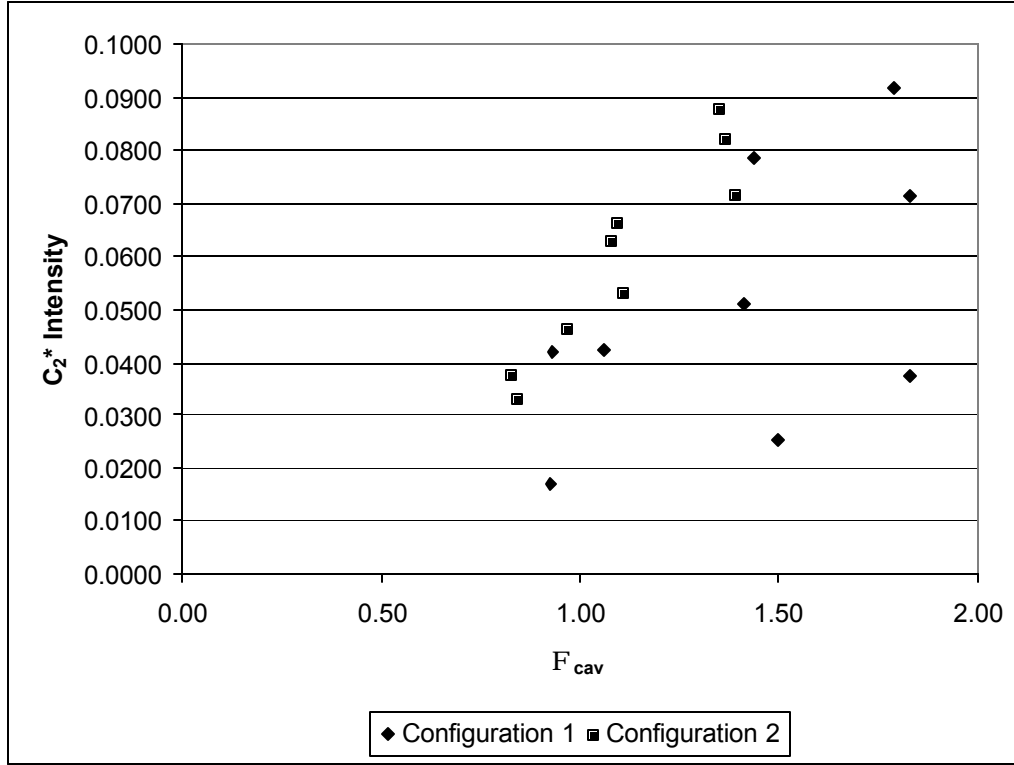


Figure 36: C_2^* Intensity versus Cavity Equivalence Ratio

Figure 37 shows how the G-loading effects the C_2^* intensity. These are calculated G-loads not measured G-loads. The G-load is calculated as follows

$$G = \frac{V_{Tan}^2}{rg} \quad (11)$$

where V_{Tan}^2 the tangential velocity, r is the *cavity radius* and g is the *acceleration due to gravity*. The velocity is determined from mass flow rate, area and density. The angle difference between this calculated velocity and the tangential velocity was determined using CFD (Zelina, 2004). This value is 15° .

As the G-load increases the C_2^* intensity decreases at constant cavity equivalence ratio. For a given G-load increasing the equivalence ratio also increases the C_2^* intensity. The two points that are below 0.04 C_2^* intensity were not used in the

construction of lines of constant Φ since it appears that these points might be outliers when compared to the rest of the data.

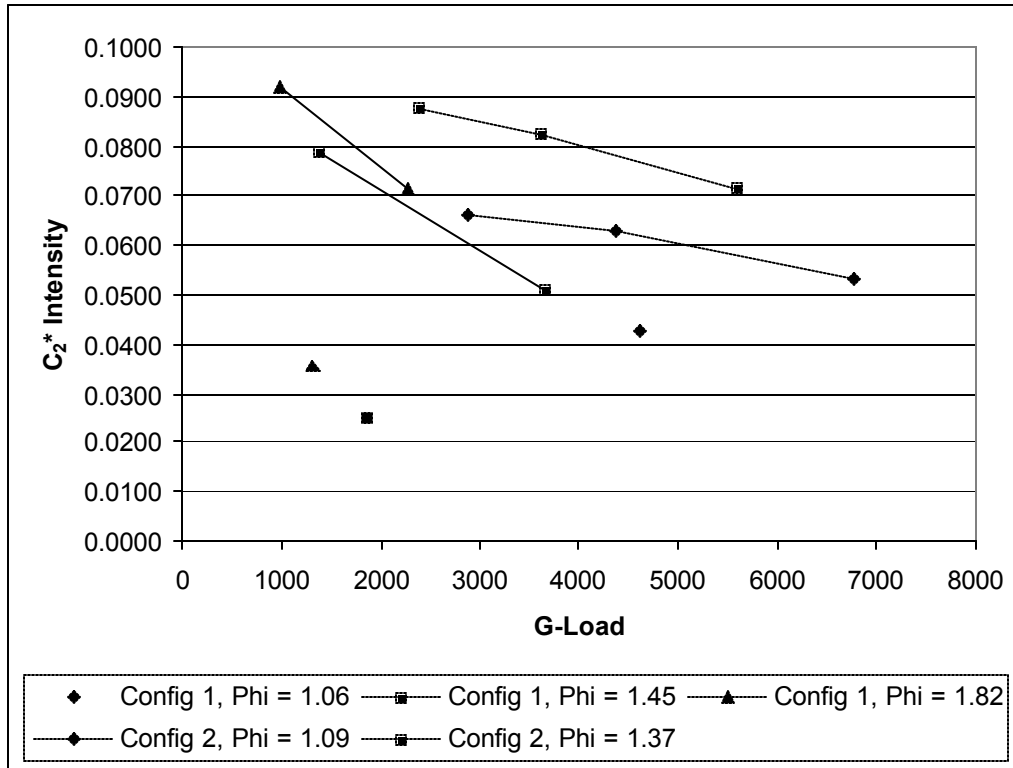


Figure 37: C_2^* Intensity versus G-Load for Constant Φ and $\Phi > 1$

IV.5 Chemiluminescence Sensing Measurement Errors

There are a few sources of error when calculating the CH^*/OH^* and C_2^*/OH^* ratios, and the C_2^* intensities. Because positioning the probe within the UCC relies on the ability of the operator to line up the scribed line with the edge of the fitting (see figure 20) there is some error induced. A repeatability test was utilized in which the operator positioned the probe and then measured the distance from the fitting to the edge of the ceramic tube using a caliper. The measurement was repeated thirteen times and the results appear in table 13.

Table 13: Results of the Repeatability Test

	Measurement (inches)
1	0.270
2	0.273
3	0.268
4	0.271
5	0.272
6	0.271
7	0.272
8	0.272
9	0.275
10	0.268
11	0.268
12	0.266
13	0.261

Using statistics on these measurements two standard deviations from the mean is equivalent to 0.072 inches. Applying this to the intensity data from the chemiluminescence experiments and adding in error bars resulted in very little error in the actual measurements since the intensity varies very little over 0.1 inches (see figure 21). These error bars appear on figures 34-35 and figures 54-61. A two standard deviation spread from the mean was chosen since about 95% of a sample population with a normal distribution lies within two standard deviations of the mean.

Another source of position error that can lead to intensity measurement error is the change in length of the graphite ferrule. Graphite was chosen as the material to lock the ceramic tube in place so as not to damage the brittle ceramic tube. A metal ferrule could cause the ceramic tube to chip or crack. Once the experiments were complete the length of the graphite ferrule was measured and compared to a new ferrule. Figure 38 shows the difference between a used and an unused ferrule.



Figure 38: Comparison of a Used and a New Graphite Ferrule

The used ferrule was 0.007 inches shorter than a new ferrule. Since the ferrule was crushed from tightening and un-tightening the fitting at least 144 times, then this translates into a 0.00005 inch position error per view port intensity measurement. Since this is such a small change it is disregarded. Even the change from the first view port intensity measured to the last view port intensity measured is only of the magnitude of the operator repeatability tests which was a small error of itself.

Errors in conversion of the signal from analog to digital via the 12 bit A/D converter is not considered since 4096 discrete intensities is enough to discern changes in intensity.

IV.6 Fuel Droplet Size Analysis Results

Experiments using the Malvern 2600 Particle Size Analyzer were completed on 15 December 2003. The fuel mass flow rate was matched to those used for the chemiluminescence experiments. Immediately it was recognized that the fuel pressures associated with these low flow rates were not going to be enough to atomize the fuel

spray. For tests numbers 5 and 6 the fuel just dripped out of the nozzle. The fuel pressure associated with test number 5 was approximately 7 psi while the pressure associated with test number 6 was approximately 10-11 psi. For test number 7 the fuel was spraying slightly, but mostly dripping from the nozzle. The fuel pressures associated with test number 7 were approximately 14-15 psi. See table 3 for more detail.

Though particle size measurements were taken since the fuel was just dripping out these measurements were considered inaccurate.

The first experiments run were set so the laser beam was 0.5 inches from the nozzle tip. As discussed earlier the effects of obscuration can skew the data towards smaller particle sizes. Obscuration is a function of the spray concentration. The Malvern 2600 measures concentration and has an indicator to alert the user if the concentration is too high. This was the case for the experiments with a 0.5 inch standoff from the fuel injector. It was decided that only measurements with a 1.5 inch standoff would be taken.

The laser test bed was realigned for this standoff and particle size measurements were recorded. Of these tests only numbers 1-3 and 8 had concentrations that were ideal or slightly greater. Test number 4 had a high concentration as measured by the software's rating scale. This can be explained by the high fuel mass flow rate when compared to the rest of the test conditions. See table 3 for more detail.

Particle size measurements were recorded for all tests even if the fuel was just dripping from the injector. These results are recorded in table 14.

Table 14: Particle Sauter Mean Diameter

Particle Test ID	Exp. ID	SMD (μm)
1	E	346
	N	
	G	
2	F	271
	O	
	P	
3	H	241
	Q	
4	I	180
	R	
5	A	318
6	J	390
	D	
7	B	386
	K	
	M	
8	L	378
	C	

The results would suggest that the particles are extremely large approximately 0.250 – 0.400 mm in diameter. It's possible that the fuel spray has not broken up into smaller particle sizes only 1.5 inches from the tip. Careful examination of one of the spray distributions can help understand what the results mean.



Figure 39: Fuel Droplet Size Distribution for Test Number 2.

As mentioned previously a 100 mm focal length lens was used for the experiments. This lens measures drop sizes from 1.8-188 μm . The SMD's reported for these tests exceeded this size range in all but one test. Additionally the Malvern 2600 used in these tests is only capable of determining particle sizes up to 564 μm . This size also coincides with the location where the size distribution abruptly ends in figure 39. The distribution results are similar for the other tests as well. In essence the SMD's recorded are only rough estimates of the actual fuel droplet sizes.

The results of the data indicate an unformed fuel spray when operating with fuel pressures lower than 20 psi and only a partially formed fuel spray at 20 psi. This poor atomization manifests itself in lower combustion efficiencies. Table 15 shows the fuel

pressure measured and the combustion efficiencies calculated for each chemiluminescence test condition and grouped together by particle size test number.

Table 15: Fuel Pressure and Combustion Efficiency

Particle Test ID	Exp. ID	Fuel Pressure (psi)	Combustion Efficiency
1	E	20.42	98.30
	N	19.53	98.76
	G	21.54	97.89
2	F	28.80	99.41
	O	28.50	99.48
	P	29.47	93.80
3	H	34.76	98.50
	Q	36.39	97.77
4	I	54.54	99.32
	R	52.97	99.31
5	A	7.54	95.35
6	J	9.36	95.74
	D	10.03	97.61
7	B	12.65	98.89
	K	12.93	98.78
	M	13.34	95.11
8	L	16.91	99.36
	C	17.61	99.59

Figure 40 shows a histogram of the combustor efficiencies grouped by particle size test number. Test numbers 5 and 6 have the lowest fuel pressures and some of the lowest combustion efficiencies. Figure 41 shows how combustion efficiency varies with fuel pressure for the experiments.

The trend is toward higher efficiencies with higher fuel pressures. Based on the particle size tests the fuel pressure is indicative of the atomization. In pretty much every test condition run the atomization could be considered poor since the size of the fuel droplets are on the order of 100 μm .

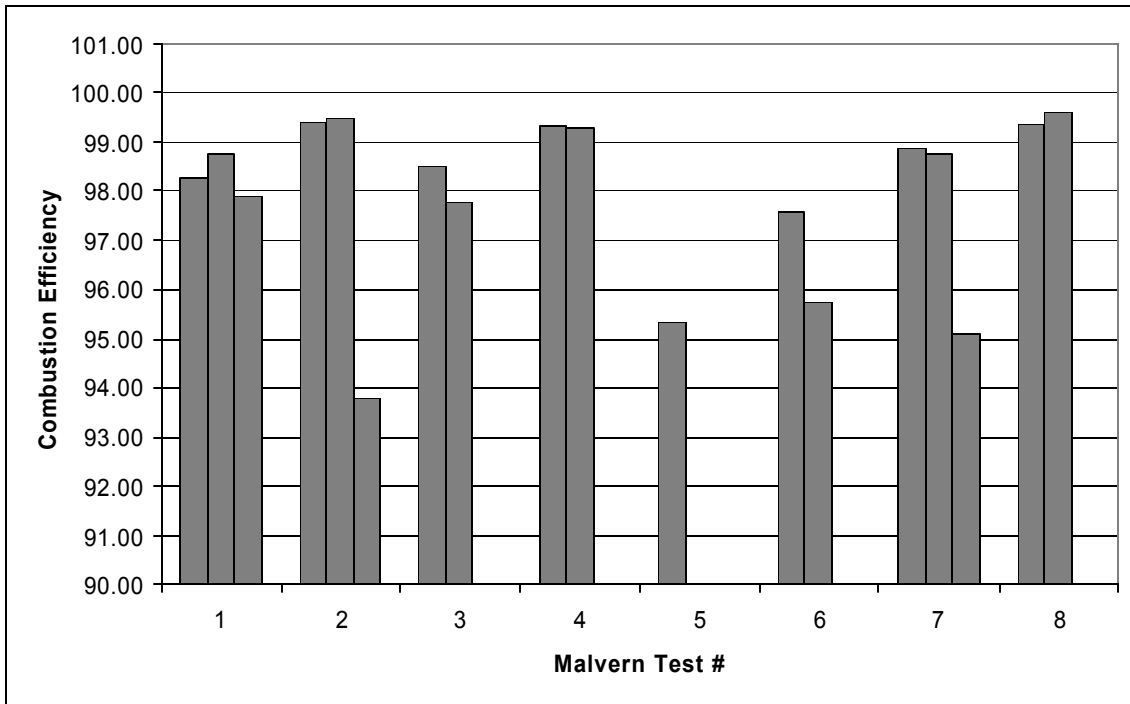


Figure 40: Histogram of Combustion Efficiency Grouped by Particle Size Test Number

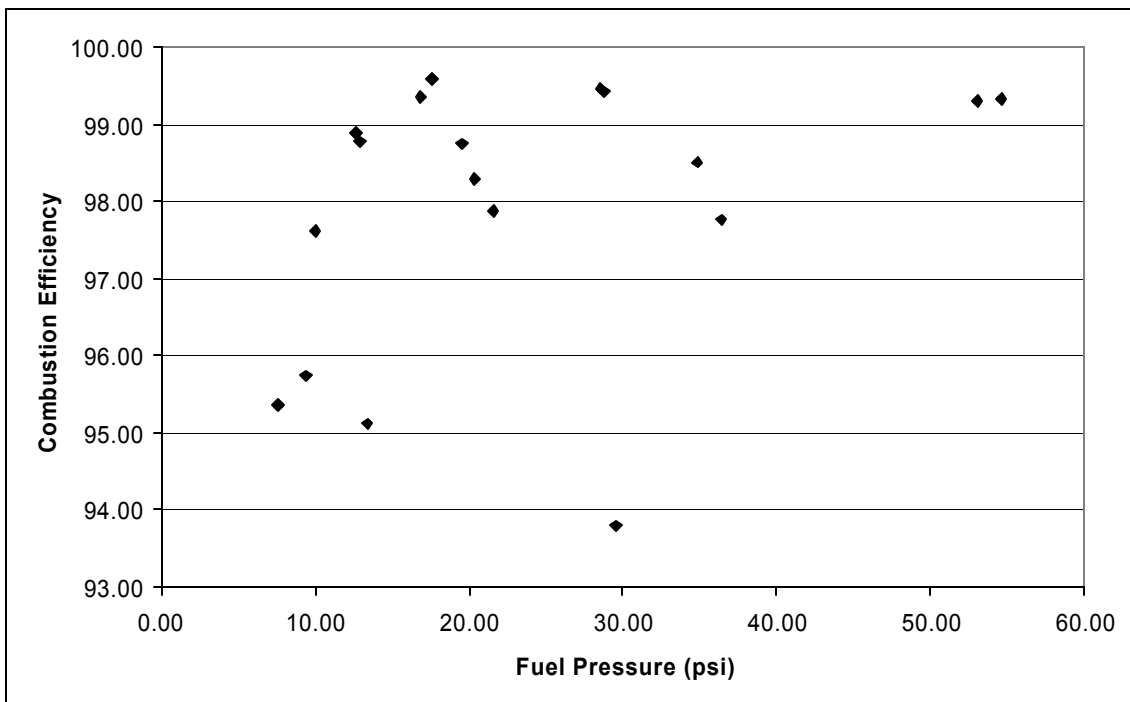


Figure 41: Combustion Efficiency versus Fuel Pressure

Even with poor atomization the combustion efficiency is still high. 61% of the test conditions run had combustion efficiencies greater than 98%. It appears that the turbulent nature of the UCC is aiding the fuel atomization. To explain some of the lower combustion efficiencies it's necessary to look at how combustion efficiency is calculated. Combustion efficiency, η_b , is as follows (ARP1533,1996:16)

$$\eta_b = \left[1.00 - 10109 \frac{EI_{CO}}{H_c} - \frac{EI_{C_xH_y}}{1000} \right] \times 100 \quad (12)$$

where EI_{CO} is the *Carbon Monoxide Emission Index*, $EI_{C_xH_y}$ is the *Unburned Hydrocarbons Emission Index* and H_c is the *net heat of combustion of the fuel* in J/kg.

The only parameters that vary from test condition to test condition are EI_{CO} and $EI_{C_xH_y}$. Figures 42 and 43 show the variation of the emissions index for carbon monoxide (CO) and unburned hydrocarbons (HC) respectively with test conditions.

In addition to having the lowest fuel pressures test conditions A and J also had the third and fourth highest levels of CO and second and third highest levels HC's. These figures also explain why test conditions M and P had such low combustion efficiencies.

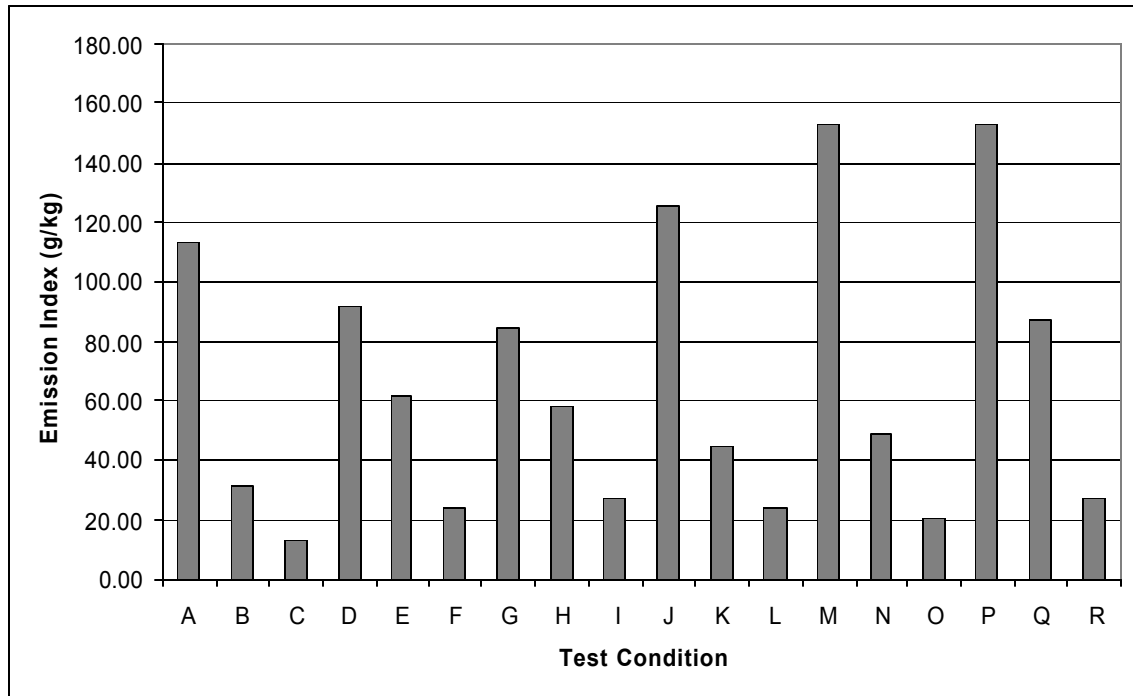


Figure 42: Carbon Monoxide Emission Index for Each Test Condition

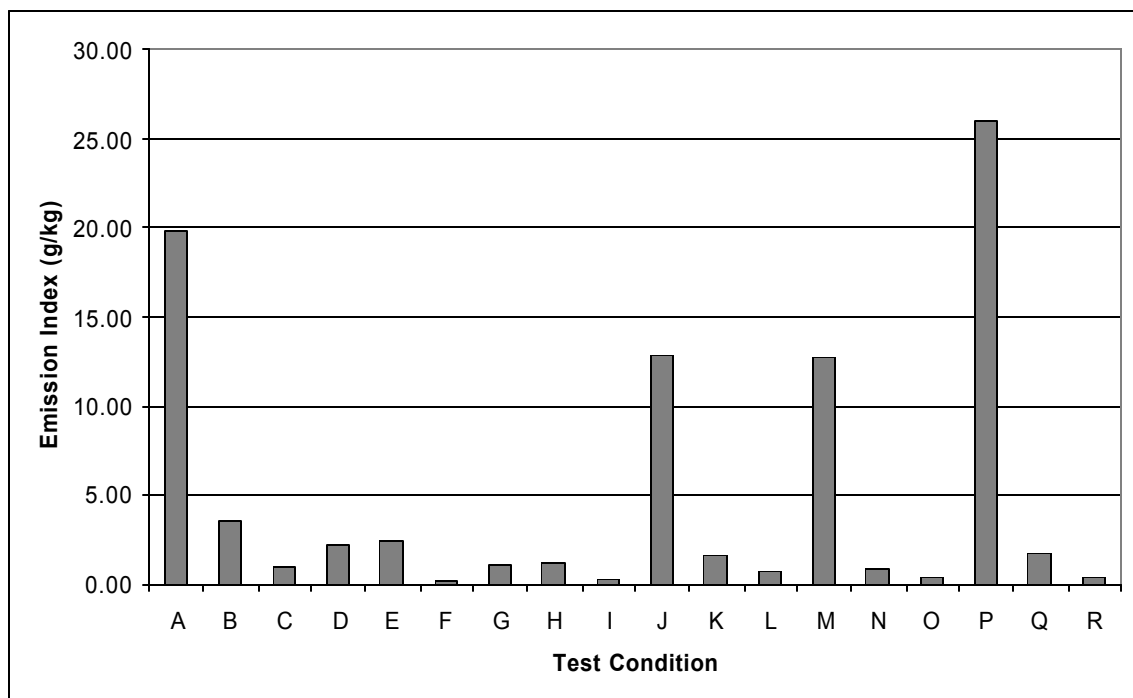


Figure 43: Unburned Hydrocarbons Emission Index for Each Test Condition

V Conclusion

V.1 Chemiluminescence Conclusions

Experiments were set up using the UCC test rig. Three discrete overall fuel to air ratios and three discrete overall pressure drops were used to create nine different test conditions. The UCC configuration was modified to provide a greater quantity of cavity air to the combustor. These nine test conditions were repeated for the new five air hole configuration for a total of eighteen test conditions. Chemiluminescence of three radical species, OH^* , CH^* and C_2^* were measured at eight discrete locations within the cavity. These results were then used to draw conclusions about effects of cavity equivalence ratio and g-loading on these chemiluminescence events.

The results of calculating CH^*/OH^* and C_2^*/OH^* ratios as a function of view port location within the cavity revealed that the majority of the highest of these two ratios are from the view ports in the outer radius of the cavity. This suggests that the majority of the fuel air mixture is combusting in the field of view of the outer radius view ports. This is likely due to the buoyancy forces caused by the colder, hence denser unreacted fuel and air mixture being transported by the high g-loads to the outer radius where it begins to react. The less dense reactants are drawn towards the inner radius and expelled out the cavity. This data is supported by the comparison of C_2^* intensities as a function of view port location within the cavity. The majority of the highest C_2^* intensities occur in the field of view of the outer radius view ports. C_2^* is a good indicator of flame location since its intensity is distributed in a narrow region in the vicinity of the flame.

Additionally the variation of C_2^* intensities with location is greater for configuration 2 than configuration 1 suggesting that the air and fuel are not as well mixed. This could

be due to the air stream from the centerline air hole disrupting the mixture by blowing the flame off the fuel injector. Plots of CH^*/OH^* and C_2^*/OH also lead to the same conclusion since there is more scatter in these ratios as a function of cavity equivalence ratio for configuration 2.

Variation of C_2^* intensity with location for configuration 2 also shows a shifting of this intensity from upstream to downstream of the fuel injector centerline which could indicate the flame is shifting as the g-load is increased. For the outer radius the C_2^* intensity appears to be more uniform, but also shows the trend of shifting intensity from upstream to downstream as g-load is increased.

Variation of C_2^* intensity with cavity equivalence ratio is less scattered for configuration 2 than configuration 1. This trend is opposite the trends seen when CH^*/OH^* and C_2^*/OH are plotted versus cavity equivalence ratio. It is unclear what is causing this other than to say that fuel and air are closely coupled in configuration 1, but not as closely coupled for configuration 2.

Experiments conducted by other researchers has shown that CH^*/OH^* and C_2^*/OH ratios for methane/air and n-heptane/air mixtures increase as equivalence ratio increases. The results of these experiments indicate this same trend for JP-8+100/air mixtures. Additionally it was noted that the C_2^*/OH^* ratio is more sensitive to changes in the equivalence ratio. This sensitivity is also observed in these experiments. The sensitivity for configuration 2 is similar to the n-heptane data collected by Morrell. The sensitivity of configuration 1 is similar, but to a lesser extent. It is unclear why this sensitivity varies with configuration but it is noted that the n-heptane covered an equivalence ratio

range of approximately 0.5 which is similar to the range in configuration 2.

Configuration 1 covers a broader range of equivalence ratios, about 0.8.

Experiments using premixed methane/air flames conducted by Roby has shown that OH^*/CH^* becomes less sensitive to changes in equivalence ratio for a turbulent flame when compared to a laminar flame. This trend is extrapolated to C_2^*/OH^* sensitivity. When the C_2^*/OH^* data for n-heptane from Morrell is compared to the C_2^*/OH^* data for JP-8+100 from these experiments it indicates the C_2^*/OH^* for JP-8+100 is less sensitive to changes in equivalence ratio. This suggests the UCC configuration is more turbulent than the experimental setup used by Morrell. Though no turbulence intensity is provided by Morrell, turbulence intensity data from a UCC configuration very similar to the two used in these experiments indicated 20%-60% in the circumferential direction and 40%-180% in the radial direction

Another trend noted was the decrease in the C_2^* intensity as g-load is increased when cavity equivalence ratio is held constant. The higher g-loads reduce residence time and this could quench C_2^* production.

V.2 Fuel Atomization Conclusions

Based on the tests conducted using the Malvern 2600 Particle Size Analyzer, it was determined that the atomization of the fuel was poor at the conditions analyzed based on observed spray pattern and calculated fuel droplet size. The SMD's calculated were larger than the measurable limit of the lens in all but one test. Additionally part of the size distribution of the fuel droplets was larger than the measurable limit of the Malvern

2600, therefore the SMD's calculated are only a rough estimate of the actual SMD's for each test condition.

This poor spray quality at low fuel pressures manifests itself in the form of lower combustion efficiencies. Many of the test conditions that had low fuel pressures also had low combustion efficiencies. CO emissions and HC emissions contribute greatly to combustion inefficiencies since HC's represent unburned fuel and therefore a loss of heat generation for that unburned mass. The presence of CO indicates a lack of full oxidation to CO₂ or a dissociation of CO₂ to CO and is another source of heat loss. Other test conditions that exhibited low combustion efficiencies, but had greater fuel pressures were the result of having high levels of HC's and CO emissions.

V.3 Recommendations

Intensity data taken for these experiments was time averaged. This time range was from 1.5 to 10 seconds. Since the combustion reactions are of the order of milliseconds a spectrometer or some combination of equipment that can resolve intensities for these extremely short times could be useful to see how the chemiluminescence varies with time.

Research into Methane/air flames indicates little effect of turbulence on the sensitivity of CH*/OH* for changes in equivalence ratio as Reynolds number is increased from 3000 to 8100. This is low compared to the Re of gas turbine combustors. Higher Re and turbulence intensity could effect this correlation. Since correlation of CH*/OH* or C2*/OH* to equivalence ratio is important for combustor diagnostics measuring the changes in CH*/OH* chemiluminescence for discrete equivalence ratios with varying

degrees of turbulence intensity at higher Re can be useful to determine the magnitude of this turbulence effect.

Though AFRL/PRTS has completed some research into fuel injector optimization (Zelina and Others, 2003), it is clear from the fuel droplet size experiments that more is needed to optimize the fuel spray atomization.

Appendix A

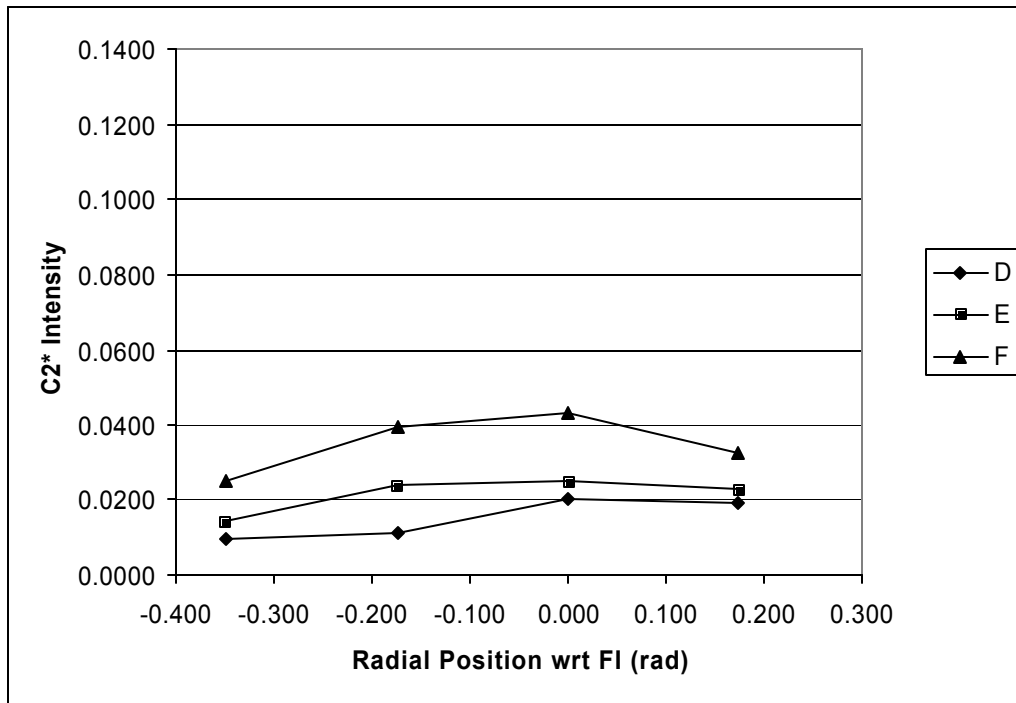


Figure 44: C_2^* Intensity versus Radial Position for the Inner Radius, 3% Pressure Loss, Configuration 1

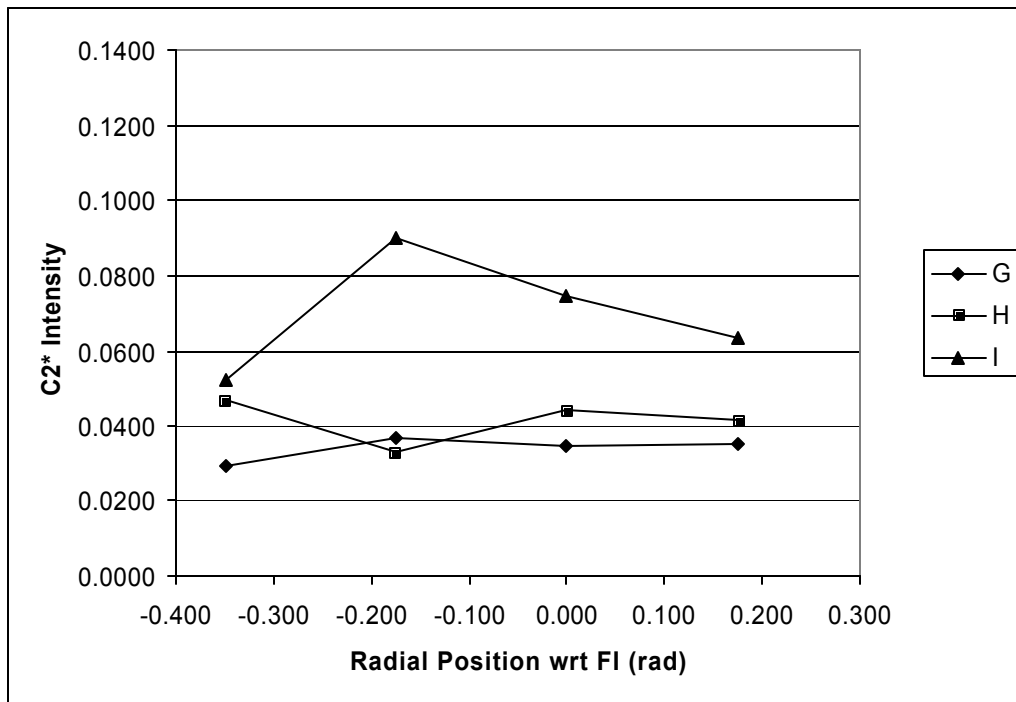


Figure 45: C_2^* Intensity versus Radial Position for the Inner Radius, 5% Pressure Loss, Configuration 1

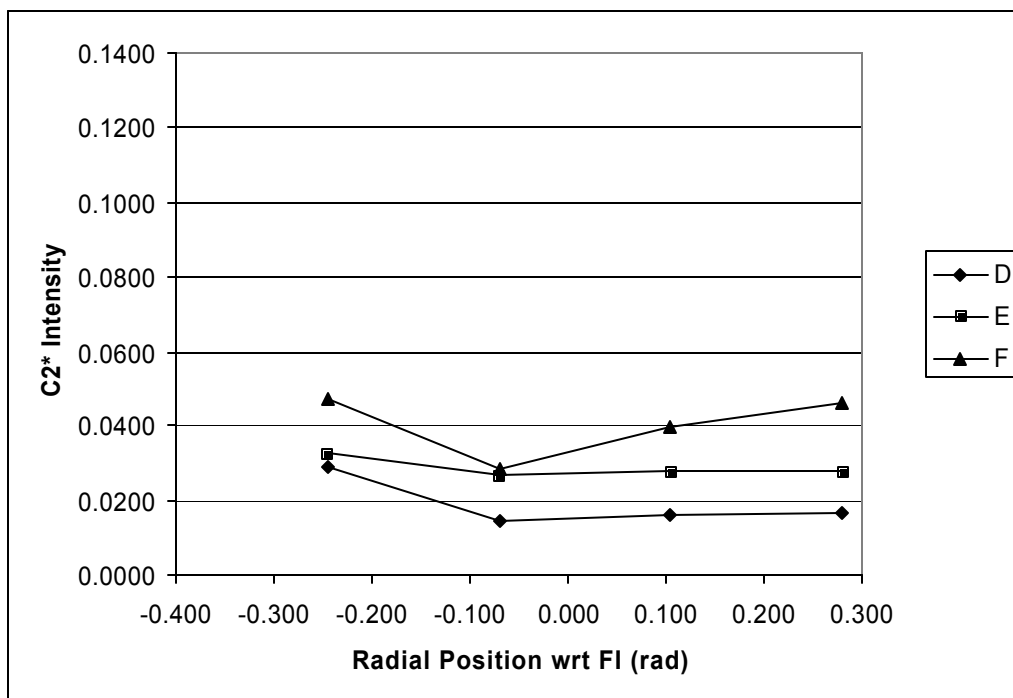


Figure 46: C_2^* Intensity versus Radial Position for the Outer Radius, 3% Pressure Loss, Configuration 1

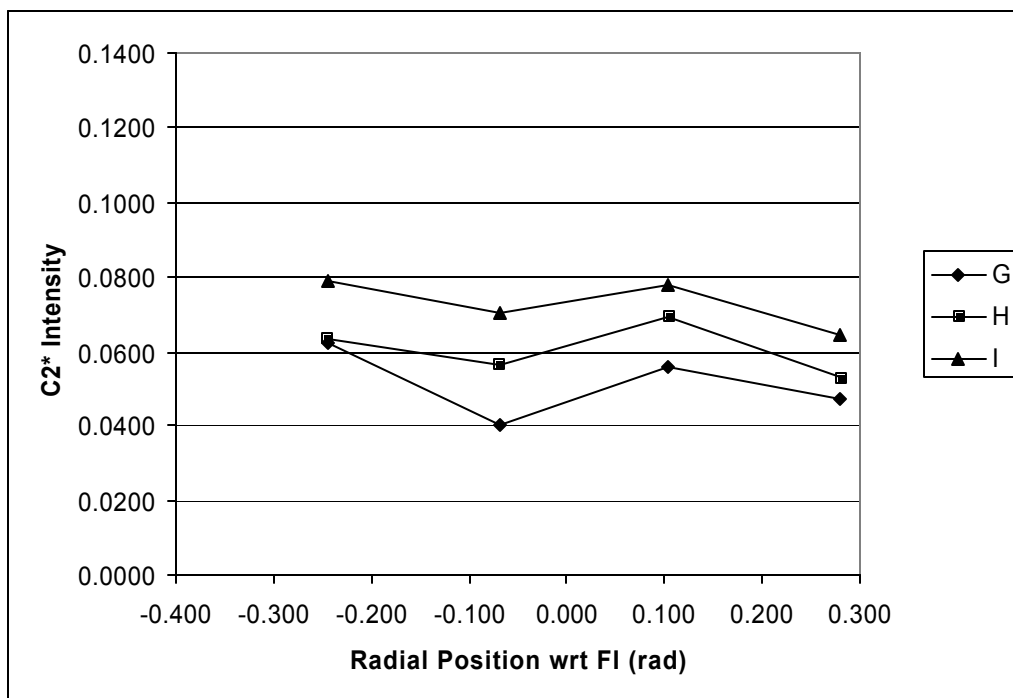


Figure 47: C_2^* Intensity versus Radial Position for the Inner Radius, 5% Pressure Loss, Configuration 1

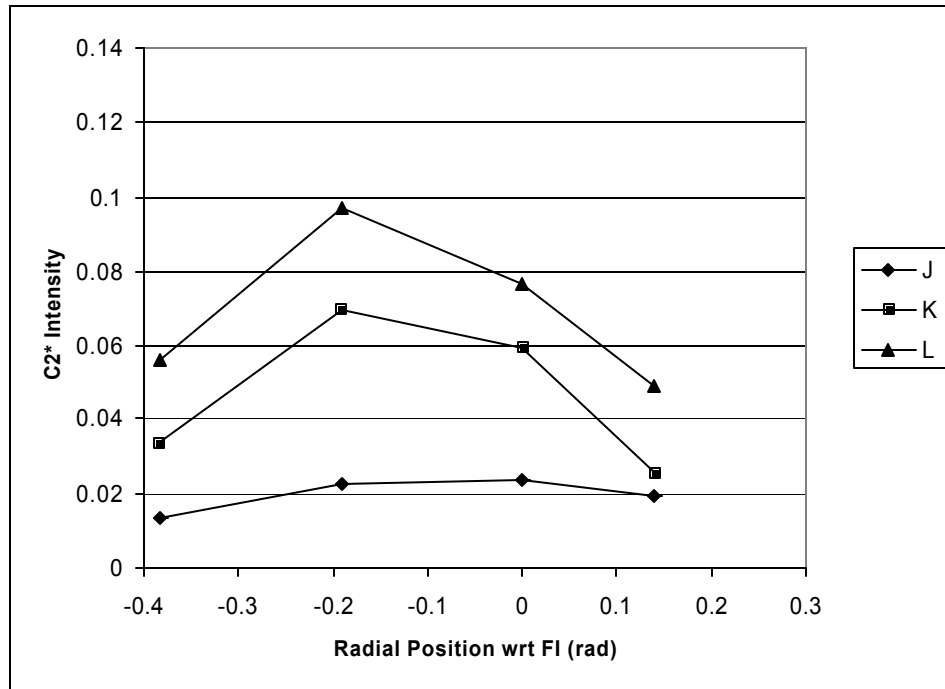


Figure 48: C_2^* Intensity versus Radial Position for the Inner Radius, 2% Pressure Loss, Configuration 2

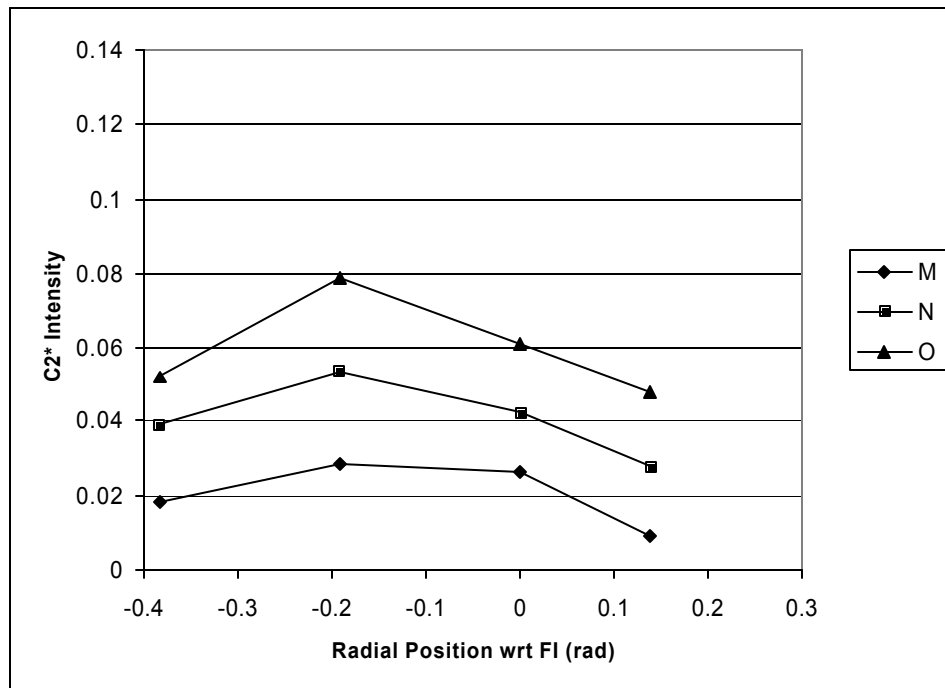


Figure 49: C_2^* Intensity versus Radial Position for the Inner Radius, 3% Pressure Loss, Configuration 2

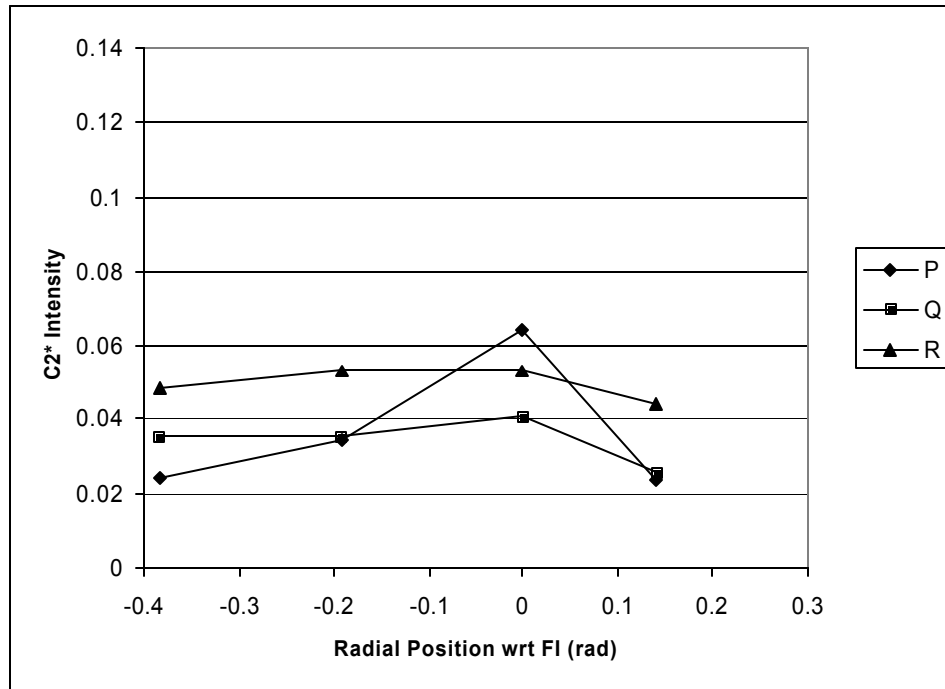


Figure 50: C_2^* Intensity versus Radial Position for the Inner Radius, 5% Pressure Loss, Configuration 2

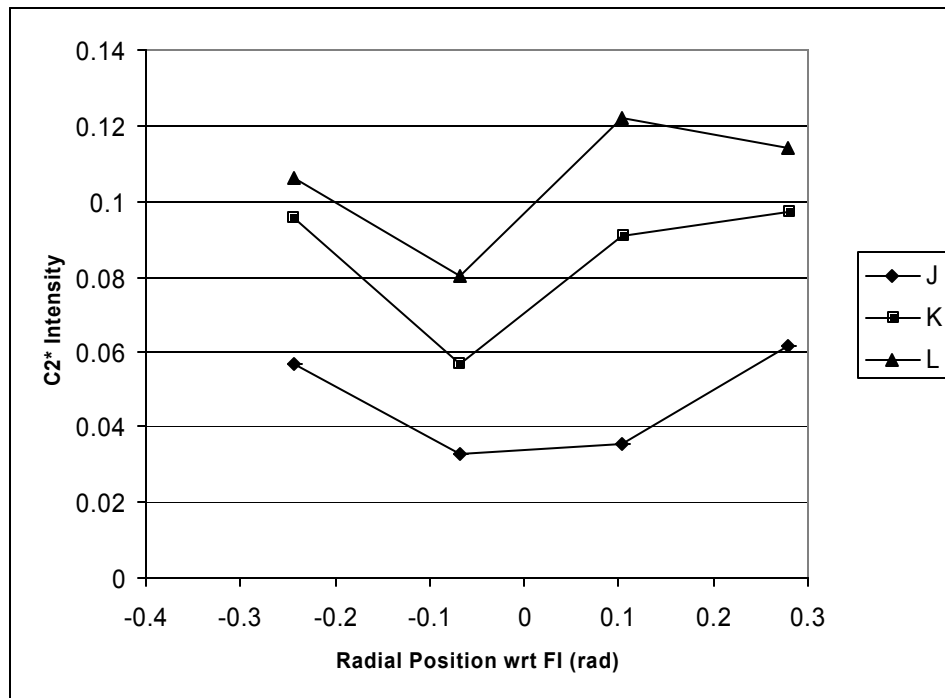


Figure 51: C_2^* Intensity versus Radial Position for the Outer Radius, 2% Pressure Loss, Configuration 2

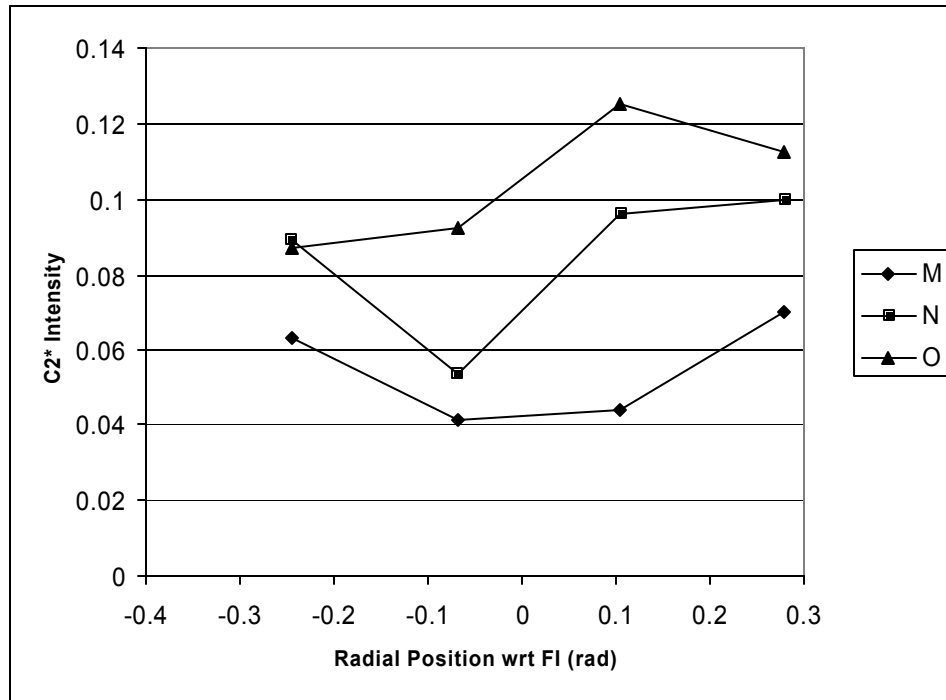


Figure 52: C_2^* Intensity versus Radial Position for the Outer Radius, 3% Pressure Loss, Configuration 2

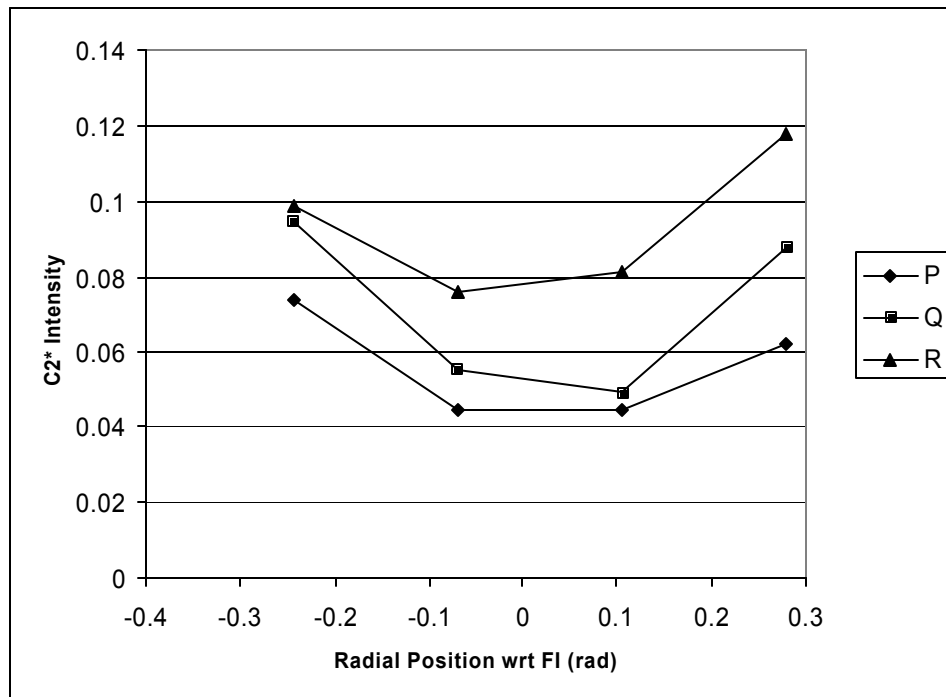


Figure 53: C_2^* Intensity versus Radial Position for the Outer Radius, 5% Pressure Loss, Configuration 2

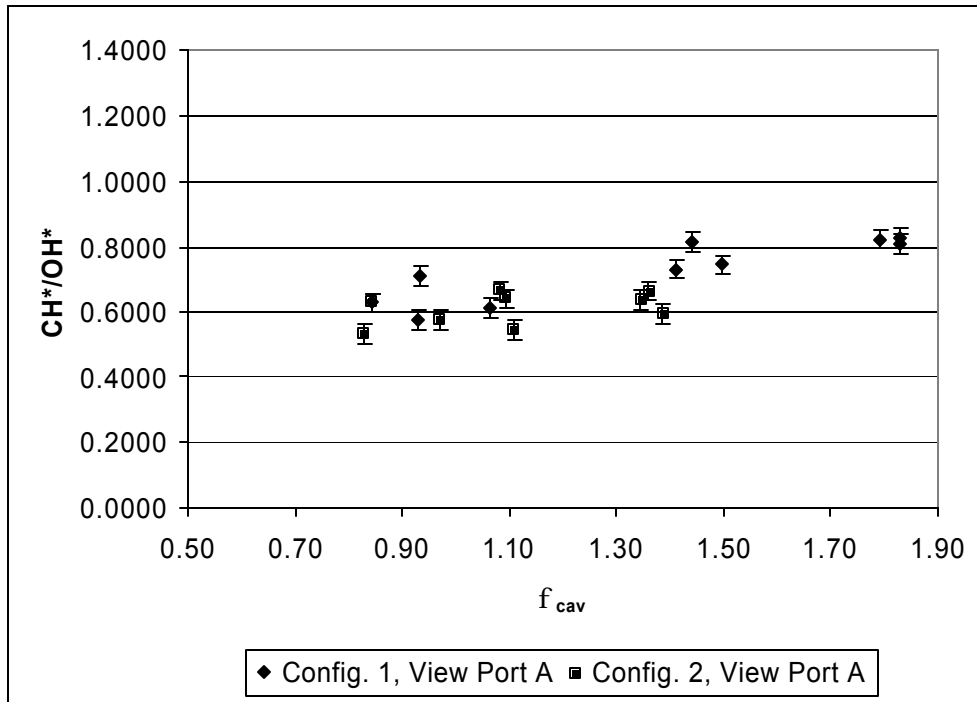


Figure 54: View Port A. CH^*/OH^* Versus Cavity Equivalence Ratio for Both Experimental Configurations

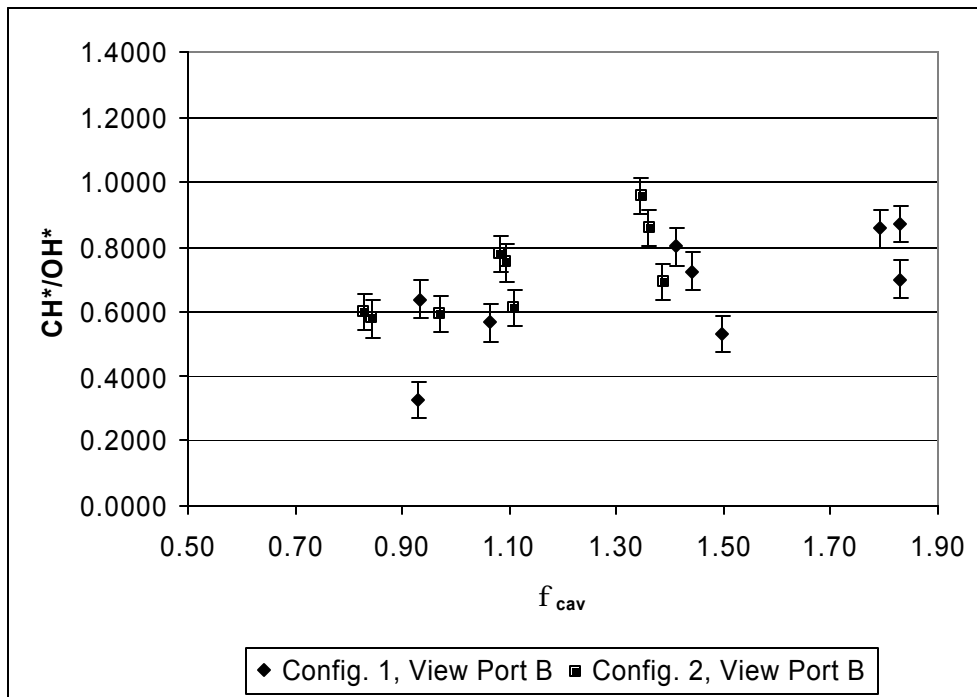


Figure 55: View Port B. CH^*/OH^* Versus Cavity Equivalence Ratio for Both Experimental Configurations

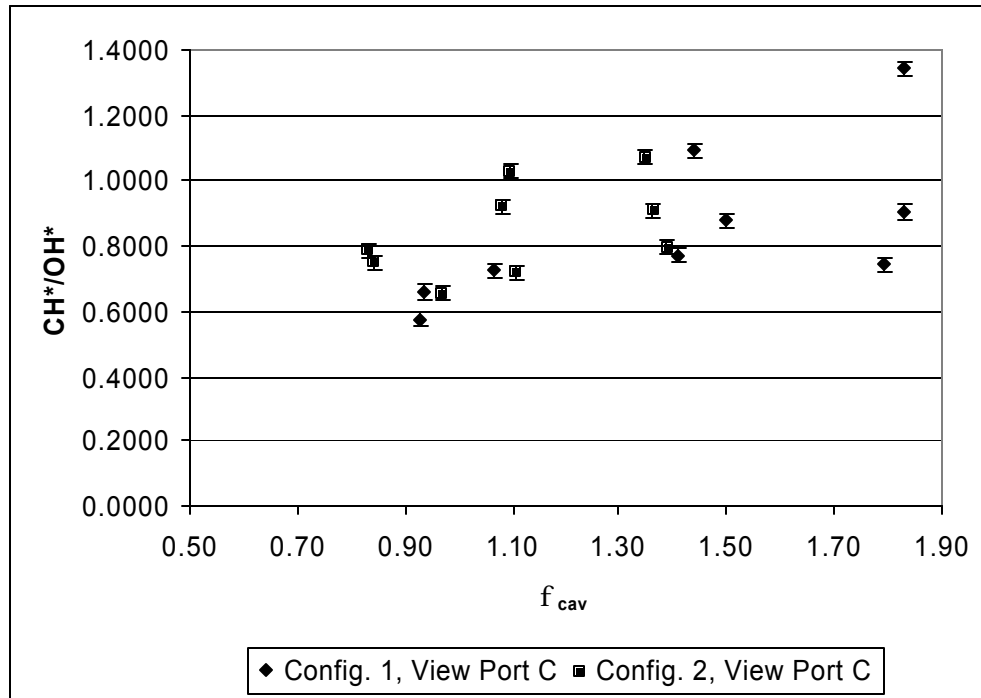


Figure 56: View Port C. CH*/OH* Versus Cavity Equivalence Ratio for Both Experimental Configurations

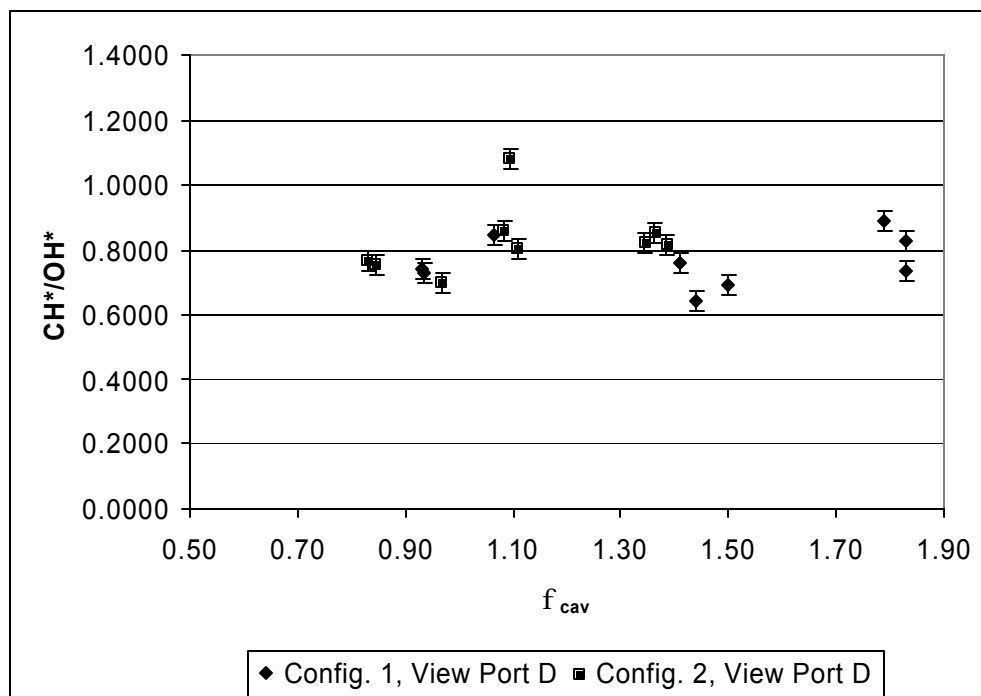


Figure 57: View Port D. CH*/OH* Versus Cavity Equivalence Ratio for Both Experimental Configurations

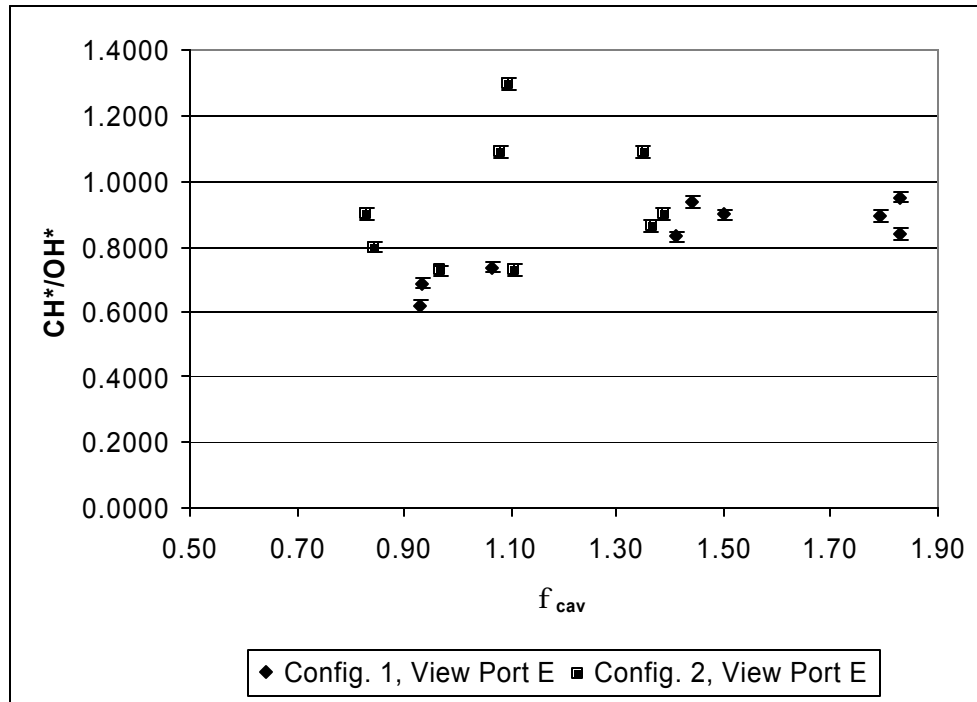


Figure 58: View Port E. CH^*/OH^* Versus Cavity Equivalence Ratio for Both Experimental Configurations

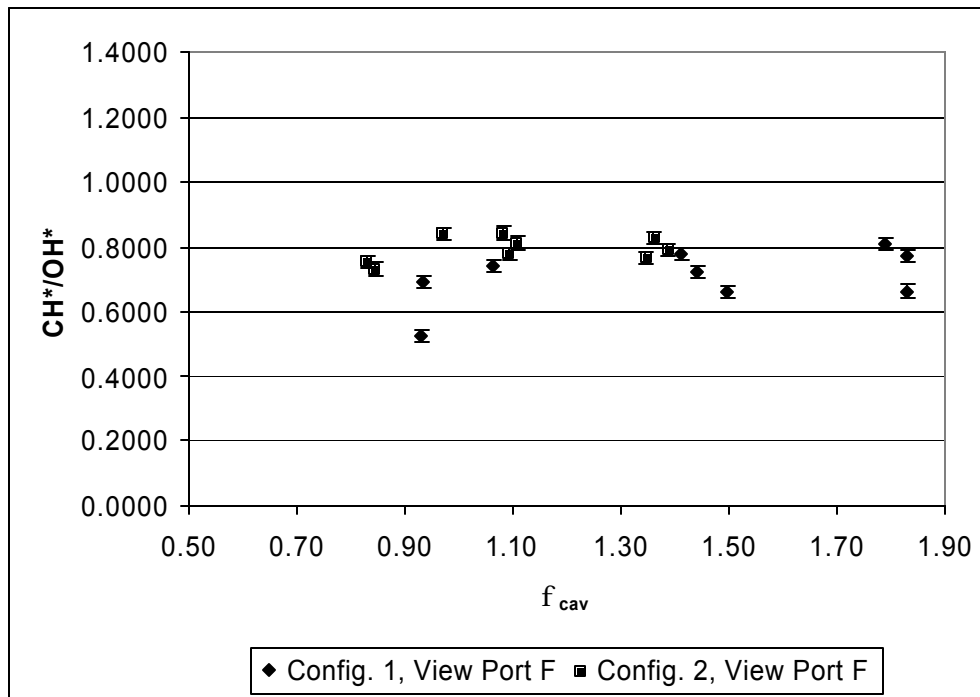


Figure 59: View Port F. CH^*/OH^* Versus Cavity Equivalence Ratio for Both Experimental Configurations

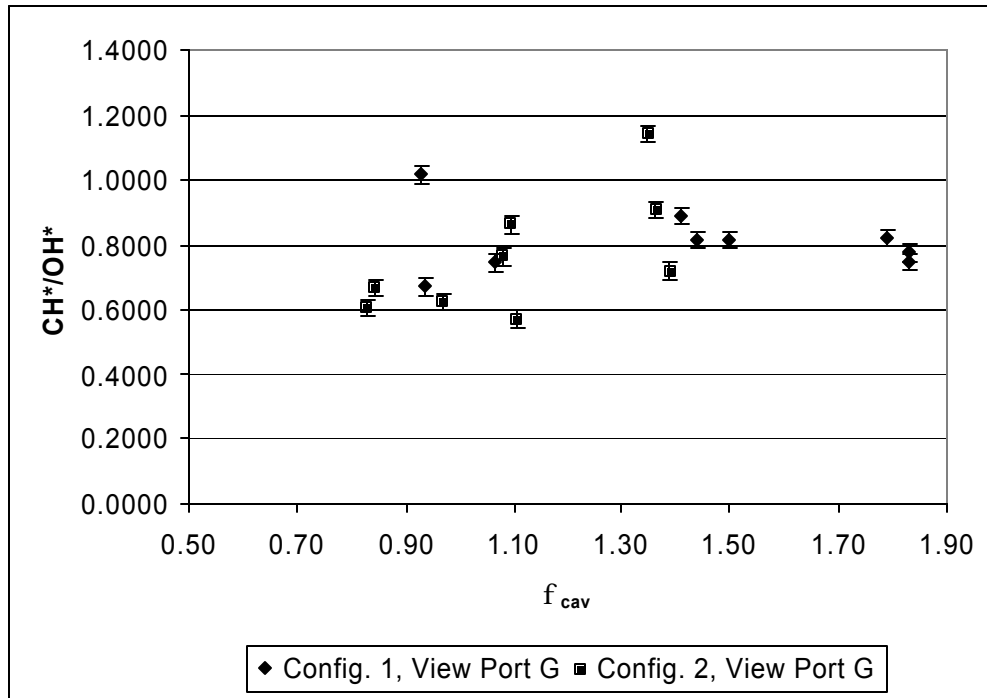


Figure 60: View Port G. CH^*/OH^* Versus Cavity Equivalence Ratio for Both Experimental Configurations

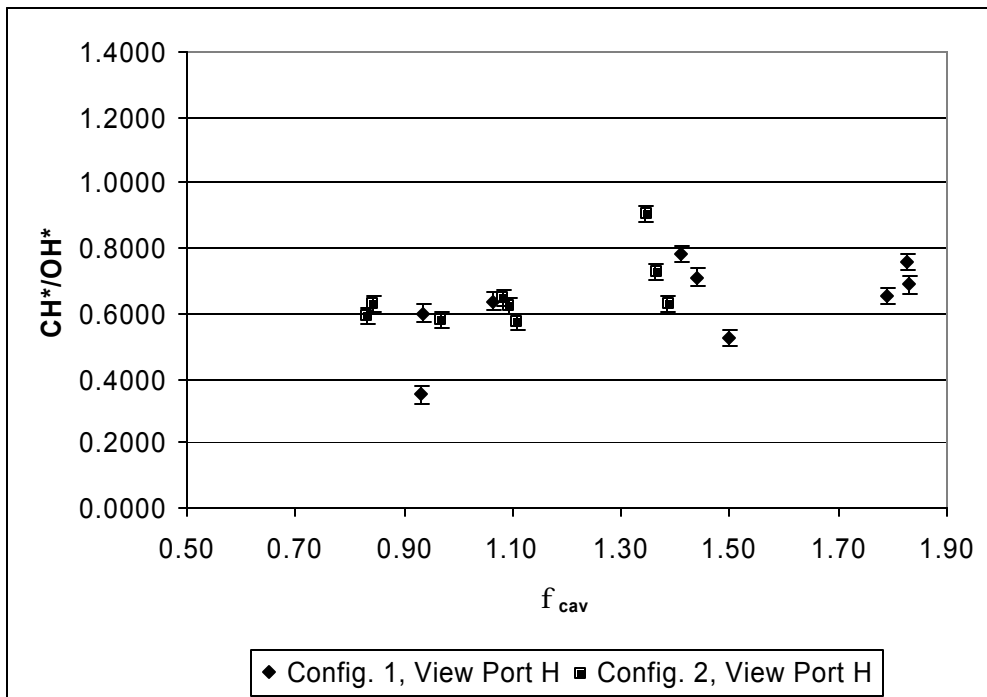


Figure 61: View Port H. CH^*/OH^* Versus Cavity Equivalence Ratio for Both Experimental Configurations

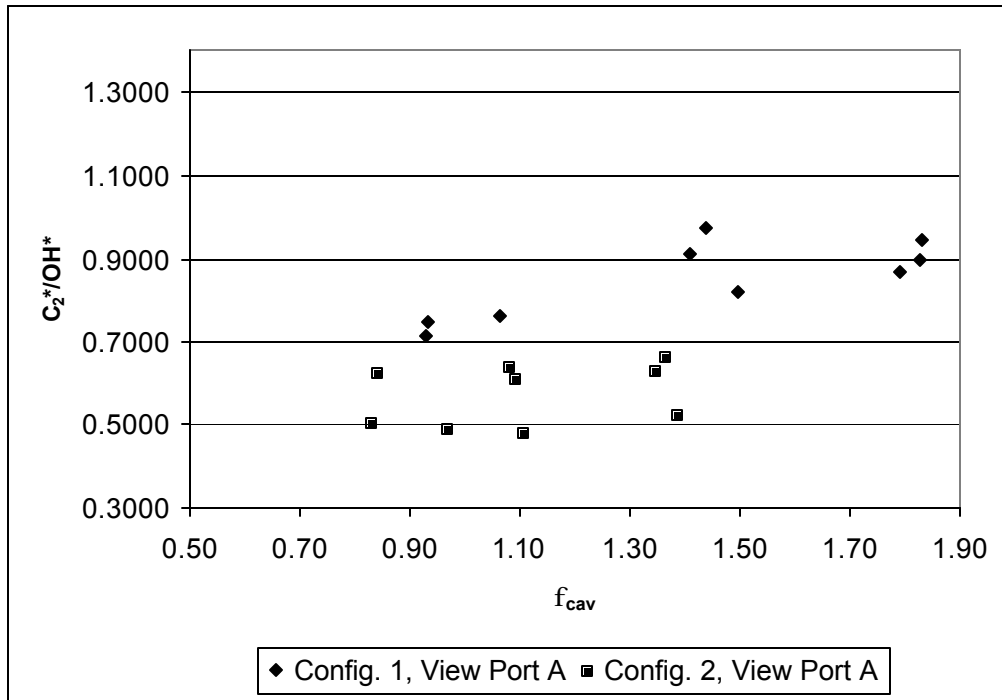


Figure 62: View Port A. C_2^*/OH^* Versus Cavity Equivalence Ratio for Both Experimental Configurations

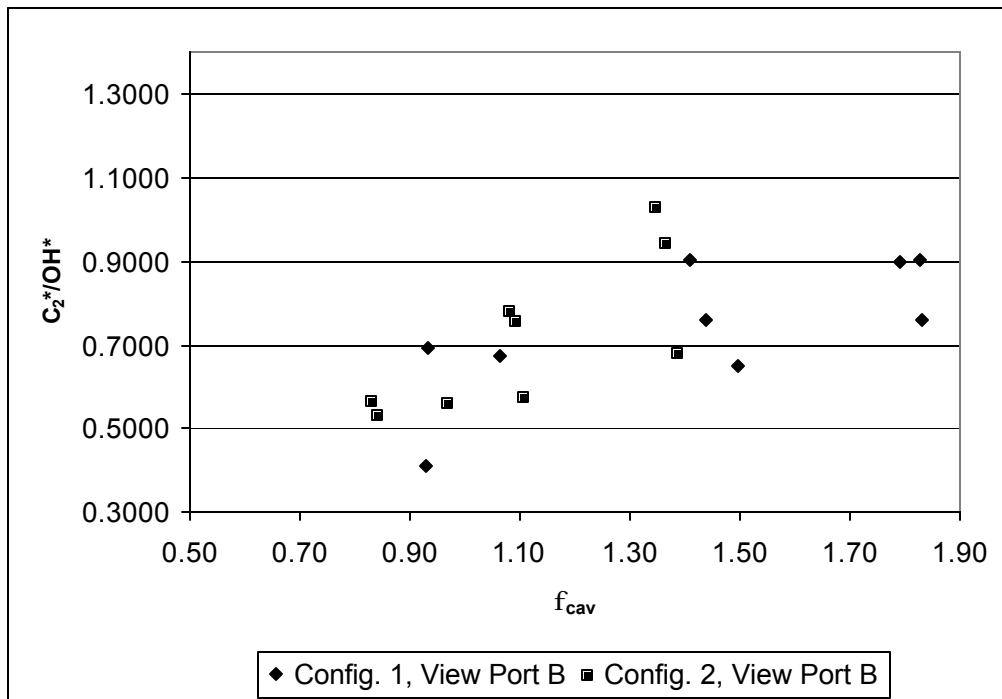


Figure 63: View Port B. C_2^*/OH^* Versus Cavity Equivalence Ratio for Both Experimental Configurations

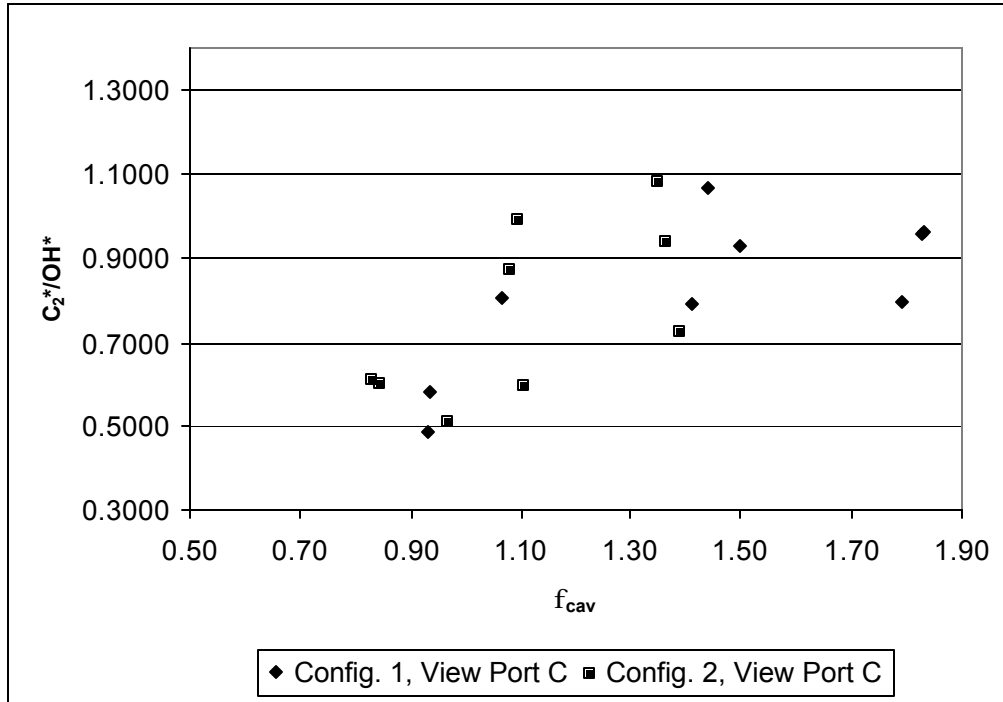


Figure 64: View Port C. C_2^*/OH^* Versus Cavity Equivalence Ratio for Both Experimental Configurations

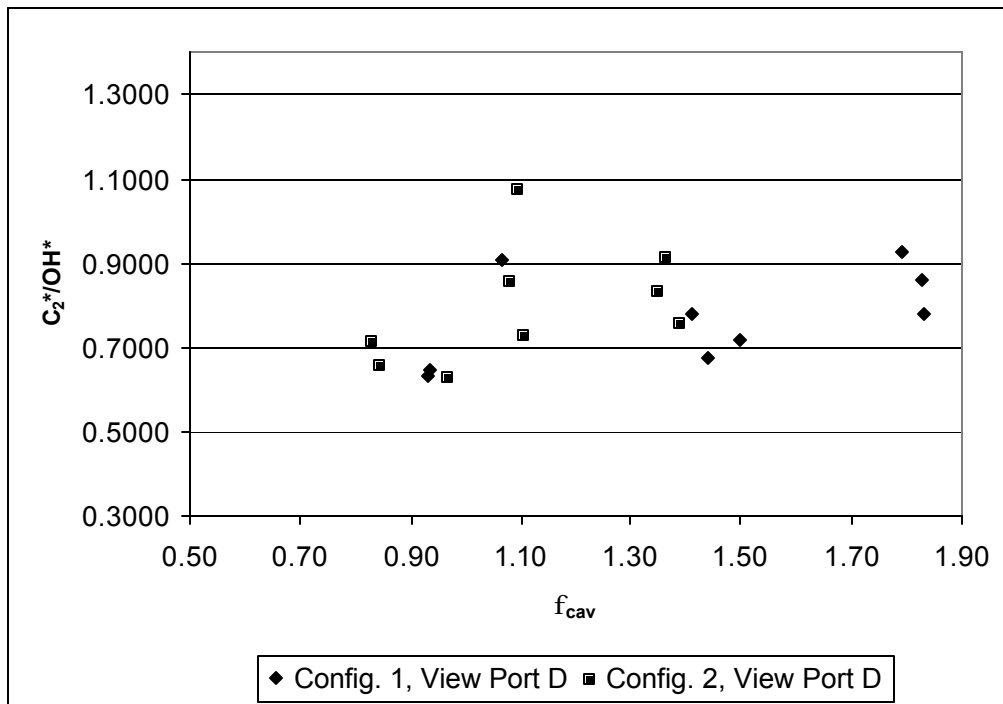


Figure 65: View Port D. C_2^*/OH^* Versus Cavity Equivalence Ratio for Both Experimental Configurations

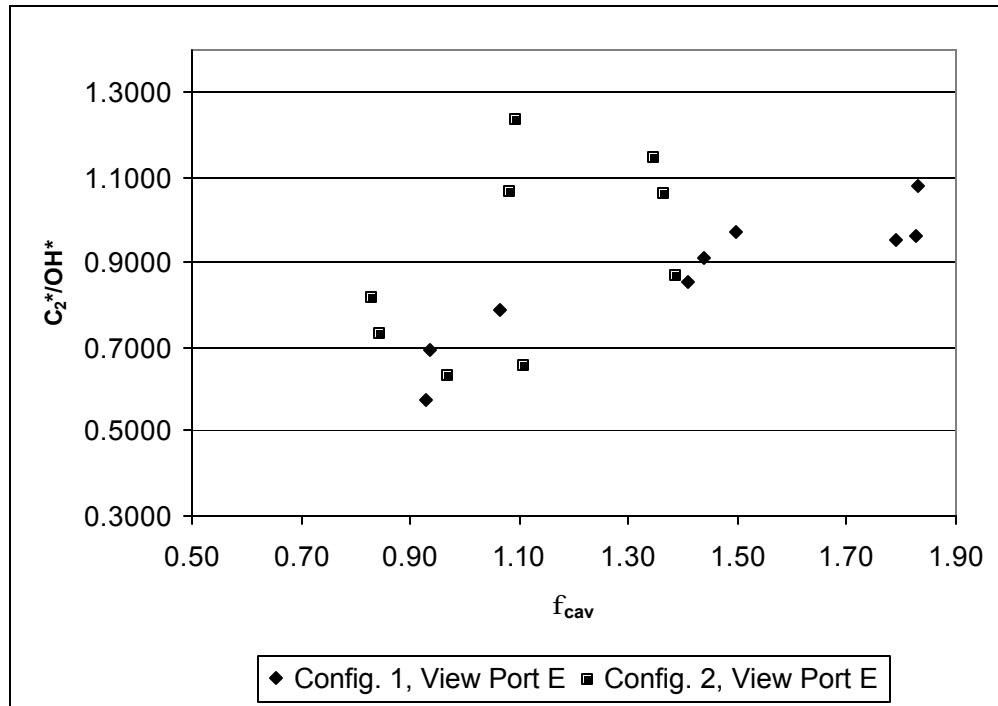


Figure 66: View Port E. C_2^*/OH^* Versus Cavity Equivalence Ratio for Both Experimental Configurations

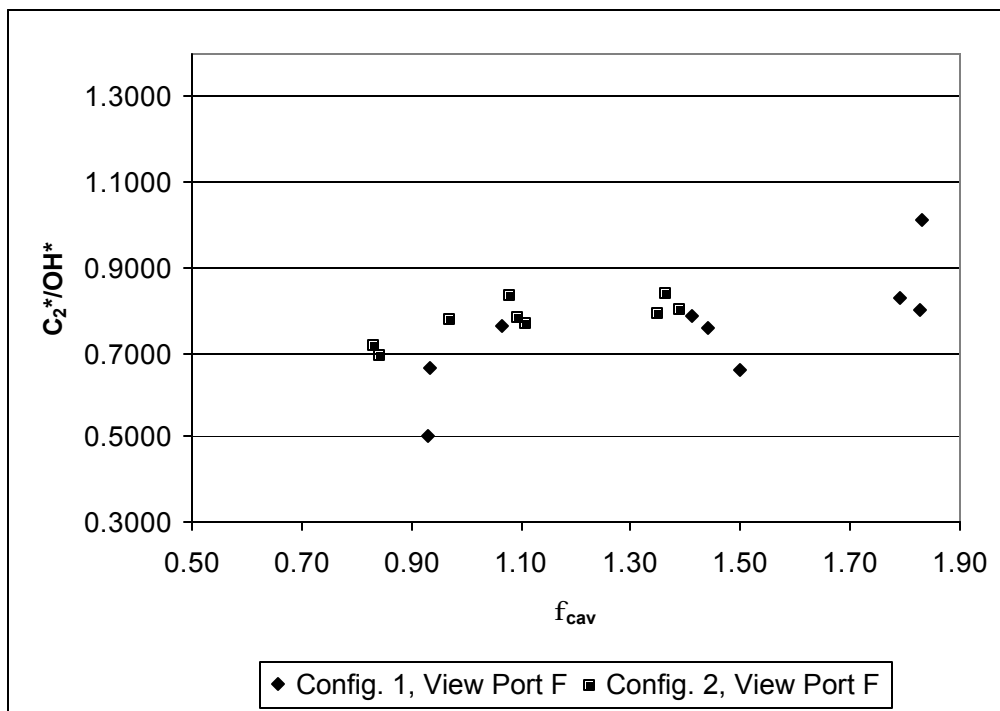


Figure 67: View Port F. C_2^*/OH^* Versus Cavity Equivalence Ratio for Both Experimental Configurations

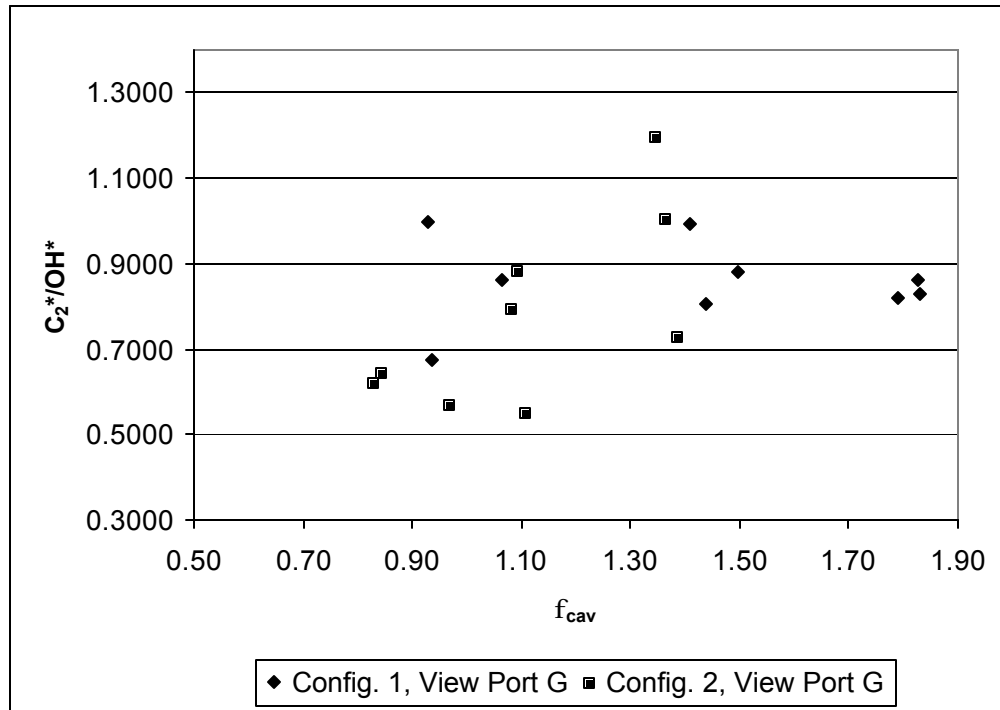


Figure 68: View Port G. C_2^*/OH^* Versus Cavity Equivalence Ratio for Both Experimental Configurations

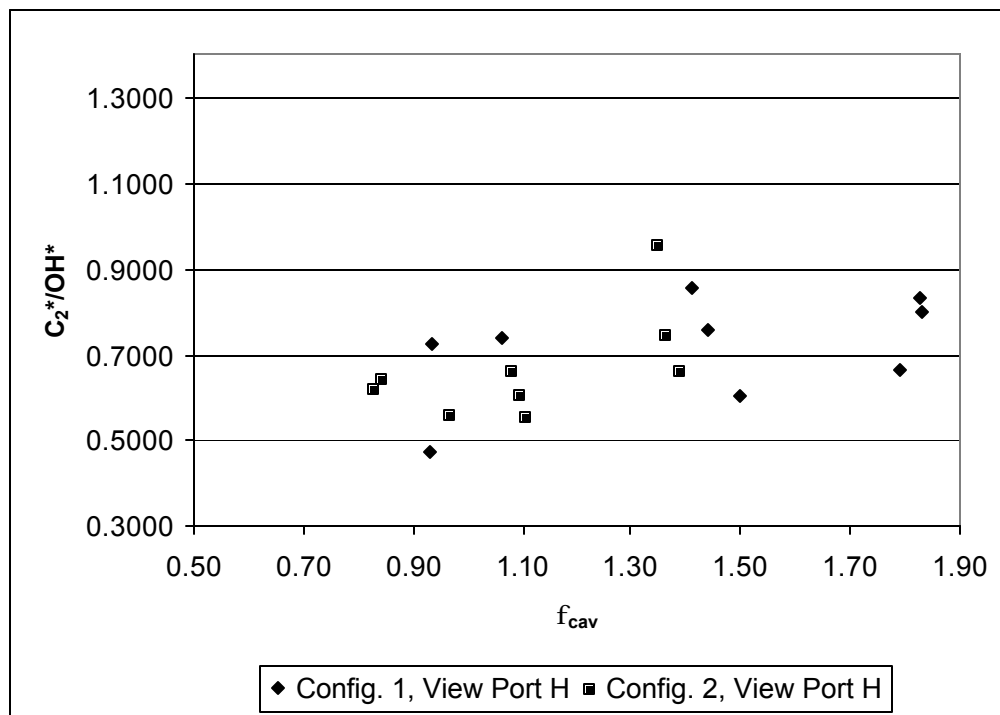


Figure 69: View Port H. C_2^*/OH^* Versus Cavity Equivalence Ratio for Both Experimental Configurations

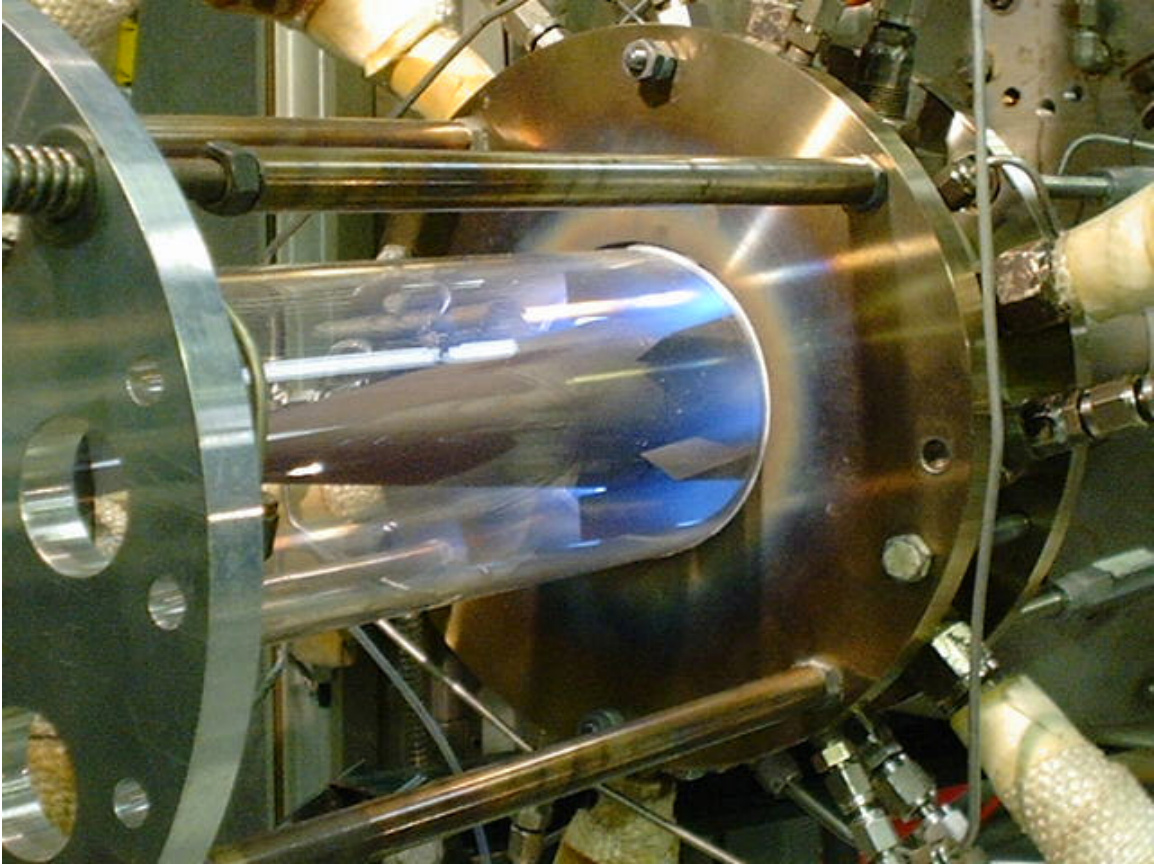


Figure 70: UCC in Operation at a Lean Cavity Equivalence Ratio

Note the blue color of the flame

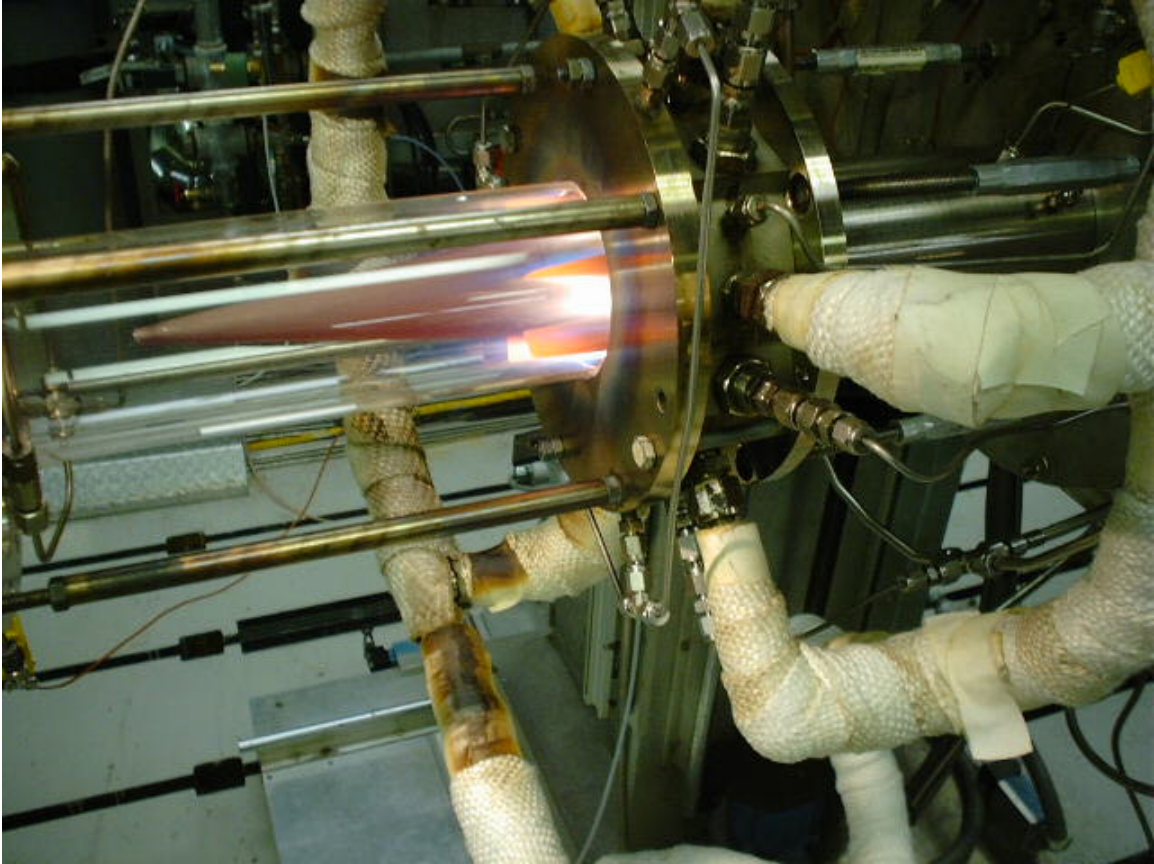


Figure 71. UCC in Operation with a Rich Cavity Equivalence Ratio

Note the orange-yellow color from the soot particles. The vanes are glowing red hot as well. The temperature is increased as the overall equivalence ratio increases

Bibliography

- Anthenien, R.A., R.A. Mantz, W.M. Roquemore, and G.J. Sturgess,, “Experimental Results for a Novel, High Swirl, Ultra Compact Combustor for Gas Turbine Engines,” Presented at the Western States Section Combustion Institute Meeting, Berkeley CA, April, 2001.
- ARP1533, “Procedure for the Calculation of Gaseous Emissions from Aircraft Turbine Engines (Supercedes By Air1533)”, Society of Automotive Engineers, June 1996
- Brown, Michael S. Ph.D. Physicist, Innovative Scientific Solutions Inc., Wright-Patterson AFB OH, Personal Interview. 29 October 2003
- Dodge, Lee G. “Calibration of the Malvern Particle Sizer,” *Applied Optics*, 23: 2415-2419 (1984)
- “Change of Calibration of Diffraction-based Particle Sizers in Dense Sprays,” *Optical Engineering*, 23: 626-630 (September/October 1984)
- Gaydon, A.G. *The Spectroscopy of Flames*. New York: John Wiley & Sons Inc., 1957
- Glassman, Irvin *Combustion*. California: Academic Press. 1996
- Ikeda, Y., J. Kojima and T. Nakajima, “Chemiluminescence Based Local Equivalence Ratio Measurement in Turbulent Premixed Flames,” *40th Aerospace Sciences Meeting & Exhibit*, Reno NV, AIAA-2002-0193 (2002).
- Lefebvre, Arthur H. *Gas Turbine Combustion*. Hemisphere Publishing Corporation, 1983
- Lewis, George, “Centrifugal-Force Effects on Combustion,” *14th Symposium (International) on Combustion*, The Combustion Institute, Pittsburgh PA, 413-419 (1972)
- McQuarrie, Donald A. *Quantum Chemistry*. California: University Science Books, 1983
- Mie Theory Article, http://en.wikipedia.org/wiki/Mie_scattering, 24 October 2003
- Morrell, M.R., J.M. Seitzman, M. Wilensky, E. Lubarsky, J. Lee, and B. Zinn, “Interpretation of Optical Emissions For Sensors In Liquid Fueled Combustors,” *39th Aerospace Sciences Meeting & Exhibit*, Reno NV, AIAA-2001-0787 (2001).
- Quaale, Ryan J. *Experimental Results for a High Swirl, Ultra Compact Combustor for Gas Turbine Engines*. MS Thesis, AFIT/GAE/ENY/03-5. School of Engineering and Management, Air Force Institute of Technology (AU), Wright-Patterson AFB OH, March 2003 (AD-A412863).

- Roby, Richard J., James E. Reaney and Erik L. Johnsson. "Detection of Temperature and Equivalence Ratio in Turbulent Premixed Flames Using Chemiluminescence," *1998 International Joint Power Generation Conference*. Vol. 1, 593-602
- Siegel, Robert and John R. Howell. *Thermal Radiation Heat Transfer*. Washington DC: Hemisphere Publishing Corporation, 1992
- Sirignano, W.A., Liu, F., "Performance Increases for Gas-Turbine Engines Through Combustion Inside the Turbine," *Journal of Propulsion and Power*, Vol. 15 No.1: 111-118 (1999)
- Smith, Gregory P., Jorge Luque, Chung Park, Jay B. Jefferies and David R. Crossley. "Low Pressure Flame Determinations of Rate Constants for OH(A) and CH(A) Chemiluminescence," *Combustion and Flame*, 131:59-69 (2002)
- Verheijen, Peter J.T. "Statistical Distributions in Particle Technology" Article published 15 March 2001, <http://www.dct.tudelft.nl/~verheijen/education/partstat/partstat.pdf>, 24 October 2003
- Zelina, Joseph, G.J. Sturgess, Adel Mansour, and Robert D. Hancock. "Fuel Injector Design and Optimization for an Ultra-Compact Combustor," (2003)
- Zelina, J., J. Ehret, R.D. Hancock, D.T. Shouse and W.M. Roquemore. "Ultra-Compact Combustion Technology Using High Swirl for Enhanced Burning Rate," 38th *Joint Propulsion Conference & Exhibit*, Indianapolis IN, AIAA-2002-3725 (2002).
- Zelina, Joseph, Ph.D. Combustion Engineer, AFRL/PRTS, Wright-Patterson AFB OH, Personal Interview. 11 February 2004

Vita

Capt Armstrong hails from Massachusetts where he attended college at Worcester Polytechnic Institute earning a B.S. degree with honors in Mechanical Engineering in 1996. Following college he worked for Johnson and Johnson as a Quality Engineer supporting manufacturing operations for orthopedic implants and instruments. Upon completion of Air Force Officer Training School in 1999 he worked as an Explosives Engineer for the Air Force Research Laboratory developing counter terrorism technologies. Capt Armstrong's assignment following AFIT will be Project Engineer for weapons integration flight testing for the F/A-22 Raptor.

REPORT DOCUMENTATION PAGE				Form Approved OMB No. 074-0188	
<p>The public reporting burden for this collection of information is estimated to average 1 hour per response, including the time for reviewing instructions, searching existing data sources, gathering and maintaining the data needed, and completing and reviewing the collection of information. Send comments regarding this burden estimate or any other aspect of the collection of information, including suggestions for reducing this burden to Department of Defense, Washington Headquarters Services, Directorate for Information Operations and Reports (0704-0188), 1215 Jefferson Davis Highway, Suite 1204, Arlington, VA 22202-4302. Respondents should be aware that notwithstanding any other provision of law, no person shall be subject to a penalty for failing to comply with a collection of information if it does not display a currently valid OMB control number.</p> <p>PLEASE DO NOT RETURN YOUR FORM TO THE ABOVE ADDRESS.</p>					
1. REPORT DATE (DD-MM-YYYY) 23-03-2004		2. REPORT TYPE Master's Thesis		3. DATES COVERED (From – To) Sep 2002 – Mar 2004	
4. TITLE AND SUBTITLE EFFECT OF EQUIVALENCE RATIO AND G-LOADING ON IN-SITU MEASUREMENTS OF CHEMILUMINESCENCE IN AN ULTRA COMPACT COMBUSTOR				5a. CONTRACT NUMBER	
				5b. GRANT NUMBER	
				5c. PROGRAM ELEMENT NUMBER	
6. AUTHOR(S) Armstrong, Jason M., Captain, USAF				5d. PROJECT NUMBER	
				5e. TASK NUMBER	
				5f. WORK UNIT NUMBER	
7. PERFORMING ORGANIZATION NAMES(S) AND ADDRESS(S) Air Force Institute of Technology Graduate School of Engineering and Management (AFIT/EN) 2950 Hobson Way WPAFB OH 45433-7765				8. PERFORMING ORGANIZATION REPORT NUMBER AFIT/GAE/ENY/04-M01	
9. SPONSORING/MONITORING AGENCY NAME(S) AND ADDRESS(ES) AFOSR/NA Attn: Dr. Julian. Tishkoff 801 North Randolph Street Room 732 Arlington, VA 22203-1977 (703) 696-8478				10. SPONSOR/MONITOR'S ACRONYM(S)	
				11. SPONSOR/MONITOR'S REPORT NUMBER(S)	
12. DISTRIBUTION/AVAILABILITY STATEMENT APPROVED FOR PUBLIC RELEASE; DISTRIBUTION UNLIMITED.					
13. SUPPLEMENTARY NOTES					
14. ABSTRACT Using a spectrometer and high temperature fiber optics the relative intensities of the near-infrared, visible and ultraviolet radiation emitted from the C ₂ *, CH*, and OH* radicals were measured at eight discrete locations within the Ultra Compact Combustor test rig. Blackbody radiation in the near infrared was also observed. The tests were conducted at various g-loadings and overall equivalence ratios and with various air hole configurations. These measurements were compared to determine the effect of these changes on the radiation emitted. Local CH*/OH* ratio was used as a gauge of the local equivalence ratio within the cavity. Results indicate the highest ratios of CH*/OH* occur in the outer radius of the cavity where the high g-loads transport the colder unreacted fuel and air. Fuel droplet size characterization was also conducted using a laser diffraction particle size analyzer. Experiments indicated poor atomization at the lower overall fuel to air ratio test conditions since the fuel flow pressure is relatively low as these test conditions. All experiments were completed in the Air Force Research Laboratory's Atmospheric Combustion Research Facility at Wright-Patterson AFB. This research supports compact common core initiatives of the Versatile, Affordable, Advanced Turbine Engine (VAATE) program.					
15. SUBJECT TERMS Chemiluminescence, Combustion, Laser Diagnostics, Spectroscopy, Hydroxyl Radicals					
16. SECURITY CLASSIFICATION OF:			17. LIMITATION OF ABSTRACT UU	18. NUMBER OF PAGES 117	19a. NAME OF RESPONSIBLE PERSON Ralph A. Anthenien, Civ, USAF
REPORT U	ABSTRACT U	c. THIS PAGE U			19b. TELEPHONE NUMBER (Include area code) (937) 255-3636, ext 4643; e-mail: ralph.anthenien@afit.edu

Standard Form 298 (Rev. 8-98)

Prescribed by ANSI Std. Z39-18